MASTERARBEIT | MASTER'S THESIS

Titel | Title

Generation of intense deep ultra-violet light for high-mass cluster interferometry

verfasst von | submitted by

Hannah Foltas BSc

angestrebter akademischer Grad | in partial fulfilment of the requirements for the degree of

Master of Science (MSc)

Wien | Vienna, 2025

Studienkennzahl lt. Studienblatt | Degree programme code as it appears on the student record sheet:	UA 066 876
Studienrichtung lt. Studienblatt | Degree programme as it appears on the student record sheet:	Masterstudium Physics
Betreut von | Supervisor:	Univ.-Prof. Dr. Markus Arndt

Acknowledgements

I am really grateful for the mental support provided by my family. Thank you, for accepting my life choices and my personal goals. Whenever, I was questioning my decisions or when I was struggling to juggle work and my personal life, you would always be by my side – I honestly appreciate that!

Further, I would like thank our whole research team for the great technical assistance, the professional expertise and the team-spirit! I would like to point out our MUSCLE/LUMI team! I appreciate the great efforts by Severin Sindelar and Bruno Ramírez for providing a reliable cluster source and detection method to conduct the cross-section measurements. Thank you, Stefan Gerlich for the technical expertise and Philipp Geyer for teaching me how to solder. I am grateful for the close collaboration with the UVQuanT project - for the regular meetings, the practical knowledge exchange and the useful tips. Particularly, I would like to point out the help we achieved from Stefan Truppe from the Imperial College of London.

I especially have to thank my supervisor, Prof. Markus Arndt for making me become part of his team and for enabling me to conduct this research. I am thankful for the enormous knowledge transfer and I believe I have achieved the best education from you. I particularly have to thank you for the constructive feedback and for the trust you put into me. Because of your high expectations, I had to learn to spend my time wisely and focus on the most important things. Under your supervision, I have achieved goals greater than I could have imagined. Thank you for shaping my future and for making me a better version of myself!

Of all the people mentioned above, I would especially like to point out the support provided by my lab partner Richard Ferstl. You taught me what real ambition and enthusiasm for science looks like. I have never met anyone with your resilience, patience, and alignment-skills! You introduced me to the world of experimental physics, showed me what good scientific practice entails, and (most importantly) taught me how to properly clean optical mirrors! I will always remember the endless efforts and the countless hours that we spent together in the lab, optimizing the laser setup to squeeze out just one more milliwatt of UV laser power.

Thank you all!

Abstract

Laser light in the deep ultra-violet (UV) region has many high-precision applications because of the small wavelength. It allows to explore research fields like spectroscopy and atomic physics, since many electronic transitions in atoms are in the UV region, for instance the $^1S_0 \rightarrow ^1 P_1$ transition in zinc at 213 nm [1]. UV lasers can excite specific energy levels, enabling laser-cooling and isotope-shift measurements [2], as well as optical pumping, for instance of mercury Hg^0 with a transition at 253.7 nm [3]. With the rising demand of microelectronics, photolithography also becomes more relevant in the manufacturing of microchips using laser wavelengths at 193 nm [4], 132 nm or even in the extreme UV at 13.5 nm [5], [6] - or in the fabrication of photonic integrated circuits [7]. Pulsed UV-light sources can also be employed for time- and angle-resolved photoemission spectroscopy [8].

UV light is often generated via frequency doubling, third-harmonic generation or sum-frequency generation because of the lack of suitable laser transitions in the UV wavelength regime. The most common gain media, like Ti:Sapphire, Nd:YAG, etc., have transitions in the visible or infrared-region, not in the UV. This thesis presents a continuous-wave (CW) laser system, which produces light at a wavelength of 225 nm. It is based on two consecutive external bow-tie enhancement cavities, which frequency quadruple the light of a Ti:Sapphire laser, to achieve deep UV light: 902 nm $\rightarrow$ 451 nm $\rightarrow$ 225 nm. The first resonator contains an anti-reflection coated LBO crystal and generates up to 3 W output power with conversion efficiencies up to 74%. The second cavity uses a Brewster cut BBO crystal and an elliptically shaped beam to generate peak output powers up to 270 mW and stable 160 mW during continuous operation.

To prove the robustness of the cascade laser system, photoionization cross-sections of silver (Ag) clusters in a mass range of $(500 - 2350)$ kDa with a mean velocity of ~ 130 m/s were measured. The laser system shows stable and sufficiently high output power over many hours of operation, over several working days. Although the UV power still needs to be scaled up, it is well suited for further photoionization cross-section measurements on different elements. In the future, the laser system will server as standing-wave ionization gratings for matter-wave experiments with massive metal nanoparticles. Replacing the current 266 nm grating with the here presented 225 nm laser would offer a big extension in materials, since the single photon energy is $E_\gamma = 5.82$ eV and should enable matter-wave interferometry with masses up to 1 MDa.

Kurzfassung

Laserlicht im tiefen ultraviolet (UV) Bereich hat aufgrund seiner kurzen Wellenlänge zahlreiche Hochpräzisions-Anwendungen. Es ermöglicht die Erforschung von Bereichen wie Spektroskopie und Atomphysik, da viele elektronische Übergänge von Atomen im UV-Bereich liegen, wie zum Beispiel der Übergang $^1S_0 \rightarrow^1 P_1$ in Zink bei 213 nm [1]. UV-Laser können gezielt bestimmte Energieniveaus anregen und ermöglichen damit Laserkühlen, Messungen von Isotopenverschiebungen [2], sowie optisches Pumpen, beispielsweise von Quecksilber (Hg^0) mit einem Übergang bei 253.7 nm [3]. Mit der steigenden Nachfrage an mikro-elektronischen Bauteilen, gewinnt auch die Photolithografie an Bedeutung, etwa bei der Herstellung von Mikrochips bei der Laserwellenlängen bei 193 nm [4], 132 nm oder sogar im extremen UV-Bereich bei 13.5 nm [5], [6] verwendet werden. UV-Laserquellen haben auch Anwendung bei der Fertigung von photonisch integrierten Schaltungen [7]. Gepulste UV-Lichtquellen können beispielsweise für zeit- und winkelaufgelöste Photoemissionsspektroskopie eingesetzt werden [8].

UV-Licht wird häufig durch das Prinzip der Frequenzverdopplung, Frequenzverdreifachung oder durch die Summe von unterschiedlichen Frequenzen erzeugt, da es wenig geeignete Laserübergänge im UV-Bereich gibt. Die am häufigsten genutzten Verstärkermedien, wie beispielsweise Ti:Saphir, Nd:YAG usw. haben Übergänge im sichtbaren oder infraroten Bereich, nicht jedoch im UV. Diese Arbeit präsentiert eine Lasersystem, das kontinuierliches Licht bei einer Wellenlänge von 225 nm emittiert. Es besteht aus zwei aufeinanderfolgenden, externen Ringresonatoren, die das Licht von einem Ti:Saphir-Laser zweimal frequenzverdoppeln, um tiefes UV-Licht zu erzeugen: 902 nm $\rightarrow$ 451 nm $\rightarrow$ 225 nm. Der erste Resonator enthält einen anti-reflexbeschichteten LBO-Kristall und generiert bis zu 3 W Ausgangsleistung mit einer Konversionseffizienz von bis zu 74%. Der zweite Resonator nutzt einen Brewster-geschnittenen BBO-Kristall und einen elliptischen Strahl, um maximale Leistungen bis zu 270 mW und stabile 160 mW im Dauerbetrieb zu erzeugen.

Um die Stabilität des Lasersystems nachzuweisen, wurden Photoionisationsquerschnitte von Silberclustern (Ag) im Massenbereich von $(500 - 2350)$ kDa mit mittleren Geschwindigkeiten von ~ 130 m/s gemessen. Das Lasersystem liefert stabile und ausreichend hohe Ausgangsleistung über einige Stunden und mehrere Tage hinweg. Auch wenn die UV Leistung noch verbessert werden muss, eignet sich das hier präsentierte Lasersytem gut für weitere Messungen von Photoionisationsquerschnitten von unterschiedlichen Clustern. Zukünftig soll der Laser als stehendes Lichtgitter bei Materiewellen-Experimenten mit massiven Nanoteilchen aus Metall eingesetzt werden. Das Ersetzen des derzeitigen 266 nm-Gitters mit dem hier vorgestellten 225 nm-Laser erlaubt eine Erweiterung der

verwendbaren Materialien, da die Einzelphotonenenergie $E_\gamma = 5.82$ eV beträgt und soll Interferoemtrie mit Massen bis zu 1 MDa ermöglichen.

Contents

List of Tables

List of Figures

1. Theory of Optical Resonators

Frequency-selection, confinement and storage of light are the most important properties of a resonator. The simplest cavity consists of two mirrors with radii R_1 and R_2, located at the distances z_1 and z_2 on the optical axis, respectively. If the radii of the light's wavefronts corresponds to R_1 and R_2, the beams will be reflected back and forth between the mirrors, without changing the transverse beam profile.

1.1. Gaussian beams as cavity eigenmodes

As a consequence of Maxwells's equations, the propagation of waves can be described by the scalar wave equation given by

$$\nabla^2 u - \frac{1}{c^2}\frac{\partial^2 u}{\partial t^2} = 0 \tag{1.1}$$

where u can be any component of the electric (E_x, E_y, E_z) or the magnetic field (B_x, B_y, B_z). Assuming a monochromatic wave, which can be written as a product of its spatial and temporal components $e^{i\omega t}$ (with $\omega = ck$), equation 1.1 can be re-expressed to get the Helmholtz equation 1.2

$$\nabla^2 u + k^2 u = 0 \tag{1.2}$$

This further reduces to the paraxial Helmholtz equation 1.3, for waves that are traveling close to the optical axis. Assuming a plane wave $u(x, y, z) = A(x, y, z)e^{-i\omega t}$, where the amplitude $A(x, y, z)$ varies slowly along the axis of propagation (z-axis) compared to the x- and y-axes [11], it is given by

$$\nabla_T^2 A - 2ik\frac{\partial A}{\partial z} = 0 \tag{1.3}$$

One possible solution to the paraxial Helmholtz equation 1.3 for a cavity with spherical mirrors are Gaussian Modes, which have the lowest order in angular momentum (TEM_{00}). If the radii of curvature of the beam and the resonator mirrors match, the beam will retrace itself. The wave then fulfills the self-consistency criterion 1.12 and obeys the resonators boundary conditions, which are defined by the mirrors. The Gaussian beam is then called an eigenmode of the cavity.

Every paraxial wave must satisfy 1.3, where $A = A(\vec{r})$ is the complex envelope, k is the wavenumber and $\nabla_T^2 = \partial^2/\partial x^2 + \partial^2/\partial y^2$ is the Laplace operator only for the transverse directions. A more thorough derivation of the Helmholtz equation can be found in many optics textbooks, for instance, in [10], [11] or [22].

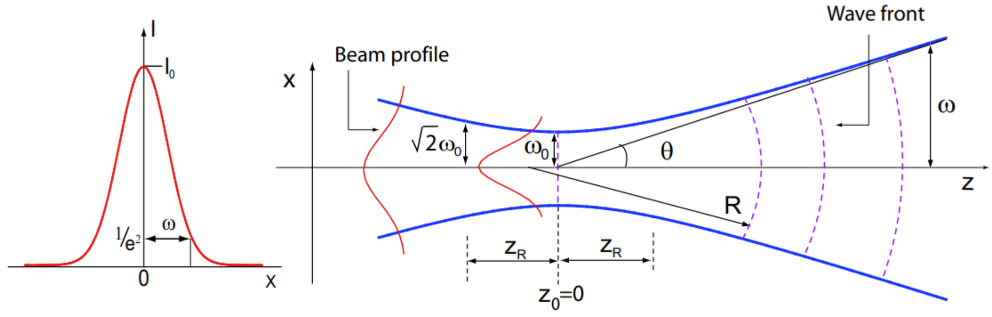

Figure 1.1.: Left: Gaussian intensity distribution. Right: Most important properties of a Gaussian beam, including the minimum waist w_0, to Rayleigh range z_0, the divergence angel θ and the wavefront curvature R. Figure taken from [13]

In general, TEM_{00} Gaussian modes have a circular shape, the normals of the wavefronts are paraxial rays, and the propagation of the beam is chosen along the z-axis. The intensity profile in the xy-axis follows a Gaussian distribution:

$$U(\vec{r}) = A_0 \frac{w_0}{w(z)} \exp\left\{-\frac{\rho^2}{w(z)^2}\right\} \exp\left\{-ikz - ik\frac{\rho^2}{2R(z)} + i\zeta(z)\right\} \tag{1.4}$$

where $U(\vec{r})$ is the complex amplitude, $\zeta(z) = \tan z/z_0$ is the Gouy phase and $\rho^2 = x^2 + y^2$. The other parameters appearing in 1.4 are discussed in more detail in the following lines. The spot size of the beam at a distance z is given by

$$w(z) = w_0\sqrt{1 + \left(\frac{z}{z_0}\right)^2} \tag{1.5}$$

where

$$z_0 = \frac{\pi w_0^2}{\lambda} \tag{1.6}$$

is the Rayleigh range.

The waist has a minimum size $w_0 = \sqrt{\lambda z_0/\pi}$ at $z = 0$ and increases in both directions according to 1.5. The radius of curvature of a Gaussian beam evolves like

$$R(z) = z\left[1 + \left(\frac{z_0}{z}\right)^2\right]. \tag{1.7}$$

A Gaussian beam can also be described by its confocal parameter $b = 2z_0$, which defines the distance around $z = 0$ where the spot size is smaller than $\sqrt{2}w_0$. The angular divergence of the beam far from the center $z \gg z_0$ is defined by$\theta_0 = \lambda/\pi w_0$. A powerful tool to express the evolution of a Gaussian beam is the complex beam parameter q(z):

$$\frac{1}{q(z)} = \frac{1}{R(z)} - i\frac{\lambda}{\pi w(z)^2} \tag{1.8}$$

1.1.1. ABCD-Matrix formalism

To describe the evolution of a paraxial Gaussian beam through an optical system, the so called ABCD-formalism is used [23] [10]. The beam is approximated as a light ray, which is completely characterized by its distance to the optical axis y_i and the enclosed angle θ_i. Every optical element can be described by a 2×2 matrix, such that the relation between the incoming ray $(y_1, \theta_1)^T$ and the outgoing ray $(y_2, \theta_2)^T$ can be calculated using equation 1.9

$$\begin{bmatrix} y_2 \\ \theta_2 \end{bmatrix} = \begin{bmatrix} A & B \\ C & D \end{bmatrix} \begin{bmatrix} y_1 \\ \theta_1 \end{bmatrix} \tag{1.9}$$

The key advantage of using the ABCD-matrix formalism is the fact that a complex system can be described as a sequence of the individual elements. The total ABCD-matrix can then be obtained by a multiplication over all optical elements, which are represented by $M_1, M_2, ..., M_n$, such that:

$$M_{total} = M_n \cdot M_{n-1} \cdot \dots \cdot M_2 \cdot M_1 \tag{1.10}$$

It has to be noted, that the matrices are multiplied in reverse order with regard to the direction from which the beam has entered the optical system. A list of all important ABCD-Matrices for optical elements, which are used in this thesis, is given in the Appendix A.1.

Assume a Gaussian input beam, which is fully characterized bythe beam parameter q_1. After interacting with a paraxial optical system (A, B, C, D), the transmitted beam is calculated by equation 1.11:

$$q_2 = \frac{Aq_1 + B}{Cq_1 + D} \tag{1.11}$$

1.1.2. Self-Consistency and Resonator Stability

For a stable eigenmode, which reproduces itself after a full round trip, the self consistency-criterion is given by equation 1.12

$$q_1 = q_2 = q \tag{1.12}$$

such that equation 1.11 reduces to

$$q = \frac{Aq + B}{Cq + D}. \tag{1.13}$$

Using that the individual optical elements are unimodular $A_iB_i - C_iD_i = 1$, equation 1.13 can be re-expressed as

$$\frac{1}{q} = \frac{D - A}{2B} \pm i \frac{\sqrt{1 - \left(\frac{A+D}{2}\right)^2}}{B}. \tag{1.14}$$

Comparing equation 1.14 with the expression for the inverse q-parameter 1.8 and using the requirement, that w^2 has to be real-valued and non-negative, the following stability criterion for a resonator can be derived:

$$\left|\frac{A+D}{2}\right| \leq 1. \tag{1.15}$$

1.2. Polarization

The time evolution of the direction of the electric field vector $\vec{E}(\vec{r},t)$ of light determines the polarization. In the case of monochromatic light, the space components of $\vec{r}$ change sinusoidally with time. In general they can have different amplitudes and phases, such that the electric field vector $\vec{E}(\vec{r},t)$ follows the shape of an ellipse.

In the paraxial approximation, light travels close to the optical z-axis. In this regime, the waves can be described as transverse electric (TEM) since the vector $\vec{E}(\vec{r},t)$ lies in the transverse xy-plane. In the most general case, a wave is elliptically polarized. The state of the polarization is described by the orientation of $\vec{E}(\vec{r},t)$ and the ellipticity, such that special cases, like linearly or circularly polarized light can occur.

In general, polarization influences the interaction between light and matter and some examples are:

1. The polarization influences the amount of light reflected and transmitted on a boundary, for instance in polarizing beam splitters. Another example are Brewster-cut wedges or crystals, which are discussed in more detail in 3.4.3.

2. The index of refraction in anisotropic media is polarization dependent. Two waves with distinct polarizations will have different travel velocities, which, for instance, causes unwanted walk-off effects as discussed in 3.4.3.

3. Waves with different polarizations will also experience different phase shifts in an anisotropic material. This can be used to actively alter the polarization state, e.g. from elliptical polarization to linear polarization, which is used in the length stabilization system of the resonators, as described in 3.5.1.

4. Lastly, non-linear crystals require certain types of polarization in order to exhibit effects like frequency-conversion. For example, the herby used LBO and BBO both require a special type of polarization to generate a second harmonic wave with twice the frequency. This is further discussed in the sections on the LBO 3.3.4 and the BBO 3.4.3.

1.2.1. Mathematical Description of Polarization

In the following, the paraxial regime is assumed. A plane wave with frequency ν is traveling with a velocity c along the z-axis, such that its electric field is in the xy-plane:

$$\vec{E}(z,t) = Re\left[\vec{A}e^{2\pi i\nu(t-z/c)}\right] \tag{1.16}$$

with the complex envelope

$$\vec{A} = A_x\vec{x} + A_y\vec{y}. \tag{1.17}$$

The polarization can then be described by the time evolution of the endpoint of the electric field vector $\vec{E}(z,t)$. By expressing the complex components with respect to their magnitudes and phases ($A_x = a_x e^{i\varphi_x}$, $A_y = a_y e^{i\varphi_y}$) and substituting 1.17 back into 2.13, the following two expressions for the x- and y-components of the vector $\vec{E}(z,t)$ can be found:

$$E_x = a_x \cos\left[2\pi\nu(t - z/c + \varphi_x)\right] \tag{1.18}$$
$$E_y = a_y \cos\left[2\pi\nu(t - z/c + \varphi_y)\right] \tag{1.19}$$

The expressions for the electric field components E_x, E_y from equation 1.18 and 1.19 are useful to describe the different types of polarizations:

1. **Linearly polarized** light occurs whenever one of the two complex amplitude components vanishes $a_x = 0$ or $a_y = 0$, or when the phase difference is a multiple integer of π, such that $\Delta\varphi = \varphi_y - \varphi_x = n\pi$. This is a degenerate case in which the electromagnetic field of the light is confined in one plane.

2. **Circularly polarized** light arises if the amplitudes have the same size $a_x = a_y = a$ and the phase difference is exactly $\Delta\varphi = n\pi/2$. This can be simply seen by taking the square of the electric field components from equation 1.18 and 1.18. This yields $E_x^2 + E_y^2 = a^2$, which is the mathematical description of a circle.

3. **Elliptically polarized** light arises when the electric field components E_x and E_y differ in phase and/or amplitude.

Special Case: Linearly Polarized Light

For this thesis, mainly linearly polarized light is relevant, except for the length stabilization technique of the cavities, where elliptically polarized light is used briefly 3.5.1. Two linear polarization states are said to be orthogonal, whenever the inner product of the complex envelope vectors of two beams $\vec{A}_1$ and $\vec{A}_2$ vanishes

$$A_{x,1}A_{x,2}^* + A_{y,1}A_{y,2}^* = 0 \tag{1.20}$$

with $\vec{A}_i = A_{x,i}\vec{x}_i + A_{y,i}\vec{y}_i$.

In the following section, four different reference systems are introduced, which are all relevant in the upcoming chapters.

1. In the context of the laboratory environment, it is common to use the terms **horizontal** and **vertical** polarization. For horizontally polarized light, the electric

field vector $\vec{E}(z,t)$ is parallel to the optical table and perpendicular to the direction of the beam propagation $\vec{k}$. Whereas, vertically polarized light is perpendicular to the vector of h-polarized light and the direction of $\vec{k}$.

2. For further discussions on birefringent effects, which occur in anisotropic media, as well as the polarization dependence of reflection and refraction on surfaces, it is useful to introduce the terms **transverse electric (TE)** and **transverse magnetic (TM)** polarization. For TE-polarized light, the electric field is orthogonal to the plane of incidence, such that its vector points into the direction of the x-axis, as visualized in figure 1.2a. Often it is also referred to as **s-polarization**. If the electric field is parallel to the incidence plane, it is called transverse magnetic (TM) or **p-polarized**. In figure 1.2a it is shown by the arrow in the y-direction.

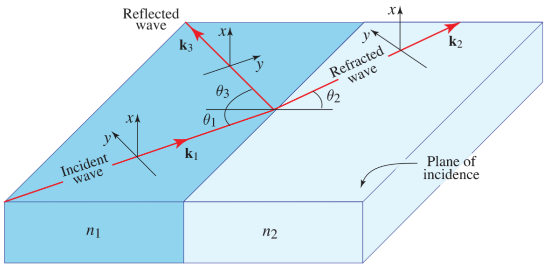

(a) Reflection and refraction at the intersection between two media with different refractive indices.

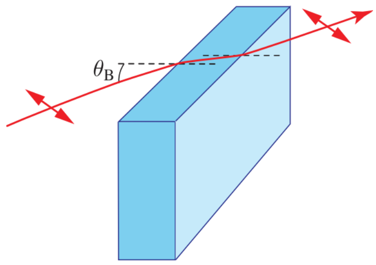

(b) Transmission of TM-polarized light through a Brewster cut wedge.

Figure 1.2.: a) Transverse electric polarized light is orthogonal to the plane of incidence (x-axis). Whereas, light with transverse magnetic polarization lies in the plane of incidence (y-axis).
b) Transverse magnetic polarized light will be transmitted through a Brewster cut wedge without reflection losses. Figures taken from [10].

3. In terms of the reference system of uniaxial crystals, it is necessary to distinguish between **ordinary** and **extraordinarily** polarized light. Uniaxial crystals will be discussed further in the chapter on the BBO crystal 3.4.3. For now, it is sufficient to know that uniaxial crystals have a single optical axis. The ordinary wave sees the same refractive index n_0 within the medium, independent of the angle θ, which is enclosed by the direction of propagation of the beam $\vec{k}$ and the optical axis of the crystal. Whereas, the extraordinary polarized wave will see a varying refractive index $n(\theta)$, depending on the enclosed angle θ. [10]

4. The last important distinction is between the **tangential** and the **sagittal** plane. With respect to optical elements, one can define a symmetry axis. For a spherical lens, it is the surface normal. The tangential plane contains the symmetry axis of

the optical element and the beam itself. The sagittal plane is orthogonal to the tangential plane and also contains the plane of the light beam, as seen in figure 1.3.

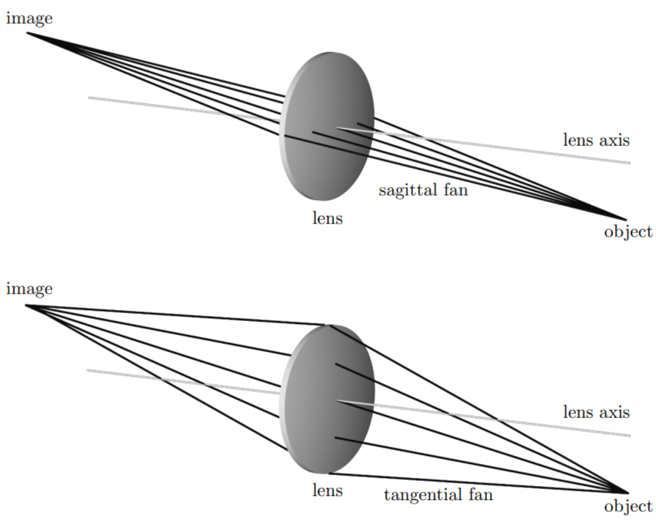

Figure 1.3.: The tangential plane contains the plane of the optical system and the off-axis beam. Whereas, the sagittal plane is orthogonal to the tangential plane and also includes the off-axis beam. Figure taken from [11].

In the experimental setup, which is presented in this thesis, some reference systems overlap such that the different expressions can be used as synonyms. It is important to note that this is a special case and in general the reference systems do not have to coincide. Table 1.4 gives an overview of the reference system and the name conventions:

Reference System	Naming Convention for Polarization	
Laboratory System	Horizontal	Vertical
Crystal Reference System	Ordinary	Extraordinary
Plane of Incidence	Transverse Electric (TE) / s-polarized	Transverse Magnetic (TM) / p-polarized

Figure 1.4.: Summary of the different reference systems and their naming conventions for the orthogonal polarizations. This is a special case applicable to the setup of this thesis, in the general case they do not have to coincide.

1.2.2. Brewster Angle

For a laser beam, that is propagating from air into a medium, for instance a crystal, the refractive indices are given by n_{air} and n_c, respectively. At the Brewster angle, surface reflections are eliminated for light with ordinary polarization. The Brewster angle is defined as [10]:

$$\theta_B = \tan^{-1}\left(\frac{n_c}{n_{\text{air}}}\right) \tag{1.21}$$

1.3. Resonator Theory

In the previous section 1.1.2, it was already shortly discussed that after a full round-trip, the field distribution has to replicate itself ($q_1 = q_2$) 1.12. Another requirement that power can build up inside resonators, is that the phase is also the same after a round trip. This is the case for phase shifts $\delta = 2\pi n$, which are integer multiples of 2π. Only in this case, the fields can interfere constructively, and intensity can be built up. [11]

Now, it will be discussed how a wave is coupled into a cavity, such that it fulfills the self-consistency criterion, how many round trips the light makes, and also how it is extracted from the cavity. For this, one needs to consider everything that affects the energy and power of the intra-cavity field. It includes the discussion on Fresnel reflection losses on the mirrors and other elements inside the cavity, as well as dissipative losses, such as absorption or scattering.

1.3.1. Mode Matching

Mode matching describes the process of ensuring that the spatial characteristics of the input beam are aligned to the cavity eigenmodes. In general, optical cavities support different modes, such as Gaussian TEM_{00}-, higher-order Hermite Gaussian or Laguerre Gaussian modes. The most desired mode is the lowest-order Gaussian (TEM_{00}), since it has the best beam quality and the lowest losses.

The mode-matching problem includes shaping the input beam such that its waist size and location matches the size and location of the natural cavity mode waist. One or two lenses can be used to perform this task. The disadvantage of using a single lens is that for a given focal length f, the distances d_1, d_2 between the lens and the two waists w_1, w_2, are fixed. This does not allow for any flexibility or adjustments later on. In practice, it is more advantageous to use two lenses. The initial waist w_1 and the cavity incoupling waist w_c are fixed parameters. For appropriately chosen focal lengths f_1 and f_2, the two-lens approach allows one to change the distances d_1, d_2, d_3 afterwards and find the best positions for optimal mode-matching, as seen in figure 1.5.

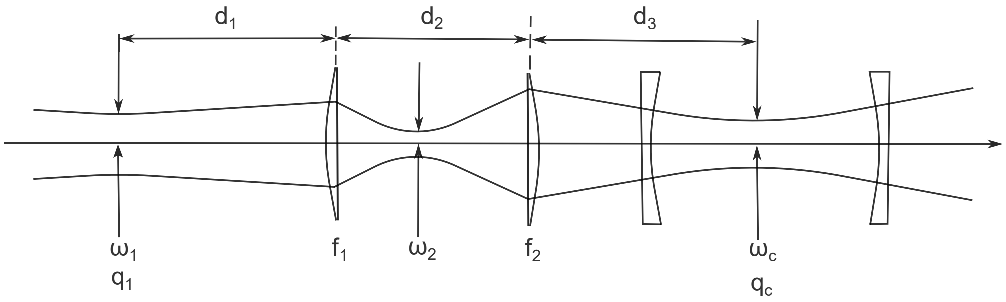

Figure 1.5.: Phase-matching by two lenses with focus lengths f_1 and f_2 allows for more flexibility in later alignment.

The following paragraph will focus on the parameter transformation given by a lens with focal width f, which maps a waist w_0 at position z with Rayleigh range z_0 to a waist size of w_0' at position z' with Rayleigh range z_0'. The naming convention is based on figure 1.6.

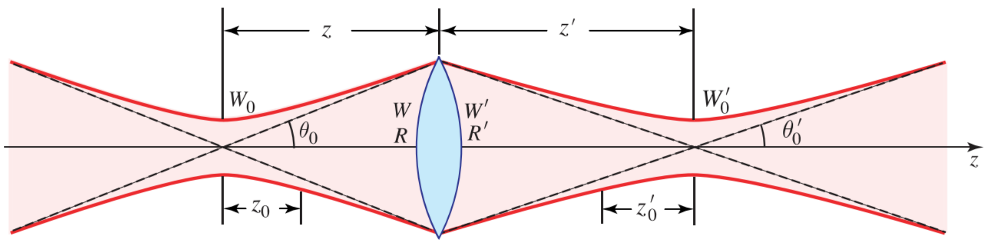

Figure 1.6.: Parameter transformation defined by a thin lens with focal width f. Figure taken from [10].

After passing through a lens, the initial waist w_0 will magnified to a waist size of w_0'

$$w_0' = M w_0 \tag{1.22}$$

by the magnification factor M

$$M = \frac{M_r}{\sqrt{1+r^2}} \tag{1.23}$$

where

$$M_r = \left| \frac{f}{z-f} \right| \tag{1.24}$$

$$r = \frac{z_0}{z-f}. \tag{1.25}$$

The positions of the waists are related to each other by equation 1.26

$$(z' - f) = M^2(z - f). \tag{1.26}$$

Until now, only the eigenmodes of the cavity have been discussed, which depend solely on the geometry of the resonator and the wavelength of the input wave. In the following chapters, it will be discussed, how many round-trips the light makes and how much power is built up. For that, one needs to consider everything that affects the energy of the circulating field, which includes reflection losses on the mirrors and the crystal, as well as dissipative losses.

1.3.2. Circulating Power

The analysis of a traveling wave bow-tie cavity is analogous to the case for a two-mirror standing wave resonator. One requirement is that all intra-cavity mirrors (except for the incoupling mirror) are highly reflective. The transmissivity and reflectivity of the incoupling mirror are indicated by t_1 and r_1. The relation between the input field E_0 and the circulating electric field E_c is given by equation 1.27, where δ is the acquired phase shift after a full round-trip.

$$\frac{E_c}{E_0} = \frac{t_1}{1 - r_1 r_m e^{-i\delta}} \tag{1.27}$$

Using the quadratic relation between the electric field and the intensity $I_c = |E_c|^2$, as well as the trigonometric relation $\cos(\delta) = 1 - 2\sin^2(\delta/2)$, gives:

$$\frac{I_c}{I_0} = \frac{t_1^2}{(1 - r_1 r_m)^2 + 4 r_1 r_m \sin^2(\delta/2)} \tag{1.28}$$

A derivation of 1.28 can be found in various textbooks, like in [11]. Equation 1.28 shows that the maximum circulating intensity I_c can be achieved if the acquired phase shift is an integer multiple n of 2π: $\delta = n\pi$. The parameter r_m includes the reflectivities of the cavity mirrors r_2, r_3, r_4 (as seen from figure 3.8 and 3.10), as well as a transmission coefficient t, which models all Fresnel losses and dissipative losses of the mirrors and the crystal:

$$r_m = r_2 r_3 r_4 t \tag{1.29}$$

The transmission coefficient for a crystal with absorption coefficient α_l and length l_c is calculated by $t = e^{-\alpha_c l_c}$. r_m can also be interpreted as the fraction of the light field that remains inside the cavity after a full round trip (excluding the incoupling transmission t_1). The behavior of the normalized circulating intensity is visualized in figure 1.7. It shows the evolution for some exemplary values, as well as the cavity-specific cases, which are presented in the thesis.

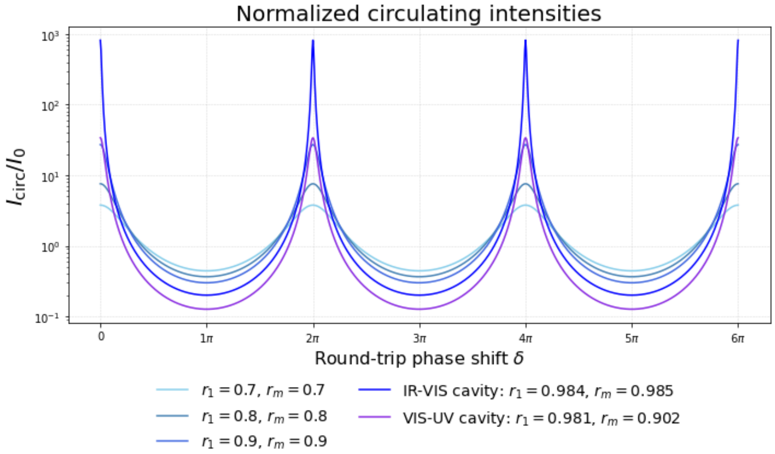

Figure 1.7.: Normalized circulating intensities with respect of the phase shift δ that is acquired during a full round-trip inside the cavity, according to equation 1.28

Similar expressions for the reflected field E_r and the reflected intensity I_r can be found:

$$\frac{E_{\mathrm{refl}}}{E_0} = \frac{r_m e^{-i\delta} - r_1}{1 - r_1 r_m e^{-i\delta}} \tag{1.30}$$

$$\frac{I_{\mathrm{r}}}{I_0} = \frac{(r_1 - r_m)^2 + 4 r_1 r_m \sin^2(\delta/2)}{(1 - r_1 r_m)^2 + 4 r_1 r_m \sin^2(\delta/2)} \tag{1.31}$$

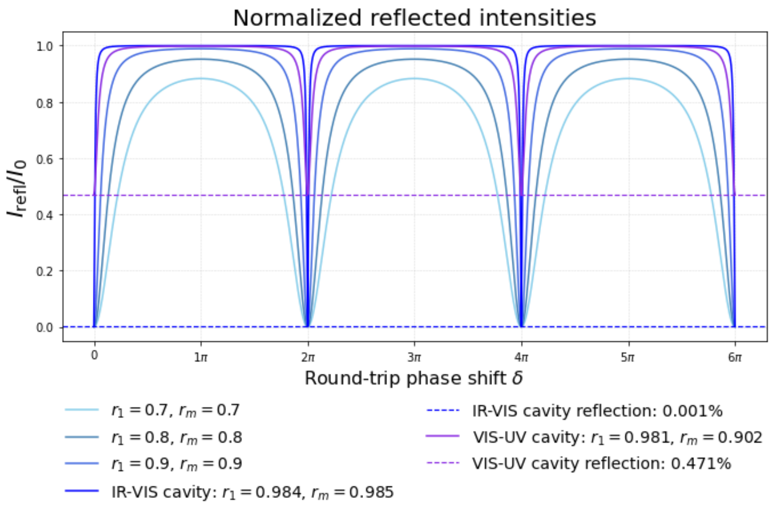

Figure 1.8.: Normalized reflected intensity with respect of the phase shift δ that is acquired during a full round-trip inside the cavity, according to equation 1.31.

The qualitative behavior of the normalized reflected intensity is visualized in figure

1.8. Again, it shows some characteristic examples as well as the two cavity-specific cases, which are presented in this thesis.

Figures 1.8 and 1.7 show that for a phase-shift of $\delta = 2\pi n$, where n has integer values, the reflected intensity nearly vanishes and the circulating intensity reaches its highest peak.

1.3.3. Finesse

In the following, the the behavior of the light's intensity is discussed near resonance $\delta \approx 2\pi n$ for integer values of n. From equation 1.28, the half maximum intensity can be derived, which occurs at the phase $\delta_{1/2}$ given by equation 1.32

$$\delta_{1/2} = 2\sin^{-1}\left(\frac{1 - r_1 r_m}{2\sqrt{r_1 r_m}}\right) \approx \frac{1 - r_1 r_m}{\sqrt{r_1 r_m}}. \tag{1.32}$$

The approximation has been done under the assumption that $\delta_{1/2} \ll 1$. This is justified by the fact that the finesse $\mathcal{F}$ of most cavities is $\mathcal{F} \gg 1$, such that $\delta_{1/2} \gg \pi$. A description of the finesse is given in the following paragraphs. On resonance, the full width half maximum (FWHM) $\Delta\nu_{1/2}$ of the circulating light field is given by [11]:

$$\text{FWHM} = \Delta\nu_{1/2} = 2\delta_{1/2} = \frac{2(1 - r_1 r_m)}{\sqrt{r_1 r_m}} \tag{1.33}$$

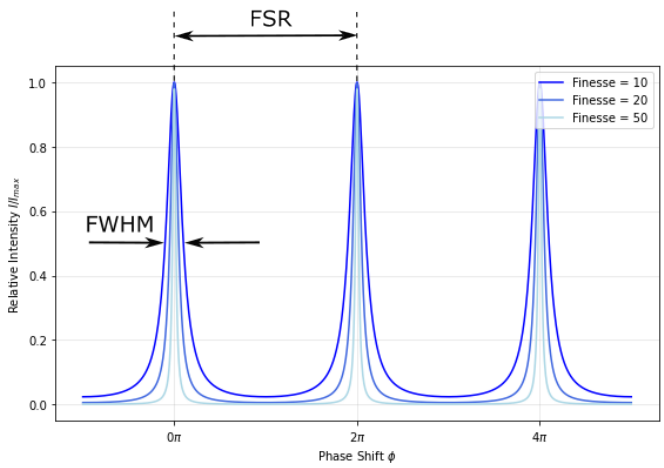

Figure 1.9.: From the transmission peaks of a resonator, the full width half maximum (FWHM) and the free spectral range (FSR) of a cavity can be obtained, which define the overall finesse.

From the condition, that the round-trip phase-shift has to satisfy $\delta = 2\pi n$, the resonance frequency of a resonator can be derived. Using that the wavevector k is defined by $k = 2\pi/\lambda = 2\pi\nu/c$ and the round-trip phase for a resonator with length L is $\delta = kL$, it follows that

$$\nu_n = \frac{nc}{L} \tag{1.34}$$

for integer values of m. In other word, only certain discrete frequencies ν_m satisfy the resonance condition such that $\delta = 2\pi n$. [10]

This leads to the definition of the free spectral range (FSR). It describes the axial mode spacing of the cavity eigenmodes and is given by equation 1.35, where L is the round trip length of the resonator.

$$FSR = \frac{c}{L} \tag{1.35}$$

A detailed derivation of the FSR can be found in [11] or [10], which is based on the supported eigenmodes of the resonator. For better understanding, the transmission peaks for a cavity are visualized by figure 1.9, from which the bandwidth and the FSR of the resonator can be evaluated.

The finesse $\mathcal{F}$ can then be defined as the ratio between the FSR and the FWHM, as described by equation 1.36. If $r_1 = r_m = r_2r_3r_4$ for the reflectivities of the incoupling mirror r_1 and the remaining cavity mirrors $(r_2r_3r_4)$ it can be simplified to:

$$\mathcal{F} = \frac{FSR}{\Delta\nu_{1/2}} = \frac{\pi\sqrt{r_1 r_m}}{1 - r_1 r_m} = \frac{\pi\sqrt{R}}{1 - R} = \frac{\pi}{\delta_{1/2}} \tag{1.36}$$

$\mathcal{F}$ is a quantity, which gives a relation between how narrow the resonances are with respect to the mode spacing. Basically, it is defined by the losses within the resonator and does not depend on the length of the cavity. For maximum intra-cavity power enhancement, a high finesse is desirable. A formula for the maximum intensity built-up inside a resonator can be derived by summing over all waves, which are traveling inside of the cavity. The resulting wave is a superposition of the individual waves, whose amplitudes are geometrically reduced due to losses inside the resonator. A detailed derivation can be looked up in [10]. The resulting intra-cavity intensity is found to be:

$$\frac{I}{I_{\max}} = \frac{1}{1 + (2\mathcal{F}/\pi)^2 \sin^2(\varphi/2)} \tag{1.37}$$

From equation 1.37 and figure 1.9 it can be seen, that the intensity is a periodic function with $2\pi n$ for integer values of n.

1.3.4. Impedance Matching

Taking a closer look on equation 1.28 indicates that the circulating intensity is maximized on resonance $\delta = 2\pi n$, meaning that there is no phase shift between the circulating light fields.

At this point, it is useful to switch to the notation by the intensity coefficients for the reflectivity R_i and the transmission T_i, instead of the amplitude coefficients r_i and t_i, for $i \in [1,2,3,4] : R_i = r_i^2, T_i = t_i^2$. On resonance, the normalized circulating power P_c becomes:

$$\frac{P_c}{P_0} = \frac{T_1}{(1-\sqrt{R_1 R_m})^2} \tag{1.38}$$

The impedance matching condition 1.39 can be obtained by evaluating the maximum of the circulating intensity from equation 1.28 ($\partial I_c/\partial r_1 = 0$ for $\delta = 0$):

$$r_1 = r_m \tag{1.39}$$

Using the energy conservation criterion $R_1 + T_1 = r_1^2 + t_1^2 = 1$ and inserting the impedance matching condition 1.39 into **??**, yields that all intra-cavity losses L have to be equal to the transmission of the incoupling mirror t_1: $L = t_1^2$.

Summarizing the above observations: Firstly, the impedance matching condition is fulfilled when the transmission of the incoupling mirror t_1^2 is equivalent to all cavity losses L. Secondly, on resonance ($\delta = 2\pi n$), the circulating power will be maximized. [11]

The circulating field inside the cavity must remain in an equilibrium state. During every round-trip the amplitude of the light field decreases due to scattering, reflection, absorption, or conversion during the SHG-process. In order to maintain an equilibrium condition, the losses have to be compensated for by the incoming field. This condition is visualized in figure 1.10, based on equation 1.38. For the simulation, losses which resulted from conversion were neglected. It shows the relative circulating power that is obtained for different configurations of the incoupling reflectivity R_1 and the resonator reflectivity R_m. From figure 1.10 it can be seen that the circulating power P_c can be higher than the input power P_0. Also, it shows that maximum power enhancement can be obtained when the impedance matching condition from equation 1.10 is fulfilled and if the total resonator reflectivity $R_m \to 1$. It is therefore necessary to minimize the resonator losses as much as possible. For an intra-cavity reflectivity $R_m = 0.99$, the input power can be enhanced by nearly a factor of 100.

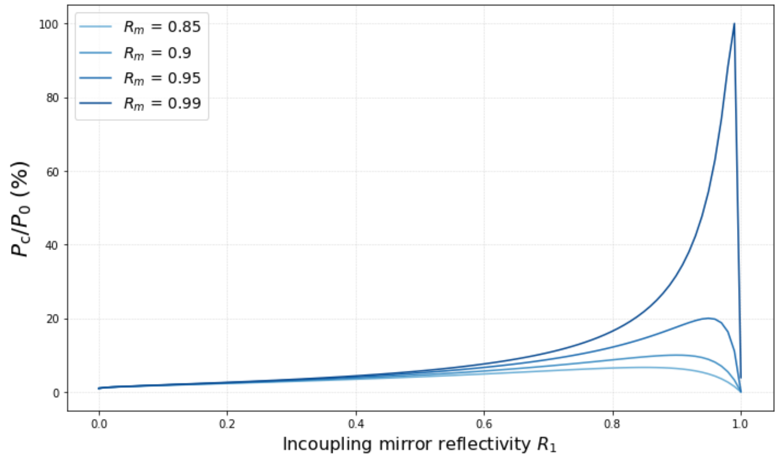

Figure 1.10.: Relative circulating power on resonance ($\delta = 2\pi n$), for integer values of n. Conversion losses are neglected. The greatest power enhancement can be achieved for $R_m \to 1$ and if the impedance matching condition 1.39 is fulfilled.

In practice, impedance-matching is achieved by choosing an incoupling mirror with the right transmission T_1, such that the cavity losses are compensated for. When the losses during the SHG-conversion are taken into account, the magnitude of the input power has to be considered when choosing the right incoupler. With increasing pump powers, the conversion losses within the crystal also increase due to thermal effects or the formation of color centers. In that case, the transmission of the incoupler has to be greater to compensate for the losses compared to smaller input powers. [11]

1.3.5. Astigmatism

One disadvantage of traveling wave resonators is the presence of astigmatic effects, because the setup requires tilted mirrors. A traveling wave resonator is constructed such, that the wave in continuously traveling, instead of constantly bouncing back and forth between a simple two-mirror Fabry-Perot cavity. Astigmatism describes the condition when an optical system focuses the x- and y- component of one beam onto different positions, as seen from figure 1.3. This causes a distortion of the resonator mode and prevents a circular Gaussian beam profile. In general, geometric aberration is introduced because of rays, which are reflected off-axis, which happens whenever optical elements are tilted with respect to the symmetry axis. This requires, that the tangential and sagittal planes need to be treated independently. In general, any cause of astigmatism will reduce the effective stability range of a cavity. In the following, two origins for astigmatism in the hereby used resonators are discussed:

1. For a mirror that is tilted by an angle θ with respect to the optical axis, the beams see different effective radii of curvature: $R_{\text{eff, t}} = R\cos(\theta)$ and $R_{\text{eff, s}} = R/\cos(\theta)$.

2. Tilted intra-cavity crystals are an additional origin of astigmatism. For a Brewster-cut crystal with length l_c, refractive index n_c, the effective crystal length l_{eff} differs for rays in the tangential and sagittal plane, such that $l_{eff,t} = l_c/n_c$ and $d_{eff_s} = l_c/n_c^3$.

Those two sources for astigmatic effects can be used to compensate each others effects. By appropriately choosing all tilting angles, it can either circularize the mode at the incoupling position, which can improve the incoupling efficiency - or it can circularize the mode at the crystal position, which might favor the second-harmonic conversion. [11]

2. Introduction to Non-Linear Optics

A medium is characterized as linear if there is a linear dependence between the polarization density $\vec{P}$ and the light's electrical field $\vec{E}(\vec{r},t)$, with the vacuum permeability ϵ_0 and the electric susceptibility χ: [10]

$$\vec{P}(\vec{r},t) = \epsilon_0 \chi \vec{E}(\vec{r},t) \tag{2.1}$$

With the invention of the first laser by Maiman [24] in 1960, one was able to study the interaction of high-intensity light fields with optical media in more detail. The experimental results showed that: The index of refraction changes with the light's intensity, light beams can interact with each other, and the light's frequency can be changed when surpassing an optical medium.
Even when focused laser light is used, the external optical field $\vec{E}$ is still small, compared to the crystalline fields inside an optical medium. [10] Therefore, the relation between the polarization density $\vec{P}$ and the electric field of light $\vec{E}$ can be expanded in a Taylor expansion around $\vec{E} = 0$. The following convention is used in [10] or [25]:

$$\vec{P} = a_1\vec{E} + \frac{1}{2}a_2\vec{E}^2 + \frac{1}{6}a_3\vec{E}^3 + ... \tag{2.2}$$

$$= \epsilon_0\chi^{(1)}\vec{E} + 2d\vec{E}^2 + 4\chi^{(3)}\vec{E}^3 + ... \tag{2.3}$$

For small $\vec{E}$, the interaction can be linearly approximated, but the non-linearity increases with increasing $\vec{E}$.

An alternative nomenclature based on the index notation is used in [25], which better visualizes that the polarization density $\vec{P} = (P_1, P_2, P_3)$ depends on all three components of the $\vec{E}$-field (E_1, E_2, E_3):

$$P_i = \epsilon_0\chi_{ij}E_j + 2d_{ijk}E_jE_k + 4\chi^{(3)}_{jkl}E_jE_kE_l \tag{2.4}$$

where the indices, $i, j, k, l \in [x, y, z]$ refer to the Cartesian coordinates. The index notation also shows that the susceptibility is not a scalar but a tensor quantity of higher order.

2.1. Non-Linear Wave Equation

From Maxwell's equations for homogeneous and dielectric media, the wave equation can be derived, which describes the propagation of light through non-linear materials:

$$\nabla^2\vec{E} - \frac{1}{c_0^2}\frac{\partial^2\vec{E}}{\partial t^2} = \mu_0\frac{\partial^2\vec{P}}{\partial t^2} \tag{2.5}$$

It is useful to decompose $\vec{P}$ into its linear and non-linear components $\vec{P_{NL}}$:

$$\vec{P} = \epsilon_0 \chi^{(1)} \vec{E} + \vec{P_{NL}} \tag{2.6}$$

$$\vec{P_{NL}} = 2d\vec{E}^2 + 4\chi^{(3)}\vec{E}^3 + ... \tag{2.7}$$

Equation 2.5 can then be re-expressed as an inhomogeneous wave equation, using the following definitions $n^2 = 1 + \chi$, $c_0 = 1/(\mu_0\epsilon_0)^{1/2}$ and $c = c_0/n$ [10] :

$$\nabla^2 \vec{E} - \frac{1}{c^2}\frac{\partial^2 \vec{E}}{\partial t^2} = -\vec{S} \tag{2.8}$$

where

$$\vec{S} = -\mu_0 \frac{\partial^2 \vec{P_{NL}}}{\partial t^2}. \tag{2.9}$$

This allows to further investigate the influence of the non-linear polarization: Non-negative values of the second derivative of $\vec{P_{NL}}$ will lead to the acceleration of charges and based on Larmor's law from electrodynamics, accelerated charges radiate an electromagnetic field. Therefore, $\vec{P}$ effectively acts as a radiating source that drives an electric field $\vec{E}$. Due to the non-linearity of $\vec{S}$, the source will emit an electric field with new frequencies, compared to the frequencies of the initial field $\vec{E}$. [14], [26] This leads to many different useful effects, such as frequency doubling of the incoming light field, which is relevant for this thesis.
In the following, it is assumed that $\chi^{(2)} \gg \chi^{(n)}$ for $n \geq 3$, such that all higher-order nonlinear susceptibilities can be neglected.

2.2. Second Harmonic Generation (SHG)

In the following section, the fundamentals of Second Harmonic Generation (SHG) will be discussed. It is based on the relation between the non-linear term of the polarizability and the electric field of the light:

$$\vec{P_{NL}} = 2d\vec{E}^2 \tag{2.10}$$

The incoming electromagnetic field can be approximated as a monochromatic plane wave with the complex amplitude $E_i(\omega_i) = A_i e^{-ik_i(\omega)z}$, where A_i is the complex envelope and $k_i(\omega_i) = \omega_i/c$:

$$\vec{E(t)} = \sum_{i=1,2,3} Re\left[E_i(\omega_i)e^{i\omega_i t}\right] \tag{2.11}$$

$$= \sum_{i=1,2,3} \frac{1}{2}\left[E_i(\omega_i)e^{-i\omega_i t} + E_i(\omega_i)^* e^{i\omega_i t}\right] \tag{2.12}$$

$$\tag{2.13}$$

By inserting this definition back into equation 2.10 and using $d = \varepsilon_0 \chi^{(2)}$, the following expression is obtained:

$$\vec{P_{NL}}(t) = \varepsilon_0 \chi^{(2)} \left[\vec{E}_0 e^{-i\omega t} + \vec{E}_0^* e^{i\omega t}\right]^2 \tag{2.14}$$

$$= \varepsilon_0 \chi^{(2)} \left[2|\vec{E}_0|^2 + \vec{E}_0^2 e^{-i(2\omega)t} + \left(\vec{E}_0^*\right)^2 e^{i(2\omega)t}\right] \tag{2.15}$$

The non-linear polarizability $\vec{P_{NL}}(t)$ is a sum of a constant electric field and a complex conjugate pair, which is oscillating with twice the frequency 2ω of the incoming field. This behavior is visualized in image 2.1.

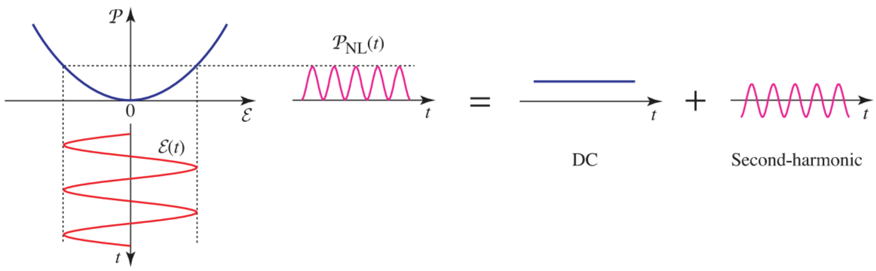

Figure 2.1.: Illustration of SHG: An input electric field with frequency ω creates a constant (DC) component and a polarization with twice the frequency 2ω. Figure taken from [10].

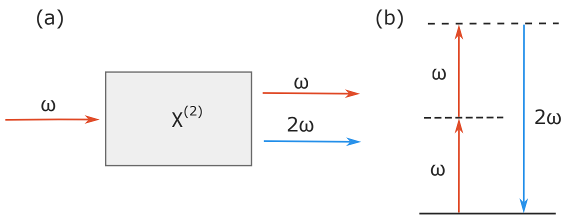

Figure 2.2.: (a) An input electric field with frequency ω interacts with a non-linear medium and generates an output field with twice the frequency 2ω. (b) The corresponding energy-levels for the SHG-process. Figure adapted from [14].

2.2.1. Coupled wave equations for three wave mixing

In order to show the importance of phase-matching ($\Delta k = k^{2\omega} - 2k^{\omega} = 0$), a closer investigation into the coupled amplitude equations for the cases of a non-depleted input beam is given.

The following prerequisites are taken: a fundamental beam is traveling along an arbitrary direction (z-direction) in a non-linear medium. Further, three different frequencies ω_1, ω_2

and ω_3 are considered and the waves are approximated as plane waves 2.13:

$$\vec{E}(t) = \sum_i \frac{1}{2} E_i e^{(i\omega_i t)}. \tag{2.16}$$

The summation is taken over $i, j = \pm 1, \pm 2, \pm 3$. Inserting 2.16 into to expressions for the non-linear polarization $\vec{P}_{NL}$ 2.10 and the radiating source $\vec{S}$ from equation 2.18, yields:

$$\vec{P}_{\mathrm{NL}}(t) = \frac{d}{2} \sum_{i,j} E_i E_j e^{i(\omega_i + \omega_j)t} \tag{2.17}$$

$$\vec{S} = \frac{\mu_0 d}{2} \sum_{i,j} (\omega_i + \omega_j)^2 E_i E_j e^{i(\omega_i + \omega_j)t} \tag{2.18}$$

Substituting the expression for the electric field 2.16, the non-linear polarization 2.17 and the source 2.18 back into the wave equation 2.5, results in the following three-wave mixing coupled wave-equations:

$$(\nabla^2 + k_1^2) E_1 = -2\mu_o \omega_1^2 d E_3 E_2^* \tag{2.19}$$

$$(\nabla^2 + k_2^2) E_2 = -2\mu_o \omega_2^2 d E_3 E_1^* \tag{2.20}$$

$$(\nabla^2 + k_3^2) E_3 = -2\mu_o \omega_3^2 d E_1 E_2. \tag{2.21}$$

Evolution of the photon flux density

For the further discussion on the evolution of the photon flux density during the frequency conversion, it is useful to introduce a new variable $a_i = A_i/\sqrt{2\eta\hbar\omega_i}$, where A_i is the amplitude of the electric field. $\eta = \eta_0/n$ is the impedance in a medium with refractive index n and the free space impedance $\eta_0 = \sqrt{\mu_0/\epsilon_0}$. The same prerequisites as in 2.2.1 are assumed. The electric field is re-expressed using the new variable a_i:

$$E_i = a_i \sqrt{2\eta\hbar\omega_i} e^{-ik_i z}, \quad i = 1, 2, 3 \tag{2.22}$$

The photon flux density (photons/ms^2) of the individual waves is then defined as

$$\phi_i = \frac{I_i}{\hbar\omega_i} = |a_i|^2 \tag{2.23}$$

where $I_i = |E_i|^2/2\eta = \hbar\omega_i |a_i|^2$ is the corresponding intensity of the beams. For weak interactions between the waves one can assume $a_i(z) = a_i$ to be constant and further use an approximation for slowly varying envelopes: $d^2 a_i/dz^2 \ll k_i da_i/dz = (2\pi/\lambda_i) da_i/dz$ such that

$$(\nabla^2 + k_i^2)[a_i e^{-ik_i z}] \approx -i2k_i \frac{da_i}{dz} e^{-ik_i z}. \tag{2.24}$$

With the slowly varying wave approximation, the coupled amplitude equations 2.19 - 2.21 reduce to

$$\frac{da_1}{dz} = -iga_3a_2^*e^{-i\Delta kz} \tag{2.25}$$
$$\frac{da_2}{dz} = -iga_3a_1^*e^{-i\Delta kz} \tag{2.26}$$
$$\frac{da_3}{dz} = -iga_1a_2e^{-i\Delta kz} \tag{2.27}$$

with

$$g^2 = 2\hbar\omega_1\omega_2\omega_3\eta^3d^2. \tag{2.28}$$

The evolution of the complex envelopes a_i is therefore described by three coupled first-order differential equations 2.25 - 2.27. A solution to those equations is given in the following chapter for the special case of second harmonic generation.

2.2.2. Solutions for Second Harmonic Generation

In the case of SHG, two frequencies are degenerate, $\omega_1 = \omega_2 = \omega$ and $\omega_3 = 2\omega$ and only two waves with the amplitudes E_1 and E_3 are involved. The coupled wave equations 2.19 - 2.21 reduce to:

$$(\nabla^2 + k_1^2)E_1 = -2\mu_o\omega_1^2dE_3E_1^* \tag{2.29}$$
$$(\nabla^2 + k_3^2)E_3 = -\mu_o\omega_3^2dE_1E_1. \tag{2.30}$$

It is important to add, that equations 2.29 and **??** were not simply obtained by plugging $E_1 = E_2$ into the initial Helmholtz equations 2.19 - 2.21. Note that the factor of 2 is absent in 2.30. By applying the slowly varying wave approximation to equations 2.29 and 2.30, the following coupled wave equations can be obtained

$$\frac{da_1}{dz} = -iga_3a_1^* \tag{2.31}$$
$$\frac{da_3}{dz} = -i\frac{g}{2}a_1^2 \tag{2.32}$$

where perfect phase-matching ($\Delta k = 0$) was assumed. With the boundary conditions that the second-harmonic wave is zero in the beginning $a_3(z=0) = 0$, the fundamental wave is real $a_1(0) \in \mathbb{R}$ and that the total number of photons is conserved $|a_1(z)|^2 + 2|a_3(z)|^2 = \text{const.}$, the following solutions can be obtained

$$a_1(z) = a_1(0)\,\text{sech}\left(\frac{1}{\sqrt{2}}ga_1(0)z\right) \tag{2.33}$$
$$a_3(z) = -\frac{j}{\sqrt{2}}a_1(0)\tanh\left(\frac{1}{\sqrt{2}}ga_1(0)z\right). \tag{2.34}$$

Using relation $\phi_i(z) = |a_i(z)|^2$ from equation 2.23, the photon flux densities for the fundamental and the harmonic wave are

$$\phi_1(z) = \phi_1(0)\,\mathrm{sech}^2\left(\frac{\gamma z}{2}\right) \tag{2.35}$$

$$\phi_3(z) = \frac{1}{2}\phi_1(0)\tanh^2\left(\frac{\gamma z}{2}\right) \tag{2.36}$$

where $\gamma/2 = ga_1(0)/\sqrt{2}$. The behavior of the photon flux densities is visualized in figure 2.3, showing that the fundamental photons are converted into second-harmonic ones. Notably, the number of converted photons can never exceed half of the input photons because of energy conservation.

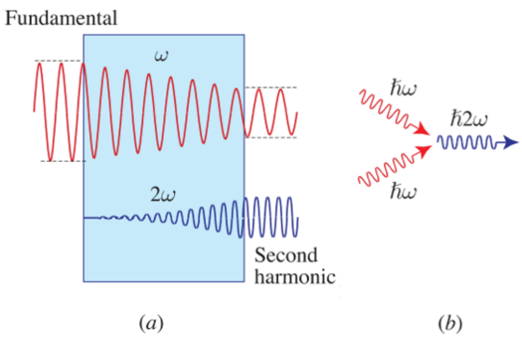

Figure 2.3.: (a) Interaction of a fundamental wave with a non-linear medium to generate second-harmonic light. (b) Energy conservation in the SHG process. Figure adapted from [10]

Conversion Efficiency and Effect of Phase-Mismatch

The second-harmonic conversion efficiency is given by the intensity of the harmonic light after an interaction length L and the fundamental input intensity:

$$\eta_{\mathrm{SHG}} = \frac{I_3(L)}{I_1(0)} = \frac{\hbar\omega_3\phi_3(L)}{\hbar\omega_1\phi_1(0)} = \frac{2\phi_3(L)}{\phi_1(0)} = \Phi_1(0)\frac{g^2L^2}{2}\,\mathrm{sinc}^2\left(\frac{\Delta kL}{2}\right). \tag{2.37}$$

Equation 2.37 applies to the weak-coupling regime, in which either the interaction length L is short, the non-linear parameter d is small or the input field weak. Further, a phase-mismatch is assumed such that $\Delta k \neq 0$. For those prerequisites the small varying wave approximation can again be applied, since the input field only changes slightly with the distance such that $a_1(z) \approx a_1(0)$. The qualitative behavior of the conversion efficiency is visualized in figure 2.4. It reaches its maximum for $\Delta k = 0$, shows a fast drop for increasing values of Δk and even reaches zero for $|\Delta k| = 2\pi/L$.

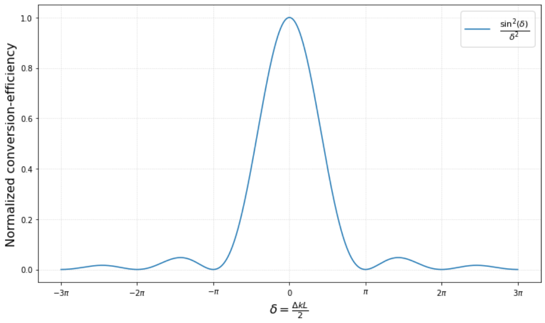

Figure 2.4.: Normalized conversion efficiency with respect to the phase-mismatch Δk.

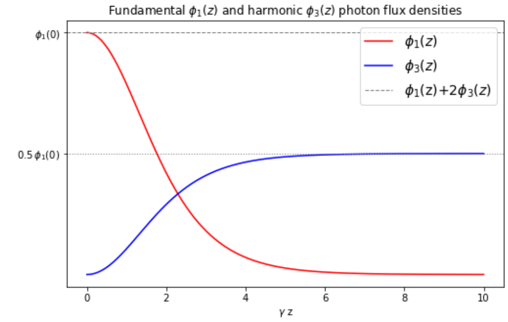

Figure 2.5.: Evolution of the photon flux densities of the input $\phi_1(z)$ and the output beam $\phi_3(z)$.

Equation 2.37 shows that for a given crystal length L, even a small phase-mismatch Δk can greatly reduce the conversion efficiency.

The maximum useful crystal length is limited by the coherence length l_c in equation 2.38:

$$l_c = \frac{2\pi}{\Delta k} = \frac{2\pi}{k^{(2\omega)} - 2k^{(\omega)}} \tag{2.38}$$

In chapter 2.4, the optimal crystal length for maximum conversion efficiency will be discussed in more detail [25], [10], [22], [14].

2.3. Techniques for Phase-Matching

As seen from equation 2.37, high conversion efficiencies can be achieved for $\Delta k = 0$. In the context of Second Harmonic Generation, this corresponds to $k^{2\omega} = 2k^{\omega}$, for $k^{\omega} = \omega[\epsilon(\nu)\mu_0]^{1/2} = n(\nu)k_0$, where $\epsilon(\nu)$ is the frequency-dependent electric permittivity and μ_0 the vacuum permeability. The most general phase-matching requirement is given by equation 2.39, which means that the refractive indices of the fundamental and SHG beams have to be equal.

$$n^{2\omega} = n^{\omega} \tag{2.39}$$

Otherwise, destructive interference between harmonic waves, which are generated at different positions within the crystal, will reduce the overall conversion efficiency. The most commonly used techniques for phase-matching are angle and temperature tuning of the crystal, which are also called critical and non-critical phase-matching. In the following, only critical phase-matching will be discussed, since this is the method used in this thesis.

2.3.1. Type I and II Phase-Matching

In both, type-I and -II phase-matching, the birefringence of an anisotropic crystal is used to match the phase velocities of the fundamental and harmonic beams via angle tuning of the crystal. The input waves can either have the same or orthogonal polarizations. The specific case, where the fundamental waves have the same polarization, is also referred to as **type-I phase-matching**. In uniaxial crystals, the fundamental beams can either have ordinary or extraordinary polarization.

In a birefringent material, light is split up into two polarization components, which travel at different velocities. The ordinary ray is polarized perpendicular to the optical axis and always sees the refractive index n_o. Whereas, light with extraordinary polarization is polarized in the plane that contains the wave vector and the optical axis. It will see an angle-dependent refractive index $n_e(\theta)$.

Regarding phase-matching, it allows distinguish between two cases: o-o-e or e-e-o processes within the crystal. This means that two photons with the same frequency ω and the same polarization are combined to generate one photon with twice the frequency 2ω and orthogonal polarization:

$$k_{\omega,o} + k_{\omega,o} \rightarrow k_{2\omega,e} \quad \text{(o-o-e process)} \tag{2.40}$$

$$k_{\omega,e} + k_{\omega,e} \rightarrow k_{2\omega,o} \quad \text{(e-e-o process)} \tag{2.41}$$

In the case, that the fundamental waves have orthogonal polarizations and still the same frequency ω, it is called **type-II phase-matching**:

$$k_{\omega,e} + k_{\omega,o} \rightarrow k_{2\omega,e} \quad \text{(e-o-e process)} \tag{2.42}$$

$$k_{\omega,e} + k_{\omega,o} \rightarrow k_{2\omega,o} \quad \text{(e-o-o process)} \tag{2.43}$$

In the following, only type I critical phase-matching will be further discussed, since this is the method that is used in this thesis.

2.3.2. Critical Phase-Matching

As mentioned above, critical phase-matching uses the effect of birefringence, also called double refraction, which is exhibited by anisotropic crystals. The mathematical description is slightly distinct for uniaxial or biaxial crystals. The case is simpler for uniaxial crystals, since they only have a single optical axis and therefore one possible phase-matching angle θ, where θ is the angle between the optical axis of the crystal (z-axis) and the direction of propagation of the light. For biaxial crystals, the description and calculation become more involved, since they have two optical axes. This additional degree of freedom allows for many possible configurations of the two phase matching angles θ_m and ϕ_m.[10]

Type I Critical Phase-Matching for Uniaxial Crystals

In uniaxial crystals, light with ordinary (orthogonal) polarization sees the same refractive index n_o, independent of the angle θ. However, extraordinary polarized waves will see a different value of the refractive index $n_e(\theta)$ depending on the angle θ.

A formula for the phase-matching angle in uniaxial crystals can be derived by inserting the phase-matching condition

$$n_e^{2\omega}(\theta_{\mathrm{pm}}) = n_0^{\omega} \tag{2.44}$$

into equation 2.45

$$\frac{1}{(n_o^{\omega})^2} = \frac{\cos^2\theta_{\mathrm{pm}}}{(n_o^{2\omega})^2} + \frac{\sin^2\theta_{\mathrm{pm}}}{(n_e^{2\omega})^2}. \tag{2.45}$$

Solving it for θ_{pm} yields the following expression for the phase-matching angle, where n_o^{ω} and n_e^{ω} give the principal values of the refractive indices for ordinary and extraordinary polarized beams [10], [25]:

$$\theta_{\mathrm{pm}} = \cos^{-1}\sqrt{\frac{\left(\frac{1}{n_o^{\omega}}\right)^2 - \left(\frac{1}{n_o^{2\omega}}\right)^2}{\left(\frac{1}{n_e^{2\omega}}\right)^2 - \left(\frac{1}{n_o^{2\omega}}\right)^2}} \tag{2.46}$$

Figure 2.6 shows the projections of the refractive indices of the ordinary and extraordinary waves at the fundamental (ω) and second-harmonic frequency (2ω) for a negative uniaxial crystal. In graphic 2.6 (c) both projections are overlapped to find the phase-matching angle θ. This is the case, where $n_o(\omega)$ (solid blue circle) intersects with $n_e(2\omega)$ (dashed red ellipse), so that $n_o(\omega) = n_e(2\omega)$. Two fundamental light beams with ordinary polarization are combined into a second harmonic beam with extraordinary polarization $o(\omega) + o(\omega) \rightarrow e(2\omega)$. The idea for figure 2.6 is based on the graphic by [27].

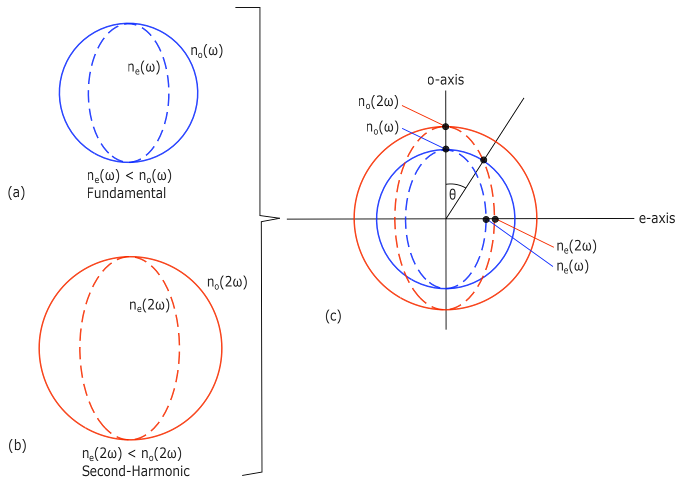

Figure 2.6.: Type-I critical phase-matching for o-o-e processes in negative uniaxial crystals $n_e < n_o$. (a) The projection of the refractive indices at the fundamental and (b) second-harmonic frequency. (c) Overlap of the projections from (a) and (b) to find the phase-matching angle θ.

Figure 2.7 visualized, how the phase-matching is achieved byangle-tuning of the non-linear crystal. For a negative uniaxial crystal, the refractive index of the extraordinary wave is smaller than the one of the ordinary wave, such that $\Delta n = n_e - n_0$ is negative, as seen from figure 2.7 (a).

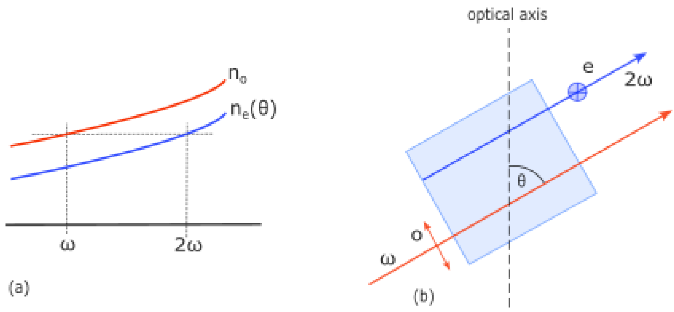

Figure 2.7.: (a) Refractive indices of negative uniaxial crystals, $n_e < n_0$. (b) Critical phase-matching is achieved byangle-tuning of the non-linear crystal.

Type I Critical Phase-Matching for Biaxial Crystals

For biaxial crystals, the calculation is more involved, since there are three principal refractive indices n_x, n_y and n_z, where in general $n_x < n_y < n_z$. The material is considered negative (or positive) biaxial if $n_z - n_y < n_y - n_x$ (or $n_z - n_y > n_y - n_x$). Furthermore, with two optical axes, it becomes impossible to define an ordinary- and an extraordinary ray.

Investigating it in more detail: Biaxial crystals have two phase matching angles θ_m and ϕ_m, where θ_m is the angle between the wave vector (direction of propagation of the light) and the z-axis (one optical axis of the crystal). And, ϕ_m is the angle between the wave vector projection on the xy-plane and the x-axis (second optical axis of the crystal). The phase-matching condition for biaxial crystals is given by equation 2.47 [27], [28]:

$$\frac{k_x^2}{n_i^{-2} - n_x^{-2}} + \frac{k_y^2}{n_i^{-2} - n_y^{-2}} + \frac{k_z^2}{n_i^{-2} - n_z^{-2}} = 0 \tag{2.47}$$

where

$$k_x = \sin^2\theta_m \cos^2\phi_m \tag{2.48}$$

$$k_y = \sin^2\theta_m \sin^2\phi_m \tag{2.49}$$

$$k_z = \cos^2\theta_m. \tag{2.50}$$

n_x, n_y, n_z are the three principal refractive indices. To find the phase matching angles θ_m and ϕ_m one needs to solve the set of equations given in 2.47 for $i \in [1, 2, 3]$.

The phase matching condition and the value of the second-order nonlinear coefficient χ_{eff} must be considered at the same time. In this advanced case, phase matching alone

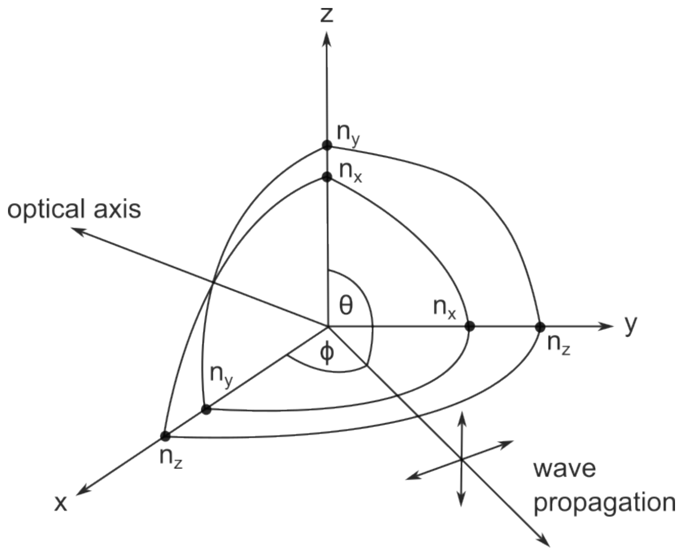

Figure 2.8.: Qualitative behavior of the refractive indices for a negative biaxial crystal, in the special case of $\theta = 90°$ a wave-vector traveling in the xy-plane. Figure adapted from [15].

might not automatically lead to a maximum value of χ_{eff}. While the value of θ_m is evaluated by the phase matching condition ($\theta_m = \theta_{\text{pm}}$), the value of ϕ_m is chosen such that χ_{eff} is optimized. What makes the problem more difficult is that both angles θ_m and ϕ_m depend on each other, and there are different possible angel configurations, as indicated by the index m. The values for θ_m and ϕ_m are determined by the manufacturer to be suitable for the desired application.

Hobden [29] found 13 phase-matching solutions for biaxial crystals. The complete list of all conditions would exceed this thesis. In general, it involves finding a solution to equation 2.47 for a set of θ_m and ϕ_m. There have been attempts to find a more direct solution to equation 2.47, for instance in the article by Yao and Fahlen [30].

Luckily, the biaxial LBO used in this thesis is a special case. The manufacturer Eksma [9] has chosen the angles such that $\theta = 90°$. In short, this means that the biaxial crystal effectively behaves like a uniaxial crystal, if the input beam travels in the correct plane. The index ellipsoid for this the special case of $\theta = 90°$ is illustrated in figure 2.8.

If a vertically polarized ray is propagating in the xy-plane, it will always see the refractive index n_z, regardless of the angle ϕ, which is enclosed with the x-axis. Whereas, p-polarized light (in the xy-plane), will see an increasing refractive index with increasing ϕ from n_x going to n_y. Under those constraints, a negative biaxial crystal behaves exactly like a negative uniaxial crystal, which again allows to define an ordinary and extraordinary ray, where $n_o = n_z$.

This can also be seen mathematically: With $\sin(90°) = 1$, equation 2.47 simplifies to the equation for uniaxial crystals 2.46, such that the second angle ϕ can simply be calculated by the formula for the phase-matching angle in uniaxial crystals [11]

$$\phi_{\text{pm}} = \cos^{-1}\sqrt{\frac{\left(\frac{1}{n_{y,e}}\right)^2 - \left(\frac{1}{n_{z,o}}\right)^2}{\left(\frac{1}{n_{x,e}}\right)^2 - \left(\frac{1}{n_{z,o}}\right)^2}}. \tag{2.51}$$

The phase-matching angles for the biaxial LBO-crystal are taken from the manufacturers specification sheet [9]:

$$\theta = 90° \tag{2.52}$$
$$\phi = 27.9° \tag{2.53}$$

A visualization of the phase-matching angles with respect to the coordinate system is given in figure 2.8.

2.4. Boyd-Kleinman-Theory

In 1968, Boyd and Kleinman published their theoretical analysis on the optimization of Second Harmonic Generation (SHG) using focused Gaussian beams in non-linear uniaxial crystals. Their concept applies to both negative and positive biaxial crystals because of symmetry reasons. The study examines the SHG output power with dependence on the ratio l_c/b_0, where l_c is the optical path length in the crystal and b_0 is the confocal parameter. Their analysis takes into account diffraction and double refraction.

2.4.1. General Concept

The concept is based on the following idea: A Gaussian beam is focused on a non-linear crystal, in which light with frequency ω interacts with the medium. Consequently, electromagnetic radiation is emitted with twice the frequency 2ω. Since the incoming fundamental light is ordinarily polarized and the second harmonic is extraordinarily polarized, the two beams will experience a walk-off and consequently a spatial separation by an angle ρ . Both the beam quality and the conversion efficiency decrease with increasing walk-off angle. Based on those assumptions, Boyd and Kleinman obtained the following relation between the fundamental input power P_ω and the second harmonic power $P_{2\omega}$:

$$P_{2\omega} = K P_\omega^2 l_c h(\xi, \sigma, B, \kappa, \mu) e^{-\alpha l_c} \tag{2.54}$$

where

$$K = \frac{16\pi^2 d_{\text{eff}}^2}{\epsilon_0 c \lambda^3 n_1 n_2}. \tag{2.55}$$

For better readability, K summarizes the effective non-linear coefficient d_{eff}, the electric susceptibility in vacuum ϵ_0 and the refractive indices n_1 and n_2 for the ordinary and extraordinary axes within the crystal. However, under phase-matching conditions, one can assume that $n_1 = n_2$.

Analyzing equation 2.54 further, the output power $P_{2\omega}$ depends on the crystal length l_c and the absorption coefficient α . The function $h(\xi, \sigma, B, \kappa, \mu)$ includes the optimizable parameters σ, μ and ξ, which represent phase mismatch 2.61, focal position 2.64 and focus strength 2.59, respectively. In addition, h depends on the parameter B 2.63, which takes into account double refraction and absorption κ

$$\kappa = \frac{\alpha b_0}{2} \tag{2.56}$$

with the absorption coefficient

$$\alpha = \alpha_1 + \alpha_2/2 \tag{2.57}$$

where α_1 and α_2 correspond to the fundamental and harmonic wave, respectively.

The Boyd-Kleinman double integral h is given by the expression

$$h(\xi, \sigma, B, \kappa, \mu) = \frac{1}{4\xi} \iint\limits_{-\xi(1-\mu)}^{\xi(1+\mu)} \frac{\exp\left[-\kappa(\tau + \tau') + i\sigma(\tau - \tau') - \frac{B^2(\tau-\tau')^2}{\xi}\right]}{(1 + i\tau)(1 - i\tau')} \, d\tau \, d\tau'. \tag{2.58}$$

All parameters in equation 2.58, will now be discussed in more detail.

The focus strength ξ is given as the ratio between the crystal length l_c and the confocal parameter $b_0 = 2z_0$, where z_0 is the Raleigh range, which takes into account the minimal waist size ω_0 and the wavelength $\lambda = \lambda_0/n$ in a medium with refractive index n.

$$\xi = \frac{l_c}{b_0} = \frac{l_c}{2z_0} \tag{2.59}$$

This results in an optimal crystal waist size for maximal conversion efficiency in the frequency doubling process:

$$w_0 = \sqrt{\frac{l_c \lambda}{2\pi\xi}} \tag{2.60}$$

The relation in equation 2.60 was derived by re-expressing equation 1.6 in terms of the Rayleigh range z_0 and inserting it into equation 2.59.

The phase mismatch between the fundamental and the harmonic wave is described by σ

$$\sigma = \frac{b_0}{2} \Delta k \tag{2.61}$$

where Δk is the wavevector difference, which is defined by the following expression using $\omega_2 = 2\omega_1$:

$$\Delta k = 2k_1 - k_2 = \frac{2\omega_1}{c}(n_1 - n_2) \tag{2.62}$$

The parameter B accounts for the double refraction angle ρ, which occurs since the fundamental and harmonic waves have ordinary and extraordinary polarizations, respectively.

$$B = \frac{\rho}{2}\sqrt{l_c k_1} \tag{2.63}$$

The focal parameter μ, is defined by the position of the focus in the crystal d_f. If the focus lies exactly in the center of the crystal $d_f = l_c/2$, then the focal parameter does not contribute to the calculations $\mu = 0$.

$$\mu = \frac{l_c - 2d_f}{l_c} \tag{2.64}$$

2.4.2. Simplification under ideal conditions

In the special case of no absorption $\kappa = 0$ and assuming that the focus position is exactly at the center of the crystal ($\mu = 0$), the Boyd-Kleinman integral reduces to:

$$h(\xi, \sigma, B) = \frac{1}{4\xi} \iint\limits_{-\xi}^{\xi} \frac{\exp\left[i\sigma(\tau - \tau') - \frac{B^2(\tau-\tau')^2}{\xi}\right]}{(1 + i\tau)(1 - i\tau')}\, d\tau\, d\tau' \tag{2.65}$$

Since the harmonic output power $P_{2\omega}$ is proportional to $h(\xi, \sigma, B)$, one wants to maximize h with regard to the parameters ξ and σ, which is often only possible by numerical calculations.[31]

2.4.3. Extended theory for elliptical beam shapes

To be precise, the Boyd-Kleinman theory is only valid for circular beam profiles. If Brewster-cut crystals are used, the beam experiences an expansion in the plane of incidence (tangential plane), which results in an elliptical beam shape. Bourzeix et al. have extended the BK-theory such that it accounts for the ellipticity of the beam shape [32].

$$P_{2\omega} = K P_{\omega}^2 l_c h(\xi, \sigma, B, \kappa, \mu) e^{-\alpha' l_c} \cdot \frac{\omega_{0,s}}{\omega_{0,t}} \tag{2.66}$$

This shows, that equation 2.54 only has to be extended by the ratio of the waist in sagittal $w_{0,s}$ and in tangential direction $w_{0,t}$. The non-linear coefficient can be extended likewise.

$$\gamma = \frac{P_{2\omega}}{P_{\omega}^2} = K l_c h(\xi, \sigma, B, \kappa, \mu) e^{-\alpha' l_c} \cdot \frac{w_{0,s}}{w_{0,t}} \tag{2.67}$$

2.4.4. Analytical approximation of the Boyd-Kleinman integral

Although, the assumptions in section 2.4.2 already offer a great simplification in the calculation of the BK-parameter, it still involves solving a two-dimensional integral and an additional optimization procedure regarding the wavevector mismatch Δk as defined in equation 2.61 [31]. With regard to the complexity, many efforts have been made to find a simplified and more straightforward approximation to the BK-integral. For instance, Chen and Chen [33] or J. R. Daniel et al. [34] have both proposed analytical functions, which give approximations to the gain function h and the strength of focus ξ. Both theories provide a direct relation between the total conversion efficiency on the walk-off and focusing parameters. In the following, I will focus on the former approximation of Chen and Chen [33]. In their publication, they propose the following analytical expression for the h-function:

$$h_{\text{mm}}(B) = \frac{1.068}{1 - 0.7\sqrt{B} + 1.62B} \tag{2.68}$$

The subscripts m and mm indicate, that one or two consecutive optimizations have been performed. The corresponding focusing parameter ξ_m, for which h reaches its maximum, is given by:

$$\xi_m(B) = \frac{2.84 + 1.39B^2}{1 + 0.1B + B^2} \tag{2.69}$$

With the following two expressions,

$$n(B) = \frac{1.91 + 1.83B}{1 + B} \tag{2.70}$$

and

$$\gamma(B) = \frac{\xi_m(0)^{n(0)}}{h_{\text{mm}}(0)} e^{-B} + 13\left(1 - e^{-B/3}\right) \tag{2.71}$$

one can approximate the Boyd-Kleinman integral 2.65 with regard to the walk-off parameter B and the focusing parameter ξ:

$$h_m(B, \xi) = \frac{h_{\text{mm}}(B)\gamma(B)\xi}{|\xi - \xi_m(B)|^{n(B)} + \gamma(B)\xi} \tag{2.72}$$

In order to get a better understanding of the BK-theory, the function $h(\sigma, \xi, B)$ will now be discussed in more detail, using the analytical model described above. Figure 2.9 plots the h(B, ξ)-function with respect to ξ for different values of B, respectively.

2.4.5. Evaluation for the BBO-Crystal

The B parameter has been calculated by equation 2.63, taking into account for the double-refraction angle $\rho = 55.9$ mrad for the BBO-crystal (section 3.4.3) with a length of $l_c = 10$ mm. The large walk-off angle ρ also results in a larger B-value, which consequently shrinks the maximally achievable value for the BK-function h_m.

$$B = 10.43 \tag{2.73}$$

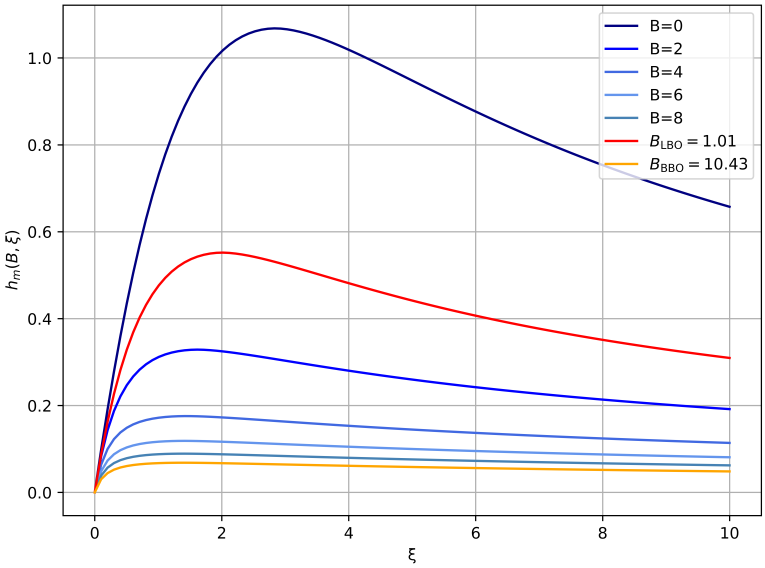

Figure 2.9.: $h_m(B, \xi)$-function for exemplary values of the double-refraction parameter B under optimal phase-matching conditions. The red and orange curves show the cases for the cavity/crystal parameters that are relevant for this thesis.

With the double-refraction parameter B, the optimal values for ξ and the h-function are obtained using equation 2.59 and 2.72, respectively.

$$\xi_{\text{opt}} = 1.39 \tag{2.74}$$

$$h_{\text{opt}} = 0.07 \tag{2.75}$$

As mentioned above, the large walk-off angle, shrinks the maximum value of h and consequently reduces the frequency conversion efficiency. From the result of the focusing strength ξ_{opt}, the optimal waist size w_0^{opt} at the center of the crystal can be calculated by equation 2.60.

$$\omega_0^{\text{opt}} = 22.70\ \mu m \tag{2.76}$$

2.4.6. Extension of the BK-theory for biaxial crystals

The initial investigation by Boyd and Kleinman [31] on the optimal beam parameters for maximum frequency conversion in non-linear media, was done for uniaxial crystals. For biaxial crystals, the concept becomes more complex, since there are three crystal axes with different refractive indices, which offer more configurations. Extensions to the original BK-theory have been proposed by Kerkoc et al. [35] to include biaxial crystals. Their investigation showed no difference in the calculation for uni- and biaxial crystals. However, their analyses referred to a specific experimental configuration and crystal material. A more comprehensive study was done by Li et al. [36]. The Boyd-Kleinman function $h(\xi, \sigma, B, \kappa, \mu)$ given in equation 2.72 stays the same, with the subtle extension of the double refraction parameter, $B = \sqrt{B_1^2 + B_2^2}$. For biaxial crystals the B-parameter consists of two terms B_1 and B_2, because of the two extraordinary axes. For uniaxial crystals this simplifies to $B = B_1 = B_2$. The calculation for the $B_{1/2}$-value is done by equation 2.77 and 2.78:

$$B_1 = \frac{\rho_\omega}{2}\sqrt{l_c k_1} \tag{2.77}$$

$$B_2 = \frac{\rho_{2\omega}}{2}\sqrt{l_c k_1} \tag{2.78}$$

2.4.7. Evaluation for the LBO-Crystal

For the double-refraction angel $\rho = 7$ mrad and a length of $l_c = 12$ mm, the following B-value was calculated:

$$B = 1.01 \tag{2.79}$$

This yields the following maximum value of the BK-function h_{opt} at the optimal focusing parameter ξ_{opt}, which is obtained for a crystal waist size of w_0^{opt}.

$$h_{\mathrm{opt}} = 0.55 \tag{2.80}$$

$$\xi_{\mathrm{opt}} = 2.00 \tag{2.81}$$

$$w_0^{\mathrm{opt}} = 29.30\ \mu m \tag{2.82}$$

Since the LBO crstal has a smaller walk-off angle than the BBO, the maximum value for h is larger by a factor of 10, which results in a higher frequency conversion efficiency in the IR-VIS cavity. As seen from figure 2.9, h reaches its maximum for a focusing strength given by 2.81, which is achieved when the waist in the crystal is focused to a size of $w_0^{\mathrm{opt}} = 29.30\ \mu m$.

3. Experiemental Implementation

This section describes the overall setup to achieve laser light in the deep UV region: Starting with the tunable Ti:Sa laser and the origin of the very first photon, followed by the experimental implementation of two external doubling stages to achieve laser light at a wavelength of 225 nm.

After an overview of the laser system , each cavity will be discussed in detail: Geometry, mode-matching and frequency conversion, Python-based simulations of the waist evolution, using the ABCD-matrix formalism and Gaussian ray propagation help to get a better understanding of the beam and as how the different optical elements influence its shape.

For each cavity, two simulations have been done: One covering the waist evolution outside of the resonators during mode-matching - and the other one simulating the propagation within the resonators, where the horizontal and vertical axes were treated independently.

To complete the understanding, the length stabilization technique is discussed, which also includes a short introduction to the locking electronics. Further an active beam stabilization system is described, which stabilizes the pointing of the Ti:Sa laser.

3.1. Fundamental: Titanium Sapphire Laser

The two external frequency doubling stages are pumped by a tunable Matisse CS laser from Sirah Lasertechnik [37]. It is an actively stabilized Titanium Sapphire (Ti:Sa). It is fully sealed and allows a hands-free operation by an Electronic Laser Self Alignment (ELSA) system. Although the Ti:Sa offers a wide tuning range over a wavelength span of $700 - 1000$ nm, it is constantly operated at 902 nm. At this wavelength, a maximum output power of roughly 5.4 W can be achieved, when it is pumped with 25 W 3.1a. The Matisse provides a narrow linewidth and emits horizontally polarized light with a divergence angle of < 2 mrad. The spatial mode profile is a TEM_{00}-mode with a beam diameter of roughly 1.4 mm at the Matisse output port. The waist position was experimentally determined by a beam profiler.

The curve fit based on equation 1.5

$$w(z) = w_0\sqrt{1 + \left(\frac{z - z_0}{z_R}\right)^2} \tag{3.1}$$

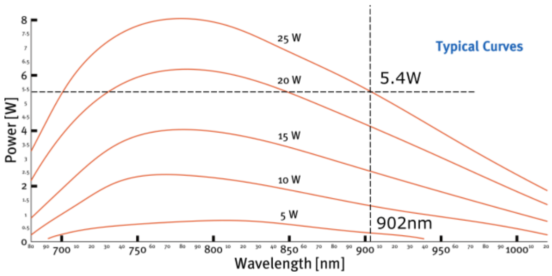

(a) Matisse laser power depending on the pumping powers and the wavelength it is operated at. Figure adapted from [37].

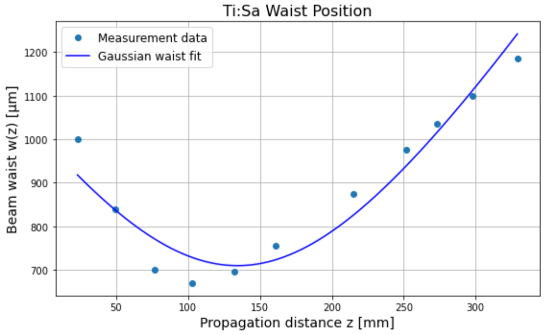

(b) Waist size and position of the Ti:Sa laser with respect to the output port.

Figure 3.1.: Ti:Sa output power, waist size and location.

gave the following results for the minimum waist size w_0 its distance from the Ti:Sa laser output:

$$w_0 = (709 \pm 28)\ \mu\text{m} \tag{3.2}$$
$$z_0 = (134.3 \pm 7.6)\ \text{mm} \tag{3.3}$$

3.1.1. Ti:Sa-Setup and Working Principle

The gain medium, is a titanium-doped sapphire crystal, is pumped by 'Millenia eV' from Spectra-Physics. It is a diode-pumped solid state (DPSS) laser with powers up to 25W at a wavelength of 532 nm. It provides a TEM$_{00}$ beam profile with high quality of $M^2 < 1.1$ and high power stability $\Delta P/P < 0.04$ % [38].

A brief description on the working principle of the Millenia laser is given here: A gain medium, which is usually a neodymium-doped yttrium aluminum garnet (Nd:YAG) emits radiation at 1064 nm, when it is pumped with a suitable source. This pump source is a diode laser, in which the recombination of holes and electrons leads to the emission of laser light. The 1064 nm-radiation from the Nd:YAG laser is then frequency-doubled to 532nm, which is the pumping source of the Ti:Sa laser.

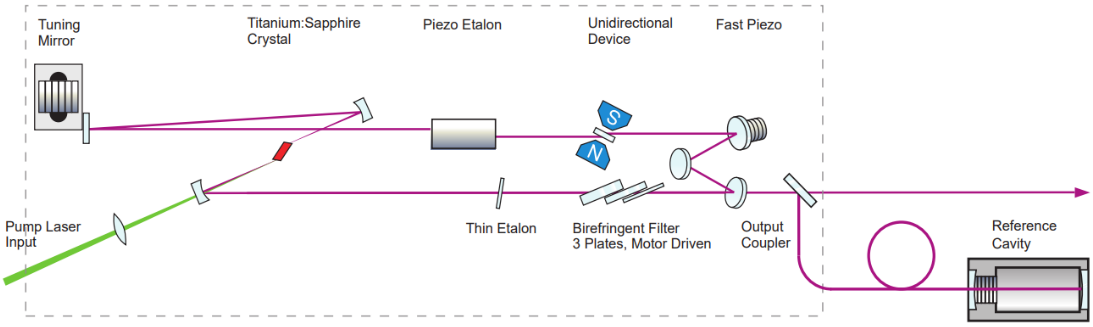

Figure 3.2.: Setup of the Ti:Sa system, which provides the fundamental laser light for the two external frequency-doubling stages. A titanium-doped sapphire crystal is pumped with 532 nm. The output frequency and linewidth of the Ti:Sa (902 nm) is determined by several frequency-selective elements.

Figure 3.2 visualizes the setup of the the Ti:Sa laser: The two spherical mirrors provide a feedback loop for the gain medium, such that electromagnetic fields with well-known properties will be emitted. Several frequency-selective elements are inserted in the resonator to achieve single-mode operation:

1. The **thin etalon** functions as a bandpass filter, which only allows a certain frequency range to pass. It can be tilted by a stepper-motor driven mount to provide tunability.
2. The **birefringent filter** rotates distinct wavelengths differently, such that the ones minimal losses will be enhanced in the resonator, whereas the others will be suppressed.
3. Through the **output coupler** a part of the laser light is emitted, whereas the rest is reflected and keeps circulating inside the cavity.
4. The **fast piezo** compensates for fast acoustic perturbations and thereby reduces the laser bandwidth.
5. The **Tuning Mirror** is also called **Slow Piezo** since it counteracts slow drifts of the laser to keep the fast piezo in the center of its moving range.
6. Since the Matisse laser could support two counter-propagating modes, a **unidirectional device** is used to only allow one direction of propagation.
7. The birefringent filter, the thin etalon and the output coupler define a spectral range of modes, which can be supported by the Ti:Sa laser. The **piezo etalon** is then used to select a single longitudinal mode.
8. An external **reference cavity** acts as a frequency reference for the stabilization of the Matisse laser.

3.1.2. Periscope

Since the exit of the Ti:Sa laser is above the plane of the cavities, it is necessary to guide the beam down using a periscope. All mirrors of the periscope must be parallel and the beam must be reflected at a 45° angle, such that its polarization is conserved. Behind the periscope, an active beam stabilization system is installed.

3.1.3. Active Beam Stabilization

The beam-pointing of the Ti:Sa laser might change due to temperature fluctuations and thermal expansion, changes in the humidity levels or mechanical noise. This required a daily re-alignment of the beam into the first cavity, which also influences the coupling into the second doubling stage. The beam-pointing instabilities could be resolved, by installing the active stabilization system Aligna by TEM Messtechnik [17]. It is implemented right after the periscope, to correct the instabilities as early as possible to avoid error accumulation and astigmatic effects later on in the beam path.

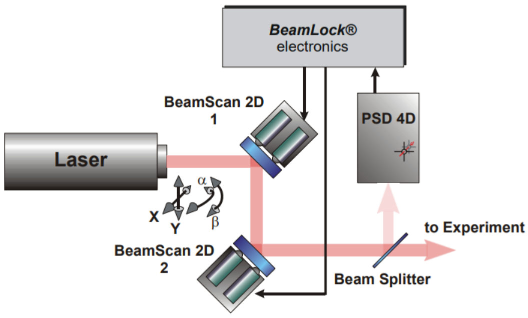

Figure 3.3.: The setup of the Aligna beam stabilization system comprises two motorized piezo-driven mirrors, a 4D position detector and the control unit. Figure taken from [16].

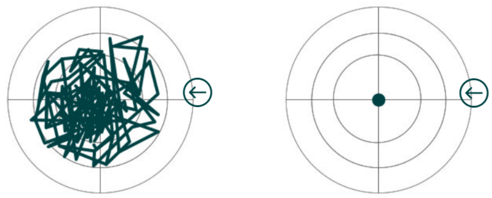

Figure 3.4.: Visualization of the active beam pointing stabilization provided by the Aligna system. Figure taken from [17].

Figure 3.3 shows the implementation of the Aligna system for pointing stabilization. The setup consists of two motorized and piezo-based actuators, a position-sensitive detector (PSD) and the control electronics. The 4D detector measures: two translational degrees of freedom X and Y and two angles α and β. The laser beam is then fully defined by those four values. Any deviations of the laser axis from the reference axis, will be compensated by the Aligna electronics. A feedback is then sent to the motorized steering mirrors, to compensate for the drift. Before using the stabilization system, it has to be trained to know the preferred reference axis. This data is converted into a (4×4) cross-link matrix, which contains all the relevant information of the setup, including the relative mirror arrangement and their separation as well as the distance to the detector and properties of the mirror mounts. After training, it works fully automated. A visualization of the effect of the active beam stabilization is shown in figure 3.4. [16]

3.2. Frequency Doubling Setup

Figure 3.5 gives an overview of the overall experimental setup. The Ti:Sa laser is operated at a wavelength of 902 nm. Its light is then frequency doubled twice, using two external bow-tie enhancement cavities. Within the resonators the fundamental power is built up and the light is then frequency doubled by a nonlinear crystal using the principle of second-harmonic generation (SHG).

abbreviation	description
Ti:Sa	Titanium Sapphire pumping laser
AM_n	Aligna mirror, $n \in [1, 2]$
M_n	guiding mirror, $n \in [1, 12]$
WD_n	flat optical window $n \in [1, 2]$
$\lambda/2_n$	half-wave plate, $n \in [1, 5]$
$\lambda/4_n$	quarter-wave plate ($n \in [1, 2]$)
L_n	lens, $n \in [1, 9]$
SMP_n	beam sampler $n \in [1, 2]$
ND 40/10	neutral density filter (optical density: 4.0/1.0)
PH	pinhole
BSC	beam-splitter cube
PM_i	power-meter position, $i \in [902_{nm}, 451_{nm}, 225_{nm}]$
W_n	Wollaston-prism, $n \in [1, 2]$
DC_n	dichroic mirror $n \in [1, 2]$
PID	proportional–integral–derivative locking electronics
LBO	Lithium triborate crystal (LiB_5O_5)
BBO	Barium borate crystal (BaB_2O_4)
PSD 4D	position sensitive detector in four degrees of freedom

Table 3.1.: Abbreviations and the corresponding description of every component, which is visualized in the setup sketch 3.5.

Firstly, light is converted from the infrared region (902 nm) down to the visible range (451 nm) using a symmetric cavity and a spherically shaped Gaussian beam. This light is further doubled in a second asymmetric cavity using an elliptically shaped beam, to achieve laser light in the deep UV region (225 nm). Both cavities, including the locking electronics, were purchased from the company Agile Optic [39]. The length stabilization in both cavities is based on the Hänsch-Couillaud locking mechanism. In figure 3.5 the individual doubling stages including their locking setups are indicated by the blue and violet background colors. Throughout the text, the individual cavities will often be referred to as the IR-VIS and VIS-UV cavity. The naming convention indicates the wavelength ranges which are converted in the resonators. All individual components of setup 3.5 are listed in table 3.1.

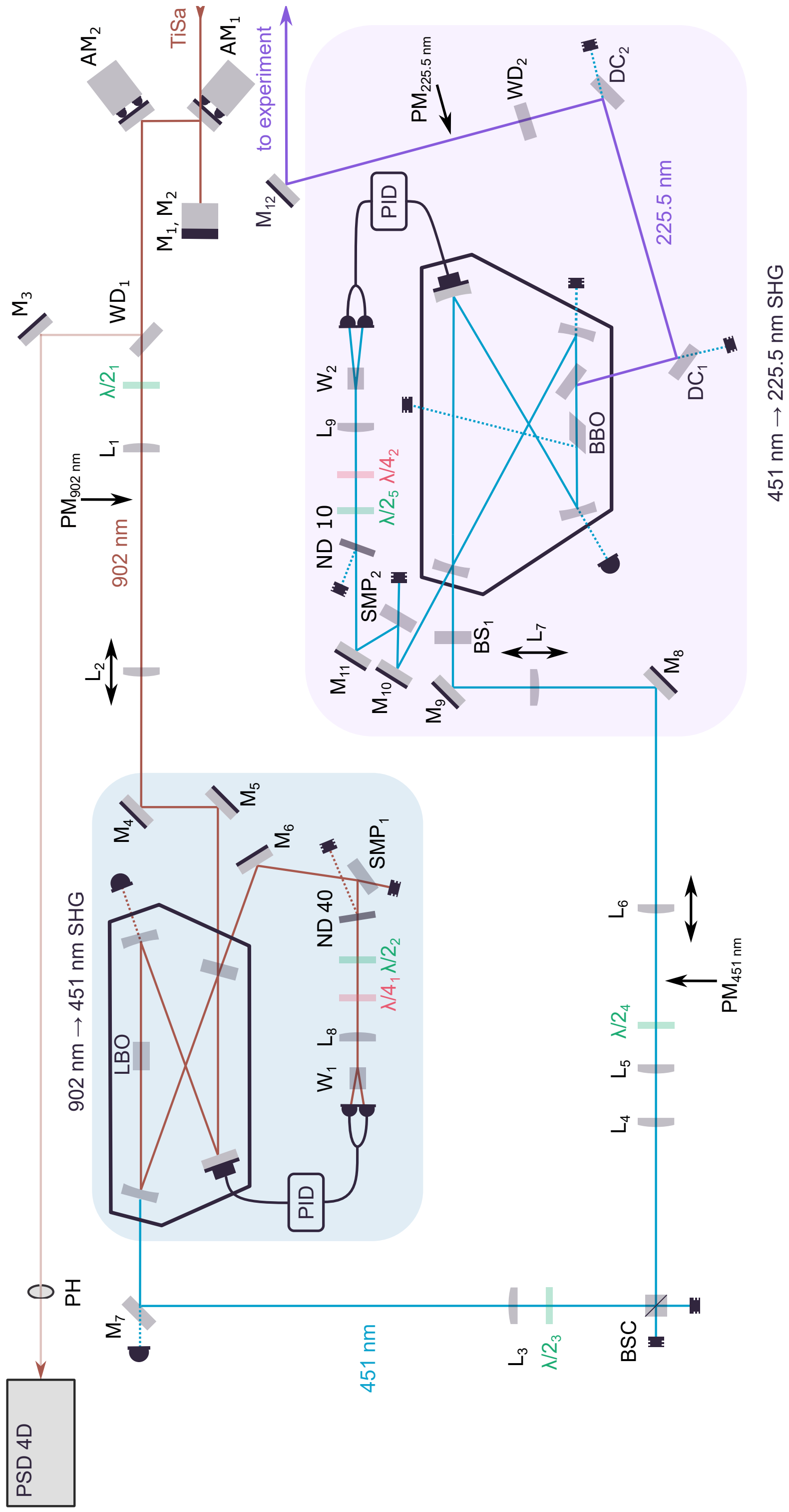

Figure 3.5.: Overview of the experimental setup, including the initial Ti:Sa laser, the active beam stabilization system, the two consecutive SHG-cavities with their Hänsch-Couillaud locking mechanism each, as well as all guiding mirrors and lenses for the mode-matching. The abbreviations are summarized in table 3.1.

3.3. IR-VIS Cavity

In this section, the first doubling stage is described. Starting with the mode-matching of the Titanium Sapphire laser to the cavity eigenmode. Then focusing on the geometry of the resonator, the evolution of the waist inside the cavity and the crystal properties.

3.3.1. Mode Matching

In order to shape the output of the Ti:Sa laser to match the resonators spatial modes at the incoupling position, a telescope consisting of two plano-convex lenses is used, as depicted in figure 1.5. Both lenses L_1 and L_2 are mounted on translation stages, in order to systematically optimize their position and achieve the best mode matching. Their respective focal lengths are $f_1 = 150$ mm and $f_2 = 100$ mm. The flat sides of the lenses are facing each other, as visualized in figure 1.5. The orientation of the lenses is chosen such that spherical aberrations are reduced. Less optical distortion is introduced, when the curved surface faces the collimated beam from the Ti:Sa. The second lens is oriented such the the flat side faces the focal point.

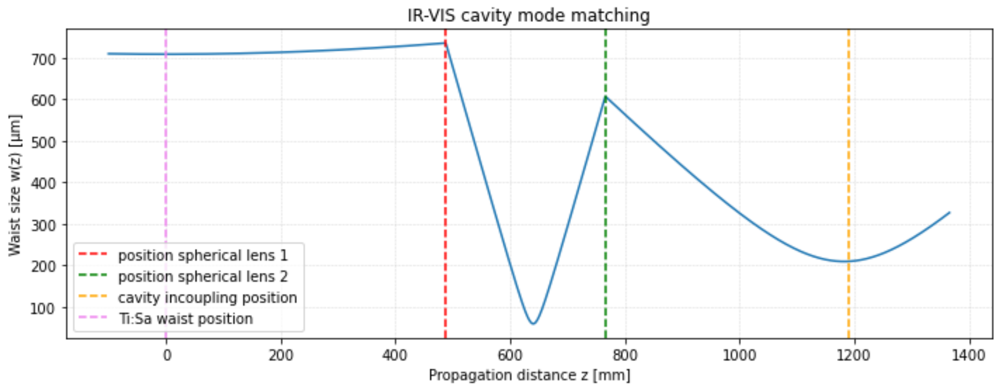

Figure 3.6.: The simulation shows, how the output waist of the Ti:Sa laser is mode matched to the eigenmodes of the IR-VIS cavity using two plano-convex lenses L_1 and L_2 with focal lengths of $f_1 = 150$ mm and $f_2 = 100$ mm, respectively.

Figure 3.6 visualized the waist evolution, starting from the position of the Ti:Sa laser and then using ABCD-matrix formalism to simulate the beam propagation through the lenses L_1 and L_2 until the incoupling position of the first resonator. Effects of the incoupling mirror of the IR-VIS cavity could were neglected, since it is planar.

Finding the right positions for the lenses is an iterative process. Figure 3.7a and 3.7b show the final measurements of the beam waist in the horizontal and vertical direction at the incoupling position. For the measurements, the cavity was removed temporarily, to make space for the beamprofiler. A Gaussian waist fit according to equation 3.1 has been put over the measurement data, which shows a good agreement between the measurements and the theoretical predictions.

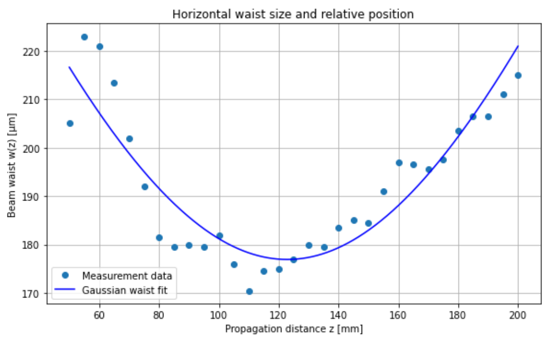

(a) Horizontal beam waist measurements.

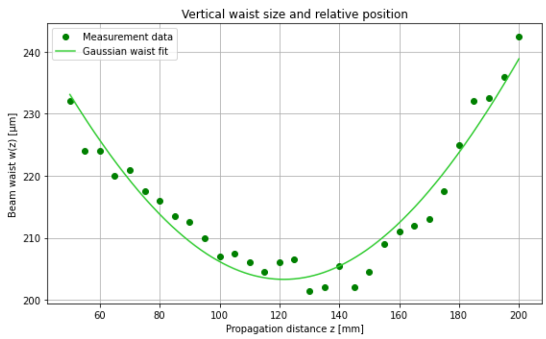

(b) Vertical beam waist measurements.

Figure 3.7.: Measurement data of the waist sizes and the relative positions of the minima, to optimize the mode-matching of the IR-VIS cavity. A Gaussian waist fit according to equation 1.5 has been put over the data points.

From the fit-parameters, the following waist sizes have been obtained

$$
\begin{aligned}
w_h &= 177\ \mu\text{m} && (3.4)\\
w_{h,target} &= 186\ \mu\text{m} && (3.5)\\
w_v &= 203\ \mu\text{m} && (3.6)\\
w_{v,target} &= 205\ \mu\text{m} && (3.7)\\
& && (3.8)
\end{aligned}
$$

which are located roughly at the same relative positions

$$
\begin{aligned}
z_{0,h} &= (122.8 \pm 1.8)\ \text{mm} && (3.9)\\
z_{0,v} &= 121\ \text{mm} && (3.10)\\
z_{0,target} &= 122\ \text{mm}. && (3.11)
\end{aligned}
$$

3.3.2. Geometry of the Resonator

The first doubling stage comprises a symmetric bow-tie shaped cavity. The light is coupled into the resonator by a planar incoupling mirror M_1 with reflectivity $R_1 = 98.4\%$. It is then reflected by another flat mirror M_2, which is mounted on a piezoelectric actuator for length stabilization. Right between M_1 and M_2, the resonator waist reaches a minimum. In order to achieve the best mode-matching an ideal waist of 205 μm in the sagittal and 186 μm in the tangential plane is aimed for. Two spherical mirrors M_3 and M_4 with ROC = 50 mm then focus the beam down to a circular waist of roughly 25 μm.

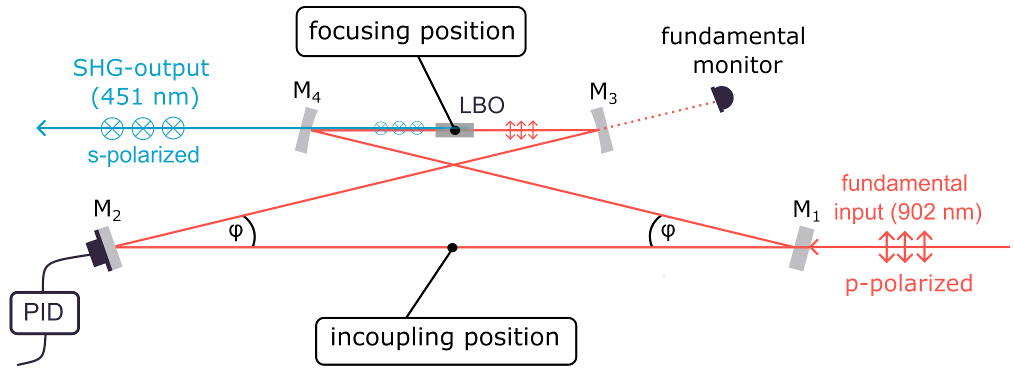

Figure 3.8.: Symmetrical bow-tie cavity for frequency doubling light from 902 nm to 451 nm. The ordinarily polarized input field is mode matched to the cavity eigenmodes. The incoupling mirror M_1 and the Piezo mirror M_2 are planar, whereas the mirrors M_3 and M_4 are spherical with a radius of curvature of 50 mm to focus the beam into the center of the LBO crystal. The frequency doubled, extraordinary polarized light is coupled out of the cavity through mirror M_4.

The LBO-crystal is located right between the curved mirrors M_3 and M_4, where the beam waist reaches its minimum for efficient frequency conversion. A small amount of light is transmitted through M_3, serving as a reference signal of the fundamental light, which is necessary when aligning the cavity for the first time. The signal is measured by a simple photodiode. Except for the incoupling mirror (M_1), all other intra-cavity mirrors (M_2, M_3, M_4) are highly reflective for the fundamental light and have a large transmittance for the second-harmonic light. The exact specifications for the front sides of the mirrors are: $R(904 \text{ nm}) > 99.9$ %, $R(452 \text{ nm}) < 1$ %. On the rear sides, their reflectivity is low for both the fundamental and the harmonic light: $R(904 \text{ nm and } 452 \text{ nm}) < 1$ %. They are officially specified for the wavelength ranges $(450 - 460)$ nm and $(900 - 920)$ nm.

3.3.3. Waist Evolution inside the Cavity

For the symmetric IR-VIS cavity the matrix, which describes the round-trip propagation through the resonator, is given by multiplication of the single components in reverse order. The individual ABCD-matrices can be looked up in Appendix A.1. The start and end point are chosen to be at the incoupling position of the cavity. Since the curved, spherical mirrors are tilted by an angle θ with respect to the direction of the incoming beam, their ABCD-matrices for the tangential and sagittal plane differ by the effective radii of curvature, with $R_{eff,t} = R \cdot cos(\theta)$ and $R_{eff,s} = \frac{R}{cos(\theta)}$.

$$
\begin{aligned}
M &= \begin{pmatrix} A & B \\ C & D \end{pmatrix} = \\
&= \begin{pmatrix} 1 & \frac{l_1}{n_{air}} \\ 0 & 1 \end{pmatrix} \begin{pmatrix} 1 & 0 \\ -\frac{2}{R_{\text{eff}}} & 1 \end{pmatrix} \begin{pmatrix} 1 & \frac{l_2}{n_{air}} \\ 0 & 1 \end{pmatrix} \begin{pmatrix} n_c & 0 \\ 0 & \frac{1}{n_c} \end{pmatrix} \begin{pmatrix} 1 & \frac{l_c}{n_c} \\ 0 & 1 \end{pmatrix} \begin{pmatrix} \frac{1}{n_c} & 0 \\ 0 & n_c \end{pmatrix} \begin{pmatrix} 1 & \frac{l_2}{n_{air}} \\ 0 & 1 \end{pmatrix} \\
&\times \begin{pmatrix} 1 & 0 \\ -\frac{2}{R_{\text{eff}}} & 1 \end{pmatrix} \begin{pmatrix} 1 & \frac{l_1}{n_{air}} \\ 0 & 1 \end{pmatrix}
\end{aligned}
$$

Here, l_1 is the length from the incoupling position to the first spherical mirror and l_2 is the distance from the spherical mirror to the crystal surface. The crystal is rectangular cut and has a refractive index n_c and a length of l_c.

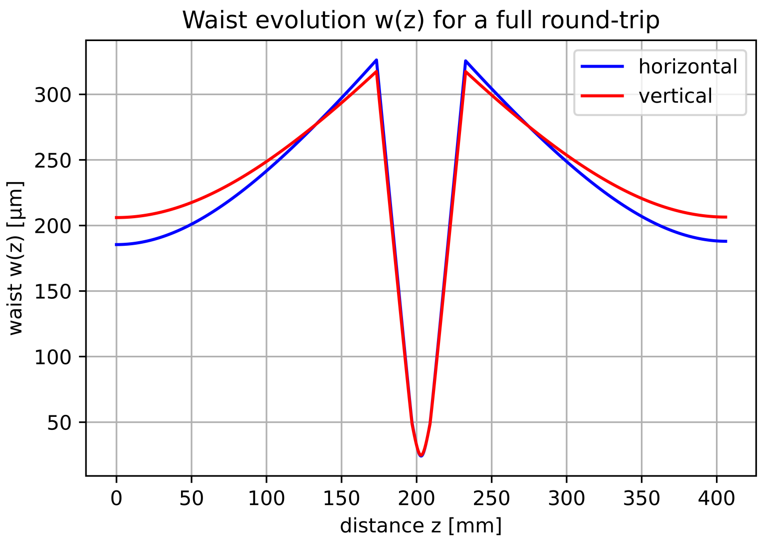

[H]

Figure 3.9.: The waist evolution during a full round-trip through the IR-VIS cavity. The plot starts and ends at the incoupling position. The waist size maximizes at the two spherical mirrors M_3 and M_4, and is focused to a waist size in the center of the crystal of roughly 25 μm in both the horizontal the vertical plane.

The waist evolution inside the IR-VIS cavity has been simulated in Python using the above described ABCD-matrix formalism for Gaussian ray propagation. The program calculates the q-parameter at the incoupling position according to equation 1.8. At the incoupling position it is assumed that the radius of curvature of the beam is infinite such that $1/R(z) \to 0$ for $R(z) \to \infty$. Based on this initial value, the q-parameter then evolves throughout the cavity, according to the above ABCD-matrix, and using the relation between q_2 and q_1 according to 1.11. Since the complex beam parameter contains all the relevant information about the Gaussian beam, one can therefore calculate the waist size at every position within the cavity by re-expressing equation 1.8. Figure 3.9 shows, that the waist has two minima inside the cavity: One at the incoupling position (between M_1 and M_2) and another, strongly focused minimum, at the center of the crystal (between the two spherical mirrors M_3 and M_4). It can also be seen, that the beam maintains a circular shape throughout the resonator.

3.3.4. Lithium triborate crystal (LiB_5O_5)

For the first doubling stage a $(3\times3\times12)$ mm^3 lithium triborate (LBO) crystal from Eksma Optics [9] has been chosen. It is right-angle cut and has anti-reflection (AR) coatings on the ends, which are perpendicular to the light's propagation axis. Throughout the whole operation of the setup, it never showed signs of degradation or the need for re-coating. The crystal is constantly heated to 45°C by the temperature controller TEC-1091 by Meerstetter Engeneering [40].

The most important specifications of the LBO-crystal are summarized in table 3.2 [9].

	Lithium triborate crystal (LiB_5O_5)
optical symmetry	negative biaxial
phase-matching	type I ($o + o \to$ e), critical
phase-matching angles	$\theta = 90°$, $\phi = 27.9°$
temperature	45°
nonlinear coefficient	d_{32} = -(0.98 ± 0.09) pm/V
effective nonlinearity	$d_{ooe} = d_{32}\cos\phi = -(0.866 \pm 0.080)$ pm/V
walk-off angle	7 mrad (Type I SHG 1064 nm)
AR coating	$R < 0.1\%$ for 840 nm, $R < 0.5\%$ for 420 nm
dimensions	$(3 \times 3 \times 12)^3$ mm
shap	right-angle cut

Table 3.2.: LBO crystal parameters according to the specification sheet provided by Eksma [9]

For frequency doubling light from the infrared wavelength range down to the visible range, the LBO-crystal is a frequently used crystal, for instance by [41], [42], [43] or [1].

3.4. VIS-UV Cavity

3.4.1. Geometry of the Resonator

In order to double the frequency a second time into the deep UV-range of 225 nm, an asymmetric, bow-tie shaped enhancement cavity by Agile Optic [39] is used. Its geometry is visualized in figure 3.10.

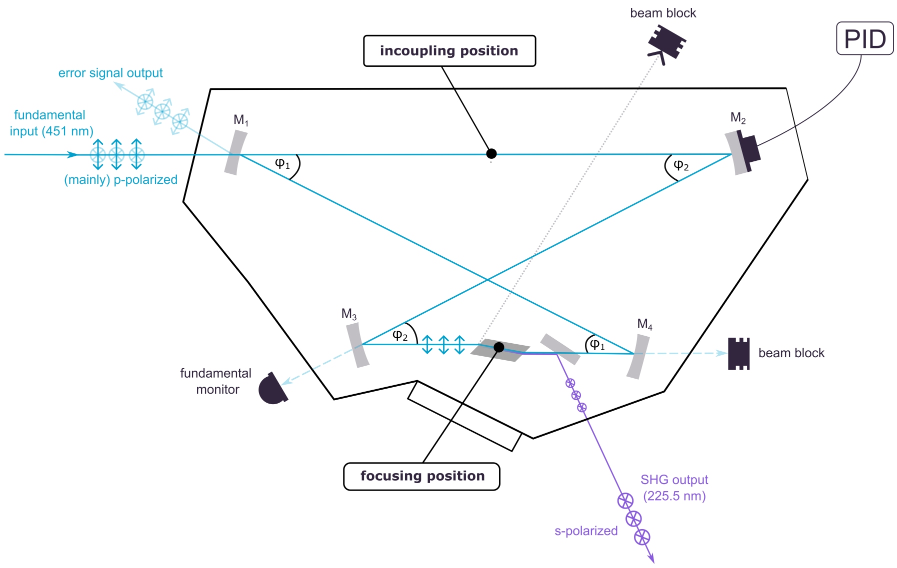

Figure 3.10.: An asymmetric bow-tie cavity is used to frequency double light from 451 nm to 225 nm. The input field has ordinary polarization. It is coupled into the cavity by the spherical mirror M_1 and reflected by the spherical Piezo mirror M_2 with the same radius of curvature. The cylindrical mirrors M_3 and M_4 focus the beam in the vertical axis. The frequency-doubled light (with extraordinary polarization) is extracted from the cavity by an outcoupling mirror.

The slightly asymmetric shape is necessary due to the Brewster-cut shape of the frequency doubling crystal. Ordinarily polarized light is coupled into the resonator by an incoupling mirror with a reflectivity of $R = 98.1\%$. In contrary to the first cavity, the second resonator supports elliptically shaped Gaussian modes. At the incoupling position, the waist sizes in the tangential and sagittal plane are roughly 143 μm and 267 μm, respectively. The incoupling mirror (M_1) and the mirror, on a piezo-electric actuator for length stabilization (M_2), are spherically shaped with a radius of curvature of $\mathrm{ROC} = 1500$ mm. The beam is then guided towards two cylindrically shaped mirrors M_3 and M_4, which have a smaller radius of curvature of $\mathrm{ROC} = 150$ mm. Those mirrors are aligned vertically, such that the beam is only focused in the horizontal direction. The vertical axis of the beam is left unchanged, since it effectively only sees two planar mirrors.The elliptical beam profile has the advantage that crystal degradation effects are reduced, since the larger beam area distributes the intensity more, while still providing good frequency conversion in the horizontal axis. The beam has a larger waist size in the phase-matching plane (vertical axis) than the walk-off, to reduce its effects. When the fundamental light travels through the crystal, it experiences a transverse shift due to Snell's law and second harmonic light is extracted from the cavity by a dichroic outcoupling mirror.

An in depth description on the polarization, refraction and frequency conversion in the BBO crystal is given in section 3.4.3. For a better understanding, the beam path is visualized in figure 3.15. Right after the cavity, two dichroic mirrors clean the UV-beam from the fundamental wavelength. To ensure a good performance, it is crucial to hit the two dichroic mirrors at an exact angle of 45°.

Mode Matching

Mode matching is slightly more complicated because of the elliptical beam shape. At the incoupling position, the beam waist should be 143 μm and 267 μm in the tangential and sagittal plane, respectively. This corresponds to an ellipticity of $\epsilon = 0.54$.

Since the waist in the first cavity is small, the beam has a big divergence angle. Therefore, a spherical lens L_3 with focal length $f_3 = 300$mm is needed to reduce the waist size in both planes. For the mode-matching to the second cavity, four cylindrical lenses $(L_4 - L_7)$ are used, two for each plane, respectively. The vertical waist is shaped by L_5 and L_7, with focal lengths of $f_5 = 200$ mm and $f_7 = 75$ mm, which is shown in figure 3.11.

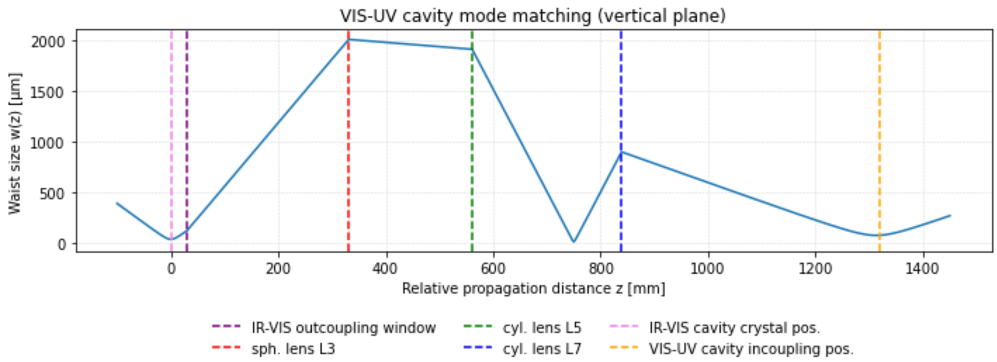

Figure 3.11.: Python based simulation of the (vertical) waist evolution through the telescope for the mode-matching to the VIS-UV cavity using one spherical lens (L_3) and two cylindrical lenses (L_5, L_7). The plot starts at the crystal position of the VIS-UV cavity and ends at the incoupling position of the IR-VIS resonator.

Figure 3.12 shows a simulation of the horizontal waist size through the telescope, consisting of the cylindrical lenses L_4 and L_6 with focal lengths of $f_4 = 300$ mm and $f_6 = 50$ mm. The last lenses (L_6 and L_7) of each telescope are mounted on translational stages, since their position has the most significant influence on the waist size/position inside the resonator.

What is interesting to see from the figures 3.11 and 3.12 are the different focus positions of the vertical and horizontal axes through the telescope. In both simulations, the incoupling mirror of the VIS-UV cavity has been neglected due to its large radius of curvature of ROC = 1500 mm.

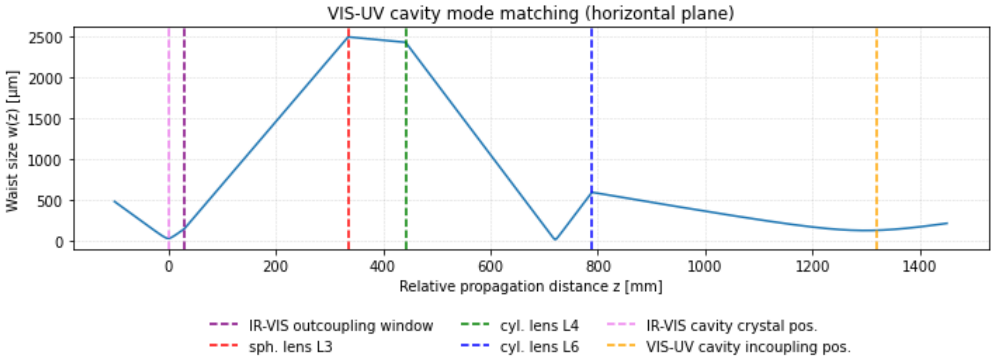

Figure 3.12.: An Python based simulation of the (horizontal) mode-matching of the beam using the same spherical lens L_3 and two cylindrical lenses L_4, L_6. The plot starts again at the crystal position of the VIS-UV cavity and ends at the incoupling position of the IR-VIS resonator.

The implementation of the telescope for the VIS-UV cavity was done iteratively, by measuring the size and location of the beam waist, after placing each of the four lenses (L_4, L_5, L_6, L_7). The final measurements are shown in figure 3.13a and 3.13b.

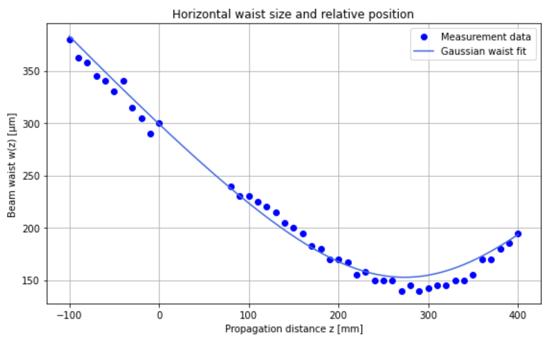

(a) Horizontal waist size and relative position.

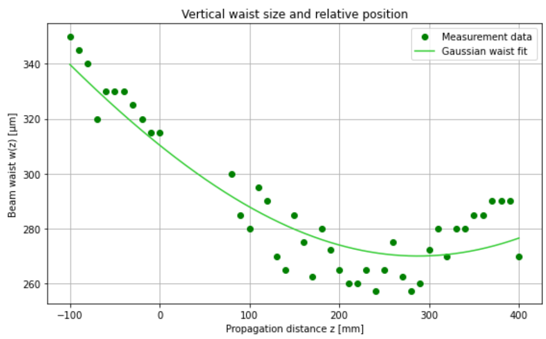

(b) Vertical waist size and relative position.

Figure 3.13.: Waist after final placement of all lenses ($L_4 - L_7$) of the telescope. A Gaussian waist fit according to equation 3.1 was fitted to the data points.

$$
\begin{aligned}
w_h &= 153\ \mu\text{m} && (3.12)\\
w_{h,target} &= 143\ \mu\text{m} && (3.13)\\
w_v &= 270\ \mu\text{m} && (3.14)\\
w_{v,target} &= 267\ \mu\text{m} && (3.15)\\
& && (3.16)
\end{aligned}
$$

andthe relative positions of the minima

$$
\begin{aligned}
z_{0,h} &= 277\ \text{mm} && (3.17)\\
z_{0,v} &= 288\ \text{mm} && (3.18)\\
z_{0,target} &= 270\ \text{mm}. && (3.19)
\end{aligned}
$$

The setup of the two folded telescope was challenging, since the rotation of the cylindrical lenses is sensitive to misalignment. Furthermore, the lens positions were optimized to high laser powers at 451 nm, since their effective radius of curvature changes with intensity.

3.4.2. Waist inside the VIS-UV Cavity

Figure 3.14 shows the evolution of the waist for a full round trip inside the IR-VIS cavity. Due to the elliptical beam shape, the cylindrical focusing mirrors and the Brewster cut crystal, it is necessary to treat the tangential and sagittal beam independently. The simulation uses the ABCD-matrix formalism (Appendix A.1) and formula 1.8 to calculate the waist size at the incoupling position. The beam evolution is calculated over the q-parameter, according to equation 1.11. The simulation takes into account every intra-cavity element visualized in figure 3.10, except for the outcoupling mirror, since it is very thin and planar. Plot 3.14 shows, that the waist is only focused in the tangential plane. It reaches a minimum in the center of the crystal, of roughly 26 μm. The sagittal waist remains unfocused with a waist size of about 259 μm at the center of the BBO crystal.

The ABCD-matrix for the tangential plane is slightly more complicated than for the sagittal plane.

$$
\begin{aligned}
M_t = \begin{pmatrix} A_t & B_t \\ C_t & D_t \end{pmatrix} &= \\
&= \begin{pmatrix} 1 & \frac{l_1}{n_{air}} \\ 0 & 1 \end{pmatrix} \begin{pmatrix} 1 & 0 \\ -\frac{2}{R_{\text{sph}} \cos\varphi_1} & 1 \end{pmatrix} \begin{pmatrix} 1 & \frac{l_2}{n_{\text{air}}} \\ 0 & 1 \end{pmatrix} \begin{pmatrix} 1 & 0 \\ -\frac{2}{R_{\text{cyl}} \cos\varphi_1} & 1 \end{pmatrix} \begin{pmatrix} 1 & \frac{l_2}{n_{\text{air}}} \\ 0 & 1 \end{pmatrix} \begin{pmatrix} 1 & \frac{l_c}{n_c} \\ 0 & 1 \end{pmatrix} \begin{pmatrix} 1 & \frac{l_3}{n_{\text{air}}} \\ 0 & 1 \end{pmatrix} \\
&\times \begin{pmatrix} 1 & 0 \\ -\frac{2}{R_{\text{sph}} \cos\varphi_2} & 1 \end{pmatrix} \begin{pmatrix} 1 & \frac{l_3}{n_{\text{air}}} \\ 0 & 1 \end{pmatrix} \begin{pmatrix} 1 & 0 \\ -\frac{2}{R_{\text{sph}} \cos\varphi_2} & 1 \end{pmatrix} \begin{pmatrix} 1 & \frac{l_1}{n_{\text{air}}} \\ 0 & 1 \end{pmatrix}
\end{aligned}
$$

Here, l_1, l_2 and l_3 are the distances from the incoupling position to a spherical mirror, from the spherical mirror to the cylindrical mirror and from the cylindrical mirror to the crystal surface. R_{sph} and R_{cyl} are the radii of curvature of the spherical and the cylindrical mirror, respectively. φ_1 and φ_2 are the angles at which the individual mirrors are tilted, according to figure 3.10.

The ABCD-matrix for the sagittal plane is simpler. The focusing mirrors are cylindrical along the vertical axis, such that the sagittal beam effectively sees them as flat mirrors. Since planar mirrors do not affect on the waist, the free propagation distances can simply be added together $(l_2 + l_3)$.

$$\begin{aligned} M_s &= \begin{pmatrix} A_s & B_s \\ C_s & D_s \end{pmatrix} = \\ &= \begin{pmatrix} 1 & \frac{l_1}{n_{air}} \\ 0 & 1 \end{pmatrix} \begin{pmatrix} 1 & 0 \\ -\frac{2\cos\varphi_1}{R_{\text{sph}}} & 1 \end{pmatrix} \begin{pmatrix} 1 & \frac{l_2+l_3}{n_{air}} \\ 0 & 1 \end{pmatrix} \begin{pmatrix} 1 & \frac{l_c}{n_c^3} \\ 0 & 1 \end{pmatrix} \begin{pmatrix} 1 & \frac{l_2+l_3}{n_{air}} \\ 0 & 1 \end{pmatrix} \\ &\times \begin{pmatrix} 1 & 0 \\ -\frac{2\cos\varphi_2}{R_{\text{sph}}} & 1 \end{pmatrix} \begin{pmatrix} 1 & \frac{l_1}{n_{air}} \\ 0 & 1 \end{pmatrix} \end{aligned}$$

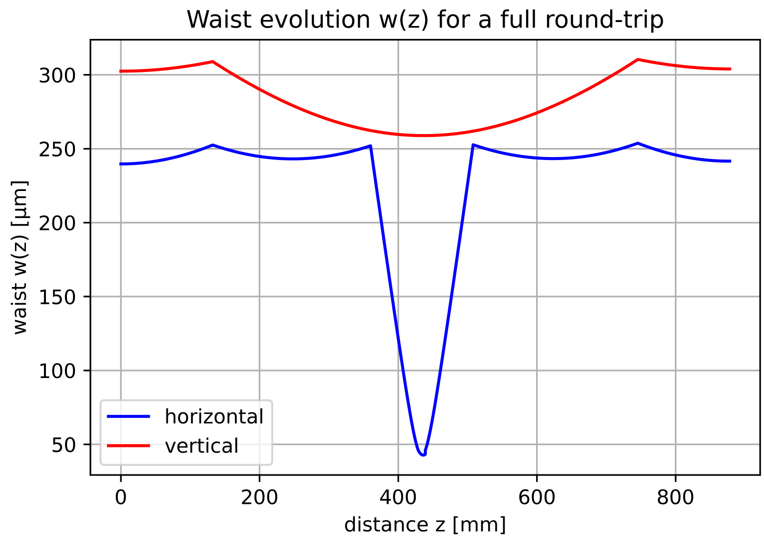

Figure 3.14.: Evolution of the waist size inside the cavity for both axes (horizontal and vertical) of the elliptical beam. The simulations starts and ends at the incoupling position. In the center of the crystal the horizontal waist is strongly focused to increase the frequency conversion. The vertical waist is kept unfocused in order to reduce UV-degradation and average the walk-off effects in this plane.

3.4.3. Barium borate crystal (BaB_2O_4)

For the SHG-process in the second doubling stage, a $(4 \times 4 \times 10)\mathrm{mm}^3$ Brewster-cut barium borate (BBO) crystal by Eksma Optics [9] is used. It is constantly heated to 140°C [40] to reduce temperature fluctuations in the laboratory and to keep out moisture, since it is hygroscopic. In article [44] it has been found out that the resilience against UV-degradation improves with increasing temperature. In [1], BBO crystals from different manufacturers were compared. They report that the crystals show similar performances when heated to above 100°C, compared to room temperatures [45]. This speaks in favor with respect to the reproducibility of an experiment.

BBO is frequently used for frequency doubling from the visible to the deep ultra-violet region [19], [46] and [47]. Relevant crystal parameters are summarized in table 3.3.

	Barium borate crystal (BaB_2O_4)
optical symmetry	negative uniaxial ($n_o > n_e$)
phase-matching	type I (o + o $\rightarrow$ e), critical
phase-matching angle	$\theta_{\mathrm{pm}} = 62.7°$, $\varphi = 90°$
temperature	140°
nonlinear coefficient	$d_{31} = \pm 0.08$ pm/V; $d_{22} = \pm 2.2$ pm/V
effective nonlinearity	$d_{ooe} = d_{31} \sin\theta - d_{22} \cos\theta \sin(3\varphi) = \mp 0.94$ pm/V
walk-off angle	55.9 mrad (Type I SHG 1064nm)
refractive indices	$n_0(451\ \mathrm{nm}) = 1.68; n_e(225\ \mathrm{nm}) = 1.54$
dimensions	$(4 \times 4 \times 10)^3$ mm
shape	Brewster-cut, $\theta_B = 59.24°$

Table 3.3.: Most relevant BBO crystal parameters [9].

After phase-matching the refractive indices of the fundamental and the harmonic beams to $n = 1.68$, the Brewster angle of the BBO-crystal is $\theta_B = 59.24°$.

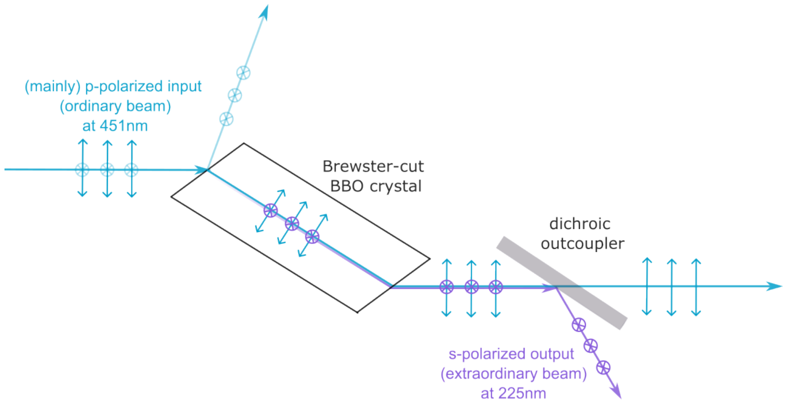

Figure 3.15.: Close up of the behavior of the beam inside the Brewster cut BBO crystal. It takes into account for the polarization of the incoming and the SHG beam and shows the effects of refraction on the surfaces of the crystal according to Snell's law.

Figure 3.15 shows a close up of the BBO-crystal and the dichroic outcoupling window. The incoming beam has mainly ordinary polarization. The part that might have extraordinary polarization is reflected on the surface of the crystal, coupled out of the cavity by a window, and dumped in a beam block. It acts as a reference signal to help with the alignment of the rotation of the crystal. Since the crystal has a Brewster cut, all of the ordinarily polarized light is transmitted and contributes to the frequency conversion. One disadvantage is that the light beam experiences a transverse shift. Upon entering and exiting the crystal, the beam is refracted according to Snell's law given by equation 3.20 [10]:

$$n_1 \sin \theta_1 = n_2 \sin \theta_2 \tag{3.20}$$

This makes the alignment more complicated. What makes it even more challenging, is that the dichroic outcoupling mirror has only a half-inch diameter and is mounted at a steep angle, such that the effective aperture is reduced. Changing the output coupler to a thinner improved the output power by roughly 20%. It is assumed that the high intra-cavity power heats up the mirror, which leads to thermal lensing which causes distortions in the cavity mode when it is locked. Thermal lensing depends on the type of material and its thickness. The exchange to a thinner outcoupler completely solved the thermal lensing problem.

The frequency doubled light experiences a walk-off effect in the vertical axis, since this is the plane of phase-matching. To average over the shifts, the waist is kept large in this axis (sagittal plane). However, in the horizontal axis (tangential plane), the waist is strongly focused to maximize the frequency conversion. The harmonic beam has extraordinary polarization and is extracted from the cavity by a dichroic outcoupling mirror, in order to avoid damaging the cylindrical mirrors with the UV light. The remaining parts of the fundamental beam continue their round-trips through the cavity.

Crystal Degradation

Due to the high-power built-up inside the cavity and thermal heating effects, the used BBO crystal showed irreversible signs of degradation on its surface, even though the elliptical focusing of the beam should mitigate the effect, since the intensity of the beam is distributed over a larger area.

Investigations of the BBO crystal surface with a microscope have shown visible damages, such as burned holes (figure 3.16a and 3.16b). They might originate from the fact that dust corns or imperfections in the crystal surface were illuminated and burned by the laser beam.

Figure 3.16a shows that the most significant hole has an outer diameter of nearly 50 μm, which corresponds exactly to the beam diameter in the horizontal direction. Several small holes with an average diameter of (23 ± 12) μm have also been observed, as seen in figure 3.16b. The smaller holes are due to the fact that the crystal position was shifted several times, to use up more spots before exchanging it. The microscope, which has been used was the Zeiss Axio Imager 2.

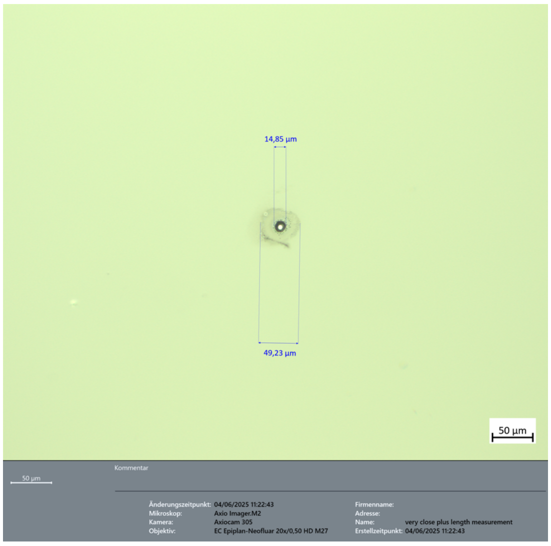

(a) Using a larger magnification, shows the surface damage on BBO input side.

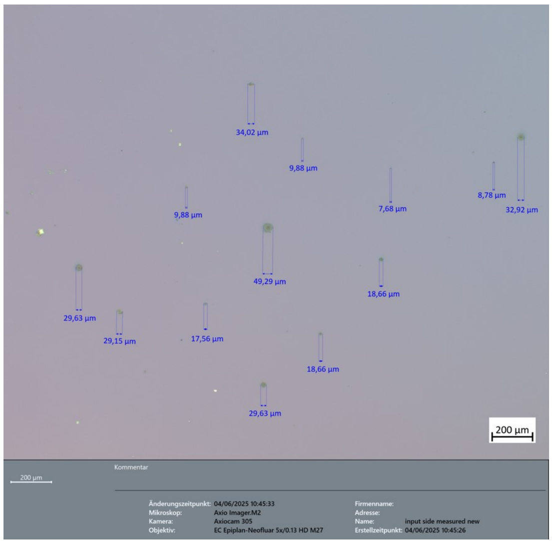

(b) Overview of the surface damages on the BBO crystal.

Figure 3.16.: a) Close up of the main burned hole on the BBO input side. An episcopic (reflected light) plan objective with enhanced contrast and chromatic correction was used. The objective had a magnification factor of 20 and a numerical aperture (NA) of 0.8 for good resolution and brightness.
b) Overview of many small burned spots, with the main one in the middle. For the image generation again an episcopic, plan objective has been used, with a $5\times$ magnification and a NA of 0.13.

The effect of crystal degradation has also been observed by other research groups: K. Takachiho et al. [48] report UV degradation after long-term operation, while M. Scheid et al. [49] saw irreversible crystal damage, especially at high output powers. A different group [50] conducted an investigation on the degradation rate with dependence on the UV output power and the crystal surface, and found that the damage rate is proportional to the strength of the SHG field.

However, distinct groups, such as [1] and [51], report no signs of irreversible damage. The positive effect of the ellipticity has been thoroughly investigated in the article [51]: They argue that, in general, the UV output is limited by two-photon absorption (TPA), which occurs whenever a crystal is irradiated by green and UV light at the same time. The excitation of color centers, followed by the TPA leads to damages, which are due to intrinsic crystal defects. But, they report, that those effects can be reduced by using a beam with a strong ellipticity. [52]

In conclusion, the degradation effects probably depend strongly on the quality of the BBO crystal and the manufacturing process.

Another temperature related issue are temperature gradients inside the BBO crystal. Because of the high circulating power, the crystal itself heats up, which affects the phase matching, so that the cavity alignment and the crystal position need to be optimized in lock.

3.4.4. Optimization of the Performance

The complex setup of the VIS-UV implies many degrees of freedom, which need to be optimized in order to achieve the best overall performance. Although it was often challenging to systematically and individually analyze each parameter, the following section provides a summary of all actions that have been undertaken to achieve optimal performance.

Cylindrical Cavity Mirror Alignment

Since the two focusing mirrors are cylindrically shaped, they require very precise alignment regarding their orientation. Unfortunately, there is not systematic way of scanning their rotation, because of the way the mirrors are mounted. Experimentally, the optimization of their orientation has been done, by loosening the screw of the mount, changing the rotation of the cylindrical mirror slightly, realigning all cavity mirrors and checking the UV-output power until the best angle has been found. For the general alignment of the cavity it is necessary to hit all mirrors centrally. Since the incoupling and the piezo mirror are spherical, the requirements are more relaxed compared to the cylindrical focusing mirrors. For optimal frequency conversion, it is essential to hit the cylindrical mirrors precisely at their center, particularly in the horizontal plane, where the beam is focused strongly.

Incoupling Efficiency

Many efforts were undertaken to increase the incoupling efficiency of the VIS-UV cavity. This has been done, by tuning the angle, at which the fundamental beam enters the cavity and monitoring the incoupling efficiency in parallel. The monitoring is done by the light that is reflected from the incoupling mirror. The incoupling efficiency is then calculated by equation 3.21

$$\eta_{inc} = 1 - \frac{P_{\text{refl,scan}}}{P_{\text{refl,lock}}} \tag{3.21}$$

where $P_{\text{refl,scan}}$ and $P_{\text{refl,lock}}$ are the reflected powers when the cavity is on scan or on lock. Due to limited space, the power cannot be measured directly with a powermeter. Instead, a simple photodiode is used and the conversion efficiency is calculated by the voltage ratio.

Crystal Alignment and Heating

The UV-output power has been increased by changing the roll angle and the Brewster angle of the BBO crystal. This has been done by systematically turning three screws on the side of the crystal holder, to change the angle at which the beam impinges the BBO. In parallel, the conversion efficiency has been monitored to find the best configuration. The conversion efficiency defines how much fundamental light is converted to second-harmonic light. In practice, it is determined by equation 3.22:

$$\eta_{\text{conv.eff.}} = \frac{P_{\text{in}}}{P_{\text{out}}} \cdot \eta_{\text{corr}} \tag{3.22}$$

P_{in} and P_{out} are the fundamental input and harmonic output powers, which are measured using a powermeter. For each cavity a correction factor η_{corr} has been experimentally determined, which accounts for losses on the mirrors. Here, the individual correction factors are:

$$\text{IR-VIS}: \ \eta_{\text{corr}} = 1.1925 \tag{3.23}$$

$$\text{VIS-UV}: \ \eta_{\text{corr}} = 1.0429 \tag{3.24}$$

Additionally, the crystal temperature has been changed iteratively, to find the optimum working temperature, at which the BBO shows the best frequency conversion. It was determined to be at 140°.

Outcoupling Mirror Angle

Since the angle of the outcoupling mirror slightly changes the beam path of the fundamental light during its round trips, it is another degree of freedom that can be optimized. Similar to the rotation-tuning of the BBO, the angle of the outcoupling mirror has been optimized in a similar way. This has been done, by slightly changing its angle and monitoring the finesse $\mathcal{F}$ simultaneously, since $\mathcal{F}$ gives information about the number of round-trips of the fundamental light.

3.5. Length Stabilization of the Cavities

In practice, optical cavities experience perturbations due to mechanical and acoustical noise, temperature fluctuation, or changes in the pressure. Hence, it is crucial that the resonator is always kept on resonance with the input laser light.

Some commonly used length stabilization techniques include the Pound-Drever-Hall (PDH) mechanism [53], the Dither-lock and the Hänsch-Couillaud (HC) [54] locking scheme. In the further section, only the latter will be discussed in detail, since it is the method used in this thesis. Concluding, a short comparison between the three locking-mechanisms is given, to point out, why the Hänsch-Couillaud scheme is the most applicable for our purposes.

3.5.1. Hänsch Couillaud Locking Scheme

The Hänsch-Couillaud (HC) mechanism was introduced in 1980 [54] and was initially intended to lock a laser to a cavity. Here, it is used in the reverse way, such that the cavity is locked to the incoming laser light. The HC-lock is also called a passive polarization technique, since it depends on a polarizing element within the cavity, which can be the Brewster-cut, non-linear crystal. Polarization dependent locking mechanisms are commonly used for frequency doubling cavities for instance by [55], [42] or [19].

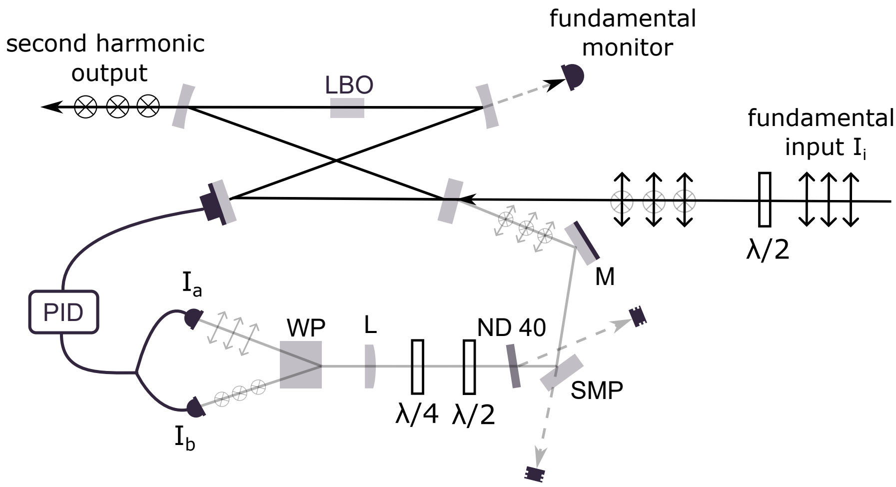

Figure 3.17.: Experimental implementation of the polarization-dependent locking-mechanism of the cavity using the Hänsch-Couillaud (HC) scheme.

The implementation of the HC-scheme is visualized in figure 3.17. The crystals used in both cavities converts horizontally polarized light. This is provided by rotating the polarization of the input laser using a half-wave plate, before entering the cavity. The HC-locking mechanism requires, to slightly rotate the half-wave plate further, in order to add a bit of vertically polarized light. Since the finesse of the cavity is high in the horizontal- and low in the vertical-axis, the fraction with vertical polarization is immediately reflected by the incoupling mirror. Whereas, the light with h-polarization is coupled into the cavity and acquires a phase shift δ. The frequency dependence of this phase shift can be neglected, because the finesse in the v-direction is much lower than in the h-direction. Both, the h- and v-polarized beams are recombined after a full round trip. On resonance, $\delta = 2\pi n$ for integer values of n, they again form linearly polarized light rotated by a certain angle. Off resonance $\delta \neq 2\pi n$, the h- and v-components combine to form an elliptically polarized beam, since they have different amplitudes and are phase-shifted with respect to each other. Using a quarter-wave plate, the elliptical polarization is again converted into linear polarization, which is then split into its horizontal and vertical components by a Wollaston prism, which has a divergence angle of $\theta = 20°$. [11]

The additional half-wave plate in this beam path just adds another degree of freedom to provide a more precise alignment[18]. Although, the intensity of the error signal is already very weak, it is further reduced by a beam sampler (SMP) and a neutral density filter (ND-filter), which has an optical density of $OD = 4$, such that it further attenuates the beam by a factor of [56]:

$$T = 10^{-OD} = 10^{-4} \tag{3.25}$$

In order to achieve an even clearer error signal, the beam is focused onto the photodiodes using a convex lens with $f = 100$mm.

Error Signal

After splitting the horizontally and vertically polarized light at the Wollaston beam splitter, the intensities I_a and I_b of both signals are measured using a differential photodiode. The expected error signal can be derived using Jones calculus, which in detail described in [11]. This yields the following dependence of the intensity difference $I_a - I_b$ with respect to the round-trip phase shift. The theoretical behavior of the error signal is visualized in 3.18.

$$I_a - I_b \propto r_1^2 t_1^2 \frac{\sin \delta}{(1 - r^2)^2 + 4r_1^2 \sin^2(\delta/2)} \tag{3.26}$$

On resonance, both photodiodes will measure the same signals and equation 3.26 will be zero. If the cavity drifts off resonance, the non-zero signal will be fed to the PID-controlling electronics. This drift is then compensated for by changing the position of the mirror, which is mounted on a piezoelectric actuator. Therefore, the relative optical phase in the bow-tie cavity is kept at a constant value within one free spectral range.

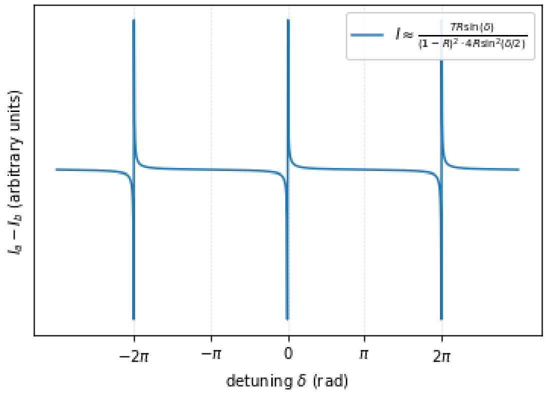

Figure 3.18.: Theoretical shape of the error signal, following the behavior described in equation 3.26.

PID Locking Electronics

A PID locking electronic is an electronic feedback system which uses a Proportional-Integral-Derivative (PID) control algorithm to length stabilize a cavity. Here a single control unit is used to stabilize both cavities, which is also called 2-Channel PID.

It is essential to understand its principle of operation. Here, only a short introduction is given, starting with the front pannel, depicted in figure 3.20. It provides two inputs 'IN 1' and 'IN 2' to connect the error signals, which have been generated by the differential photodiode for the first and second cavity, respectively. The PID provides two outputs 'OUT 1' and 'OUT 2', to control the piezoelectric mirrors. The outputs 'AUX 1' and 'AUX 2' are auxiliary and can be used to monitor the power with two photodiodes. The output 'AUX 3' is not connected internally and unnecessary for the length stabilization

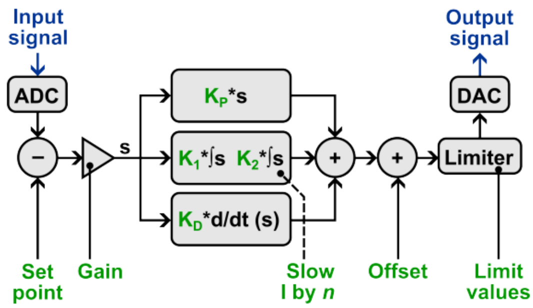

(a) Adjustable PID parameters, which influence the stability of the cavity lock.

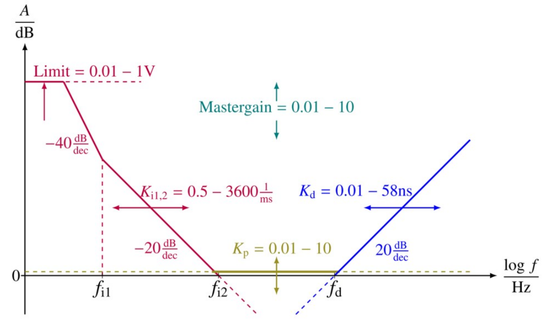

(b) Response of the amplitdue of the PID with respect to the frequency.

Figure 3.19.: a) Visualization of the PID-signal processing. The setpoint defines the target value of the error signal for a cavity in lock. Gain is a factor, which is multiplied to the input signal, depending on the laser power. The K-parameters are again multiplicative factors. After the calculations, an offset is added to the output signal. The maximum output values are bounded limiting values. Figure taken from [18].
b) Visualization of the effect of the individual control parameters of the PID, including their ranges. The graph shows the amplitude response with respect to the frequency. Figure taken from [19].

of the cavities.

The PID settings menu is used for configuration. It takes the input 'IN 1/2', processes the information and in return provides an output signal 'OUT 1/2' according to the settings that were chosen. The processing is visualized in the block diagram 3.19a. Analogue signals are marked in blue and setting parameters are indicated in green.

With respect to figure 3.19b, the frequency ranges are defined by the multiplicative factors K_1, K_2 and K_D and can be calculated by equation 3.27 and 3.28 [19]:

$$f_i = \frac{K_i}{2\pi} \tag{3.27}$$

$$f_d = \frac{1}{2\pi K_d} \tag{3.28}$$

Setpoint gives the target value for the error signal when the cavity is locked. This value has to be adjusted every time when locking the cavity.

Gain is a factor, which is multiplied to all ADC-readings (Analog to Digital Converter). When working with lower/higher laser powers, this factor is usually increased/decreased.

- $K_P \in [0.0, 10]$, $K_1 \in [0.5, 3600]$ ms, K_2 $[0.5, 3600]$ ms and $K_D \in [0.01, 58]$ ns are

Figure 3.20.: PID main interface, which allows to input the error signal from two distinct cavities 'IN 1/2'. After processing the information, a feedback 'OUT 1/2' is returned to the individual piezo mirrors for length stabilization of the resonators. The auxiliary outputs 'AUX 1/2' are used for power monitoring. 'AUX 3' is optional and internally not connected.

again all multiplicative factors for the proportional part, the first and second integral part and the differential part of the controller. The define the frequency ranges for the amplitude response curve of the PID.

- **Slow I by n** is a divider, which takes the average of the last n values of the integral part.

- **Offset:** Defines a certain DC offset, which is added to the output after all calculations have been done. Since it does not affect the cavities while locked, it can be set to $0V$.

- **Limit values** allows to define a maximum integrator value. After reaching this maximum value, the integrator will be reset to 0. It also allows to define the upper and lower output values. Again, if the limits are reached, the output voltage will automatically be reset.

Notch Filter

Since, unwanted noise was impacting the error signal for the VIS-UV cavity, a twin-T notch filter was designed according to [57] and built as part of this thesis. The electronic circuit of the twin-T notch filter is visualized in figure 3.21.

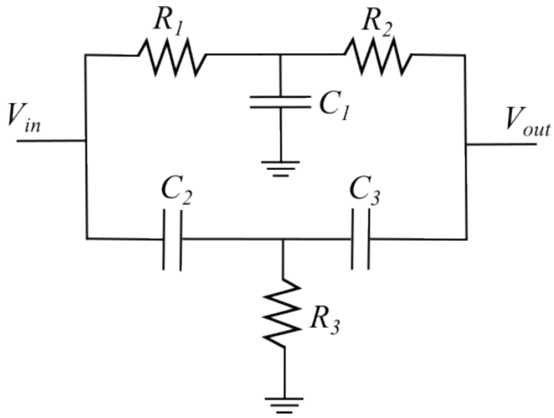

Figure 3.21.: Electric circuit of a twin-T notch filter, to cancel out noise signals at 90 kHz and 100 kHz.

The intention is to filter out the noise signals at 90 kHz and 100 kHz. The values have been obtained by taking the Fourier transform of the error signal on the oscilloscope, which is depicted in figure 3.22a. The setup allows to cancel out noise at two center frequencies, given by equation 3.29 and 3.30

$$f_1 = \frac{1}{2\pi}\sqrt{\frac{\left(\frac{1}{C_3}+\frac{1}{C_2}\right)}{C_1 R_1 R_2}} = 102 \text{ kHz} \tag{3.29}$$

$$f_2 = \frac{1}{2\pi}\sqrt{\frac{1}{C_2 C_3 R_3 (R_1 + R_2)}} = 101 \text{ kHz} \tag{3.30}$$

for the following resistor and capacitor values:

$$R_1 = R_2 = 22 \text{ k}\Omega$$
$$R_3 = 5.6 \text{ k}\Omega$$
$$C_1 = C_2 = C_3 = 100\ \mu\text{F}$$

The notch filter was temporarily integrated between the output signal of the differential photodiode and the input of the PID. As seen from figure 3.22b, it indeed filtered out the unwanted noise. However, it weakened the overall error signal too much, such that it was removed again. Instead a commercial 10 kHz electric low-pass filter from Thorlabs [56] has been installed, which canceled out the unwanted frequency noises. The low frequency-noise at roughly 820 kHz is due mechanical disturbances from turbo pumps, which are installed on the opposite side of our optical table.

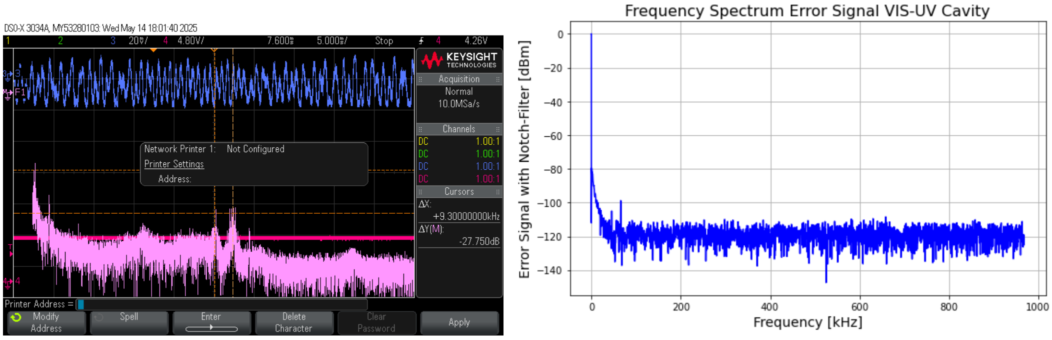

(a) Before installing a twin-T notch filter especially two noise frequencies at 90 kHz and 100 kHz were disturbing the locking signal.

(b) Installing a twin-T notch filter between the output of the photodiode for the error signal and the PID electronics cancells out the unwanted noise.

Figure 3.22.: Effect of the twin-T notch filter on the frequency spectrum of the error signal of the VIS-UV cavity.

Advantages over the Pound-Drever-Hall locking mechanism

The **Hänsch-Couillaud** lock is commonly used to stabilize enhancement cavities. It requires the presence of a birefringent object, which introduces a phase-shift within the cavity, which is apparent for non-linear crystals. The HC-method offers sufficient accuracy and does not require additional hardware components, which makes it a highly suitable locking scheme for cavity length stabilization.

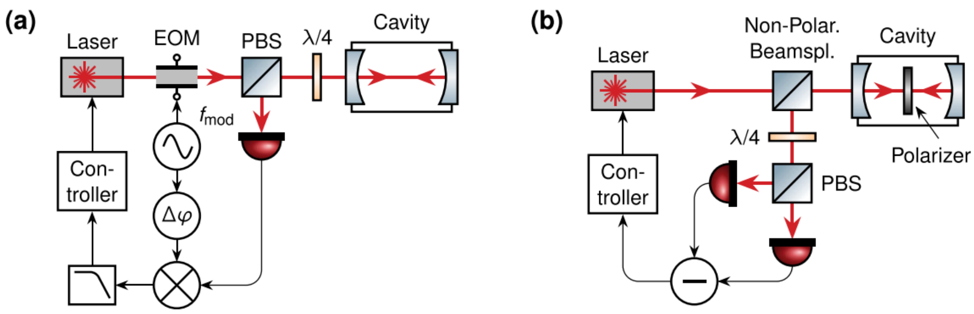

Figure 3.23.: Comparison of the experimental setup of the Pound-Drever Hall (PDH) approach in (a) and the Hänsch-Couillaud (HC) locking mechanism, shown in (b). Figure taken from [20].

The **Pound-Drever-Hall (PDH)** approach requires a modulation of the input signal. It needs additional hardware components, such as an electro-optic modulator (EOM), to modulate an additional phase on top of the carrier frequency. This modulation is imposed on the laser beam at a radio frequency (RF), which creates sidebands. This increases the overall setup complexity. The PDH-method would indeed offer a greater accuracy and frequency stabilization, which is especially necessary for high-finesse cavities. For frequency-doubling enhancement cavities, such a high precision is not necessary. [53]

4. Results: Laser Performance

In this section, the latest performance evaluations of both frequency doubling stages are presented. For each cavity the following parameters have been tested:

- The fundamental input power was stepwise increased and the harmonic output power was measured, to obtain an input-output relation, which should follow a behavior according to equation 2.54.

- The power-dependent conversion efficiency of each cavity was determined by measuring the input and output. The conversion efficiency is a measure of the cavity alignment, mode matching, impedance matching and crystal quality. It is calculated over equation 3.22.

- The incoupling efficiency was evaluated, which gives information about how much fundamental light is coupled into the cavity. This depends on the quality of the mode-matching and the right polarization. The calculation is done over equation 3.21.

- Lastly, long-term stability measurements of the Ti:Sa, as well as the IR-VIS and the VIS-UV cavity were performed. These tests are of great importance for the application of the laser system for future experiments.

4.1. IR-VIS Cavity Performance

4.1.1. Power Scan and Conversion Efficiency

Figure 4.1a shows a power scan of the first cavity. The input-output relation of the power should follow a quadratic behavior $P_{2\omega} \propto P_{\omega}^2$ for low pumping powers. The observed behavior is closer to linear. From figure 4.1a, it can be seen that the conversion efficiency roughly saturates at 75%. This behavior can be attributed to power-dependent impedance mismatches in the cavity: at higher pump powers, gain and intra-cavity losses may become unbalanced. This could be solved by using an incoupling mirror with a transmission, that is optimized to losses when operating with higher input power. When investing more time into the incoupling and the mirror alignment of the IR-VIS cavity, maximum conversion efficiencies of up to 78% have already been achieve. This is also comparable to other groups, for instance [42] have achieved ~ 72 % efficiency, when operating in a slightly higher wavelength-regime from 1046 nm $\rightarrow$ 523 nm.

Figure 4.1b shows both the conversion efficiency and the incoupling efficiency. The incoupling saturates at roughly 89%. This is also comparable to other research groups, like [1] who have achieved conversion efficiencies of up to 80 % when operating at a slightly lower wavelength range 852 nm → 428 nm.

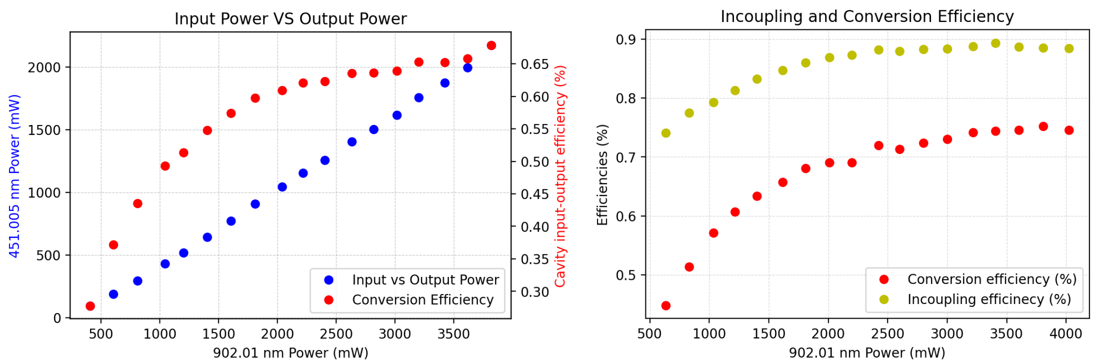

(a) Relation of the input-output power including the conversion efficiency of the IR-VIS cavity.

(b) The conversion and incoupling efficiencies roughly saturate at 75% and 89%.

Figure 4.1.: Performance tests of the IR-VIS cavity, including a (a) power scan and (b) the incoupling and conversion efficiency.

Many efforts have been put into the alignment of the intra-cavity mirrors, such that a finesse of ∼ 200 was achieved. This already accounts for the losses due to conversion. When pumping the IR-VIS cavity with roughly 5 W, a stable output power of 3 W at 451 nm was achieved.

In general, the IR-VIS doubling stage is highly stable and does not require frequent realignment of the resonator itself or the incoupling mirrors. Any drifts in the incoupling optics are compensated for by the Aligna beam stabilization system. Changing the alignment of the incoupling mirrors by hand is generally avoided, since it influences the further beam path and the incoupling into the second cavity.

4.2. VIS-UV Cavity Performance

4.2.1. Power Scan and Conversion Efficiency

From figure 4.2a it can be seen that in the low input regime, the input-output power relation of the VIS-UV roughly follows a quadratic dependence $P_{2\omega} \propto P_{\omega}^2$, as expected theoretically. With increasing input powers, it follows a sub-quadratic behavior, which closely resembles a square-root dependence. This suggests the presence of saturation effects at higher input powers. One possible cause could be thermal effects in the nonlinear crystal or in the cavity mirrors, which can lead to a power-dependent imbalance between gains and losses. For instance, heating can induce temperature gradients in the crystal, which results in a change of the refractive index. Other effects, like thermal lensing and the formation of color centers might degrade the conversion efficiency. Those mechanisms hinder the expected quadratic scaling and instead limit the growth of the second-harmonic output, such that a saturated signal is observed. Compared to the first resonator, the incoupling efficiency of the VIS-UV cavity is lower. The incoupling was improved by optimizing the lens positions of the telescope at high laser powers, since the effective radius of curvature of the lenses changes with different laser powers, which in turn changes the focus position and the waist size inside the cavity. From figure 4.2b it can be seen that the incoupling saturates at 65%. With sensitive adjustments of the incoupling mirrors, a maximum incoupling efficiency of 74% was achieved.

The conversion efficiency of the VIS-UV cavity roughly reaches $9-10\%$, which is significantly lower compared to the IR-VIS resonator. This can be explained by the crystal parameters: The BBO has a smaller non-linear coefficient and a larger walk-off, which effectively lowers the overall conversion efficiency. Also UV-degradation effects within the crystal, like the formation of color centers or thermal lensing effects, reduce the conversion efficiency significantly.

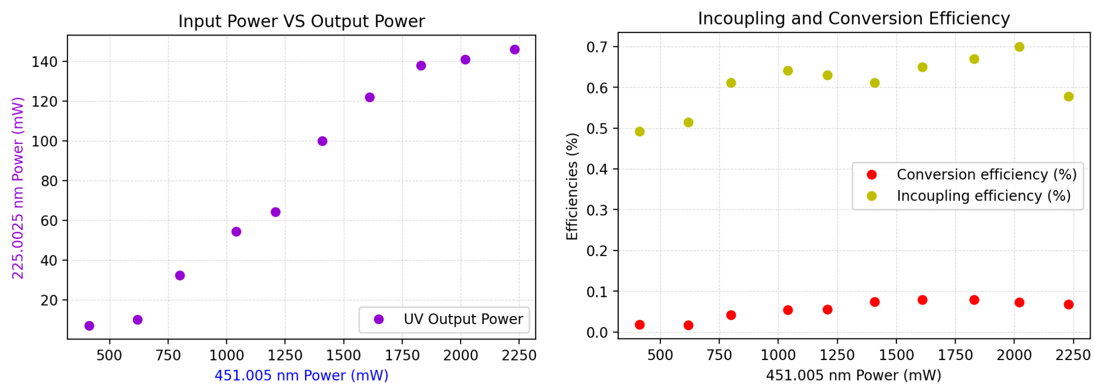

(a) Relation of the input and output power of the VIS-UV cavity.

(b) The incoupling and conversion efficiency roughly saturate at 65 % and 10 %.

Figure 4.2.: Performance checks of the VIS-UV resonator, showing (a) a power scan and (b) the incoupling and conversion efficiencies.

With careful alignment of the cylindrical focusing mirrors, a finesse of up to 190 could be reached. On typical working days and during long operation times the finesse was in the range of 170-180. Comparing this to other groups shows that this still offers room for improvement: For instance, the group [19] has achieved a maximum finesse of $\mathcal{F} = 317$, when generating UV light at a significantly higher wavelength of 313 nm. Overall, the highest UV-output power that was achieved with our resonator was 277 mW, when pumping it with 3 W at 451 nm.

4.3. Stability Measurements

Figure 4.3 shows a combined stability measurement of the three lasers. Since we did not have suitable equipment to measure all three output powers at the same time, the individual measurements were performed consecutively. The stability measurement was not conducted at 70% of the maximum output power of the Ti:Sa laser, in order to prevent unnecessary degradation of the equipment.

The Ti:Sa provides a highly stable output power of 3.5 W over the whole time of operation. The IR-VIS cavity shows slight signs of decay, starting at roughly 2 W, the power dropped down to roughly 1900 mW. After slight adjustments of the phase-matching, the power can be fully regained. The overall performance of the IR-VIS cavity is stable, even after several months of operation, a crystal exchange was never necessary.

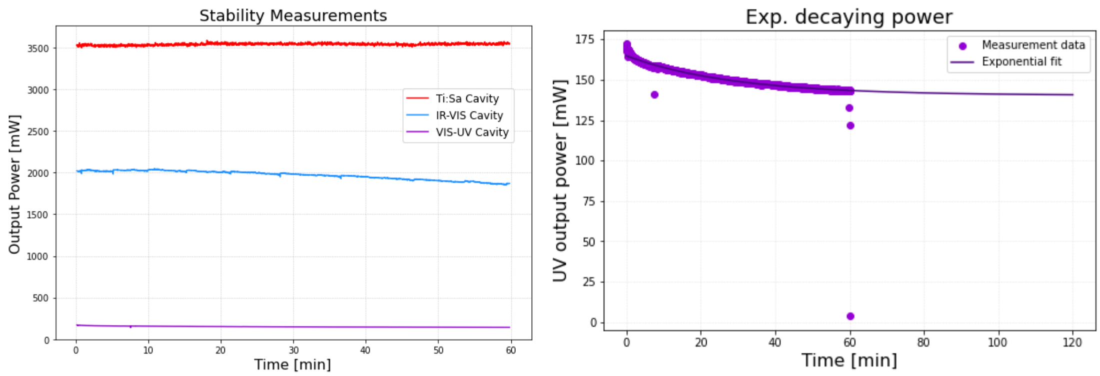

(a) Combined stability measurements of the Ti:Sa laser and the two frequency doubling stages were taken consecutively.

(b) Individual stability measurement of the VIS-UV cavity, showing an exponential power decay.

Figure 4.3.: Stability measurements of the laser output powers. In (a) a combined measurement is shown and in (b) an exponential fit was put over the UV output power.

Figure 4.3b shows a the stability of the VIS-UV resonator in more detail, where an exponential decrease in the beginning is visible. The UV-output power is relatively stable over the one hour measurement, with a power drop of roughly 15%. Starting at 170 mW, the power decreases exponentially and saturates at roughly 140 mW. Repeated stability measurements have shown that a fraction of the power can be regained by optimizing the phase-matching. The only way to regain the full output power is by shifting the crystal position, to hit a new spot. In general this is avoided, since it requires to re-align the cavity mirrors. If a stable operation over several hours is required, it is preferred to operate at a slightly degraded crystal position, since the power level starts at the plateaued position. From experience, the exponential drop in the beginning is not as significant when starting at a slightly degraded spot. For both plots in figure 4.3, the same measurement data for the VIS-UV cavity were taken. The exponential decay of the UV-power was also observed by other researchers, like [1].

Even though, figure 4.3b only shows a stability measurement over one hour, the UV-laser has been used in measurements, where it showed reliable output power over 4 hours of operation over several working days. On each of those working days, only the phase-matching and incoupling alignment was adjusted. Only small power drops were observed, which could be fully regained by shifting the crystal position and realigning the VIS-UV cavity at the end of the week.

It should also be noted that for the stability measurements in figure 4.3 not the maximum pump power was used, to prevent unnecessary crystal degradation. From practice, it seems like the the BBO degradation is proportional to the hours of operation and the input power.

4.4. International Comparison

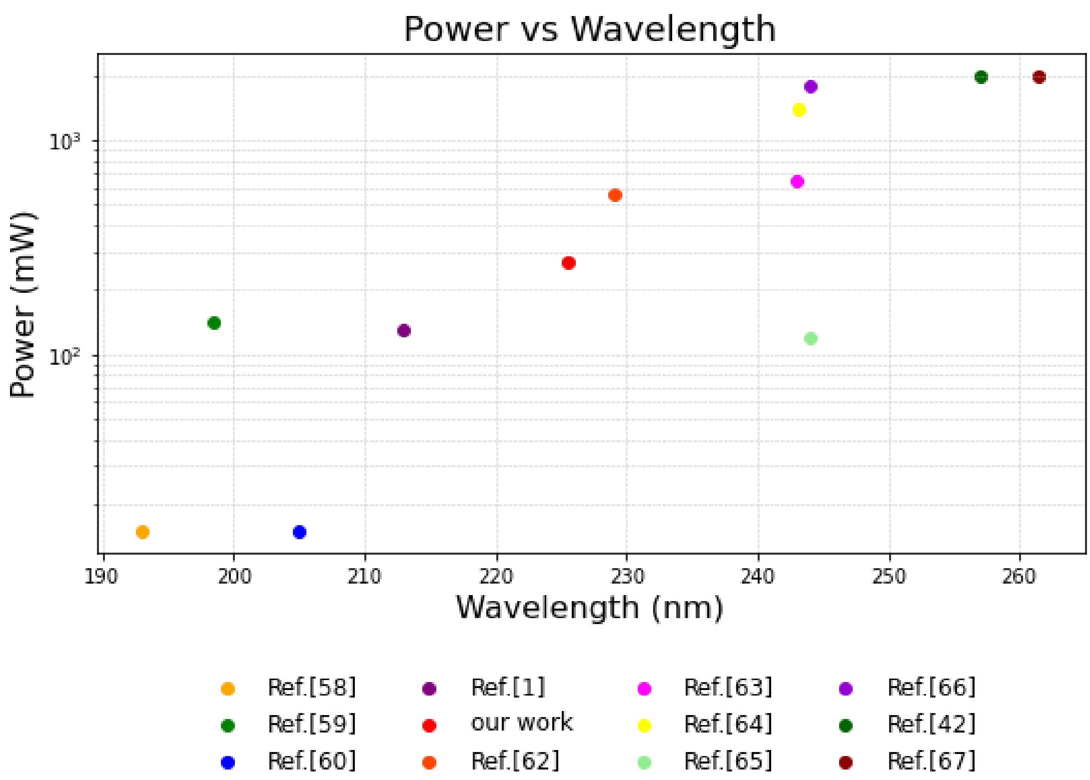

Figure 4.4.: Comparison of the maximum output powers in the deep ultra-violet range from different research groups.

Figure 4.4 gives an overview of UV output powers, which have been achieved at different wavelengths by various research groups [58], [59], [60], [1], [61], [62], [63], [64], [65], [66], [42], [67]. It can be seen from the logarithmic plot that the powers decrease exponentially with decreasing wavelength. It shows that our output power fits well with the prediction and that it is competitive on the international level.

It should be mentioned that figure 4.4 does not take into account for the pump power which generates the UV-light. In order to make more correct assumptions, it would be better to compare the conversion efficiencies instead of the absolute output powers. Unfortunately, many papers did not mention their pumping powers or conversion efficiencies.

5. Application: Ionization Cross-Section Measurements

To show the usefulness of the laser and also prove that it provides sufficiently high and stable output power, ionization cross-sections of silver (Ag) clusters have been measured. With a work function of $W_{Ag} \approx 4.5$ eV [68] it is well below the single photon energy $E_\gamma = 5.82$ eV of the laser light at 225 nm, which is sufficient to ionize the clusters. Firstly, the theory is introduced, followed by the implementation and the conduction of the experiment. Lastly, the results are presented and future improvements are discussed.

5.1. Theory of Ionization Cross-Sections

In general, photoionization describes the absorption of photons by a material, which results in the formation of ions [69]. In the case of metal clusters the process is described by the photoelectric effect, in which electrons are emitted from the material when it is illuminated by electromagnetic radiation with sufficient frequency. The effect was first explained by Einstein in 1905 [70]. A visualization is given in figure 5.1.

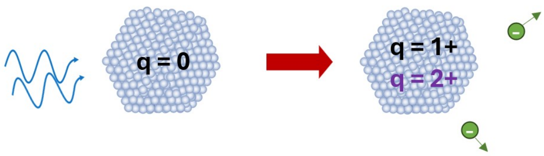

Figure 5.1.: Visualization of the photoelectric effect. The absorption of electromagnetic radiation with suitable frequency by a metal cluster results in the emission of electrons. As a result, the cluster transitions to a higher charge stage and becomes ionized.

A requirement is that the single photon energy, by equation 5.1, exceeds the ionization energy of the particle, which is given by equation 5.2.

$$E_\gamma = h\nu \tag{5.1}$$

$$E_{\text{ion}} = W + \alpha \frac{e^2}{4\pi\varepsilon_0 R} \tag{5.2}$$

Generally, the ionization energy consists of the experimental bulk work function W of the material and the Coulomb energy, which is given by the second term of equation 5.2. The slope parameter α is approximately $\alpha \approx 3/8$ [71]. The cluster radius is given by $R = (3m/4\pi\rho)^{1/3}$.

In order to fully saturate the ionization efficiency and ensure that the transition of the neutral cluster to the ion state is maximized, the single photon energy must exceed the ionization energy by at least $(0.5 - 1)$ eV [72].

On average, the number of absorbed photons by a cluster with an absorption cross-section σ_{abs} is given by equation 6.4.

$$n_{\mathrm{abs}} = \int_{-\infty}^{\infty} \frac{2P\sigma_{\mathrm{abs}}\lambda}{\pi w_x w_y \nu_x hc} e^{-2x^2/w_x^2}\, dx = \sqrt{\frac{2}{\pi}} \cdot \frac{P\sigma_{\mathrm{abs}}\lambda}{w_y \nu_x hc} \tag{5.3}$$

It depends on the laser power P provided by a Gaussian beam with a waist size of ω_x and ω_y, as well as the wavelength λ of the light and the interaction time between the cluster and the photons. The interaction time is defined by the velocity of the particle beam in forward direction v_x. The right side of equation 6.4 is calculated via integration over the beam profile of the laser.

In theory, multi-photon ionization is also be possible, such that the clusters are not singly charged, but are transferred to a higher charge state. However, in this experimental implementation the single photon energy is still too low, compared to the ionization energy of the silver clusters, such that it is assumed that single-charge states are the only present charge state of the ions.

5.2. Experimental Implementation

Figure 5.2 visualizes the setup of the ionization cross-section measurement. A continuous source of silver atoms is provided via a magnetron sputtering source and a gas flow is used to guide the cluster beam. In an aggregation chamber the atoms form clusters, where the number of particles per cluster follow a log-normal distribution [73]. On average the source produces an equal amount of positively charged, negatively charged and neutral clusters, where only neutrals are used for the further experiment. Charged particles are immediately discarded from the beam over external electric fields. The cluster velocity is decreased by an aerodynamic lens and the beam is collimated horizontally using a collimation slit.

There are two interaction zones between the silver clusters and the UV-laser light:

1. With the **first zone**, the relative depletion efficiency, the velocity distribution and the ionization cross-sections are measured.

2. In the **second zone** the neutral particles are ionized by the UV-laser light, which is necessary for the detection method.

A uadrupole mass spectrometer (QMS) is used as a mass analyzer to separate ions by their mass-to-charge ratio, producing a mass spectrum.

In short, the working principle of a QMS is based on stability regions in an electromagnetic field obeying Mathieu's equation, such that only clusters with a suitable mass-to-charge ratio (m/z) can pass [74], [75]. The ions hit a conversion dynode, releasing secondary electrons which are amplified in an electron multiplier to generate a measurable signal.

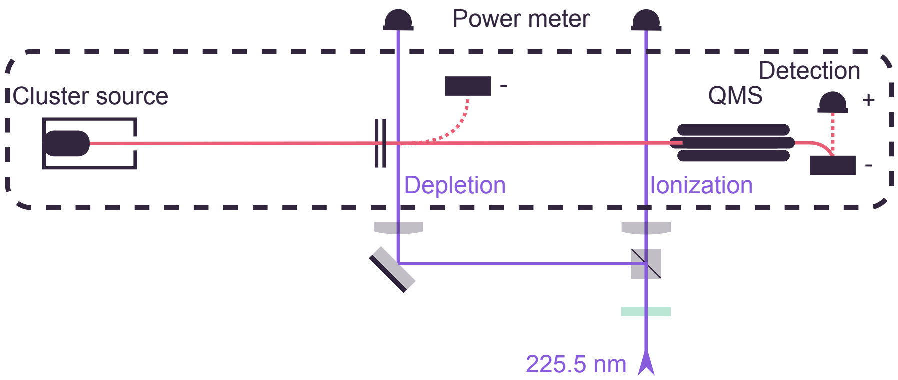

Figure 5.2.: Setup for the photoionization cross-section measurements. Silver clusters are generated in a sputtering source. After two interaction zones with the UV light, they are mass-selected via a quadrupole mass spectrometer and the count rates are measured. Image by Richard Ferstl.

Figure 5.3 shows a SolidWorks drawing of the source (left), the chambers thorough which the clusters are guided using a gas flow (middle). The cluster velocities are determined by the type of gas in the aggregation cell and the plasma settings. They are slowed down using an aerodynamic lens and the beam is collimated with a horizontal slit. Two windows of the vacuum chambers allow to insert the UV-laser light for the interaction. The right side of figure 5.3 shows the QMS for the analysis of the mass spectrum and the count rate-detection.

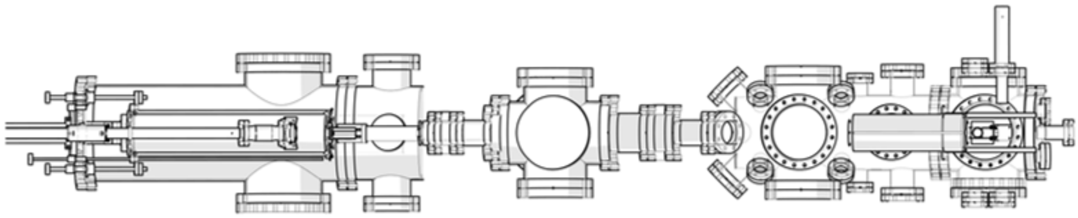

Figure 5.3.: SolidWorks drawing of the experimental setup for the generation of cluster beams: A sputtering head produces silver atoms, which form clusters in an aggregation cell. Two windows of the vacuum chambers allow the interaction with the UV laser light. The cluster count rates are determined with a QMS. Image by Severin Sindelar.

Beam Path

Figure 5.4 shows the extended beam path from the exit of the VIS-UV cavity to the entrance of the vacuum chamber. The light beam is guided in a tube close to the back end of the Ti:Sa. Since the beam is focused horizontally at the BBO crystal position, it has a large divergence angle in this axis, such that a cylindrical lens with $f = 300$ mm is used to focus it. A half wave plate and a polarizing beam splitter cube are used to regulate the power and to split the beam into two beam paths: one for the depletion measurement and the other one for the ionization-based detection. A periscope is used to bring the laser light on the same level as the clusters beam. An additional cylindrical lens with $f = 300$ mm is used to put the focus of the waist on the cluster beam.

The upper mirror of the periscope is mounted on a translation stage to optimally match the height of the laser light to the height of the cluster beam for the depletion measurement. A flip mirror is installed between the periscope and the window of the vacuum chamber. This allows to quickly change the beam path to measure the waist size using a beam profiler.

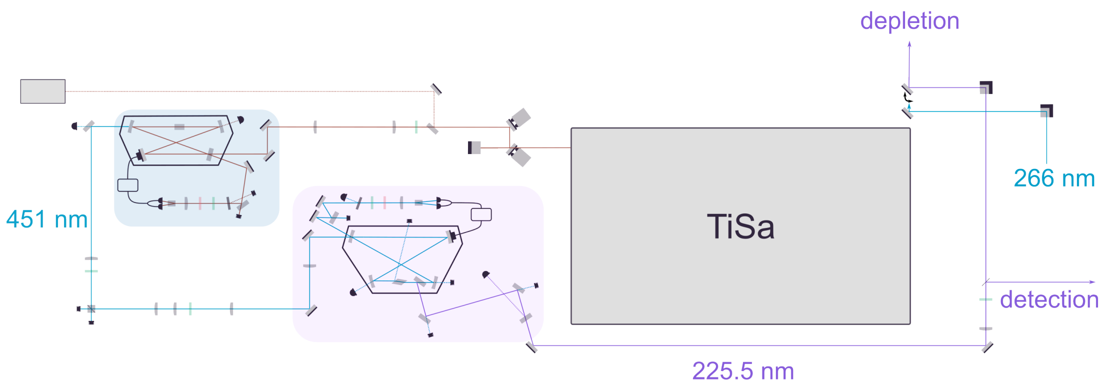

Figure 5.4.: The beam path of the frequency-quadrupling setup is extended and split up for the two interaction zones with the clusters.

5.3. Measurements

5.3.1. Cluster Velocity Distribution

The evaluation of the cross-sections requires to know the velocity of the cluster beam. It was determined via a Time-of-Flight (TOF) measurement, where the results are shown in figure 5.5. A mechanical chopper at a frequency of 26 Hz was temporarily inserted into the laser beam path leading to the first interaction zone. It periodically chops the laser light, which consequently results in a periodic depletion of the cluster beam which is used to evaluate the TOF. Noise is extracted from the measurement data (darkblue curve). The chopper blade is approximated by a step function (yellow). The chopper function is convoluted with a Gaussian (purple curve) to obtain a third function, which is fitted to the denoised measurement data to evaluate the TOF.

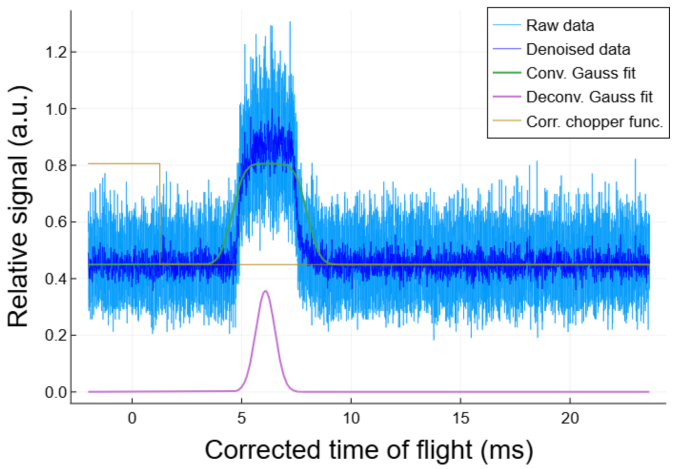

Figure 5.5.: Time of flight between the first interaction zone and the detector for the evaluation of the cluster velocity. A mechanical chopper was used to cut the laser beam.

Knowing the time-of-flight and the distance between the two interaction zones $d_{1/2}$ as well as the length of the QMS l_{QMS}, the cluster velocities can be determined. Since the QMS acccelerates the ions, it slightly modifies the transit time according to equation 5.4:

$$t_{\mathrm{trans}} = \frac{d_{1/2}}{v_0} + \frac{l_{QMS}}{\sqrt{v_0^2 + 2qU/m}} \tag{5.4}$$

t_{trans} is the measured total transit time. $d_{1/2} = (80.0 \pm 0.8)$ cm is the length between the two interaction zones, $l_{QMS} = (31.0 \pm 0.4)$ cm is the length of the QMS and $U \approx 5$ V is the applied voltage. The second term in equation 5.4 comes from the fact that for accelerated charges, the gain in kinetic energy $mv^2/2$ is equal to the loss in potential energy qU, such that $v = \sqrt{2qU/m}$.

Finding an analytical expression of equation 5.4 in terms of the velocity v_0 is difficult. Therefore, the evaluation is done numerically, by inverting 5.4 and interpolating the data. By inserting the TOF-data, which is shown in figure 5.5 into the re-expressed version of equation 5.5, the velocity spread is obtained, which is shown in figure 5.6.

The reason for the high signal for low velocities has purely mathematical reasons and does not represent slow-moving particles. This is because the data from the TOF measurement is mapped to velocity space. The transformation from time to velocity is given by $v = L/t$, where v is the particle velocity, L is the path length and t is the time-of-flight. Converting a TOF signal $S(t)$ to a velocity signal $S(v)$, the following transformation needs to be done: $S(v) = S(t)\ dt/dv = S(t)\ L/v^2$. This means that for slow velocities, the factor $1/v^2$ diverges, which can strongly amplify a weak background signal in the long-time region. Even a small amount of noise can result in a large signal after the conversion, which falsely suggests that many particles have a small velocity. For the correct evaluation of the velocity spectrum , a baseline correction has been done, where data beyond a certain time threshold are excluded from the evaluation to mitigate this issue.

By averaging over the velocity distribution (purple line) from figure 5.6, the mean cluster velocity $\overline{v}$ was determined:

$$\overline{v} = (132.1 \pm 7.2)\ \mathrm{m/s} \tag{5.5}$$

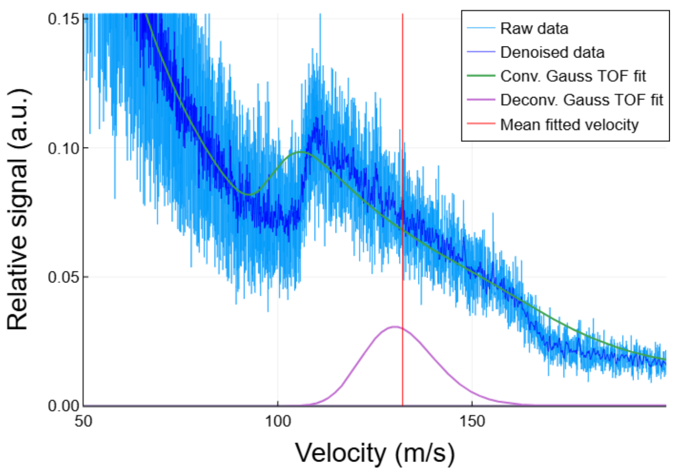

Figure 5.6.: The velocity distribution of silver clusters was obtained by a TOF-measurement and knowing the travel distance.

5.3.2. Waist size

The beam profile of the laser waist at the interaction zone was measured using a camera beam profiler (LaserCam HR II - 1/2"). The most relevant data extracted are the waist diameters in the horizontal w_x and vertical w_y direction. The data was taken from the software of the beamprofiler. The uncertainties were chosen large enough to account for stray noise and the spatial resolution of the camera according to the specification sheet:

$$w_x = (0.5 \pm 0.1)\ \mathrm{mm} \tag{5.6}$$

$$w_y = (4.2 \pm 0.2)\ \mathrm{mm} \tag{5.7}$$

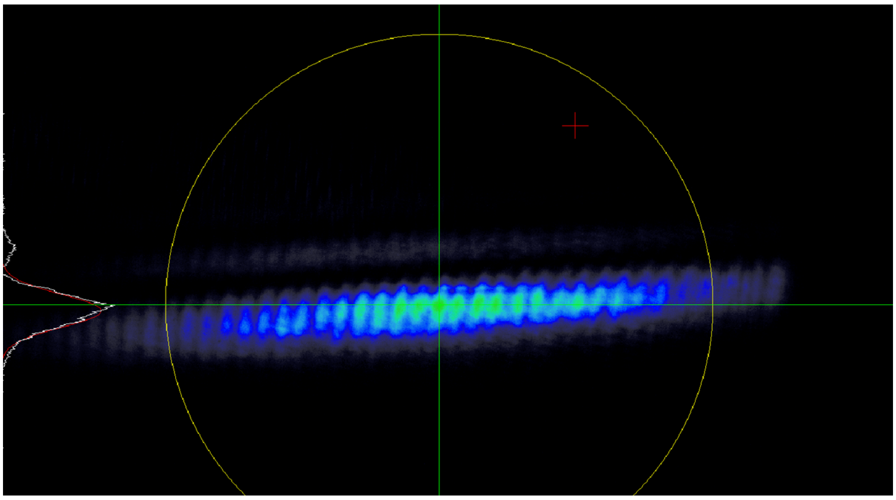

Figure 5.7.: The laser profile in the first interaction zone was measured with a camera beam profiler to evaluate the effective interaction area with the cluster beam .

5.3.3. Photoionization Cross-Sections

The ionization cross-sections σ_{PI} are determined indirectly over a saturation curve fit using equation 5.8, where $S(P_\gamma)$ is the power-dependent signal [76]. The formula can be simplified greatly by collecting all constants in a parameter A.

$$S(P_\gamma) = 1 - \exp\left(-\sqrt{\frac{2}{\pi}} \cdot \frac{\sigma_{\mathrm{PI}} P_\gamma \lambda_\gamma}{hc v_x w_y} \int_{-y_0}^{y_0} \frac{1}{2y_0} e^{-\frac{2y^2}{w_y^2}}\, dy\right) = 1 - \exp\left(-\sigma_{PI} P_\gamma A\right) \tag{5.8}$$

Several parameters have to be known beforehand: P_γ and λ_γ are the power and wavelength of the laser light with a waist size of ω_y in the horizontal axis. v_x is the cluster forward velocity and $2y_0$ is the overlap of the cluster beam and the laser light, which is in this setup determined be the collimation slit width of the cluster beam, which is $2y_0 = (150 \pm 10)\ \mu$m.

Conduction

In the first interaction zone, as seen from figure 5.2, the UV laser power $P_{depl.}$ is stepwise increased from $(0 - 70)$ mW using a half-wave plate and a PBS. Depending on the laser power, a fraction of the neutral clusters absorb photons, become ionized and are depleted from the further path over an external electric field with opposite charge. The remaining neutral clusters travel forward to the detection chamber. Since the QMS-based detection can only measure mass spectra of charged particles, a second interaction zone is required, where the clusters are ionized.

Figure 5.8 shows the mass spectra, which were taken with different depletion powers. For each depletion laser power $P_{depl.}$ a reference measurement was to be taken without laser light, to measure the ratio. With the depletion ratios, the ionization cross-section clusters can be determined using equation 5.8.

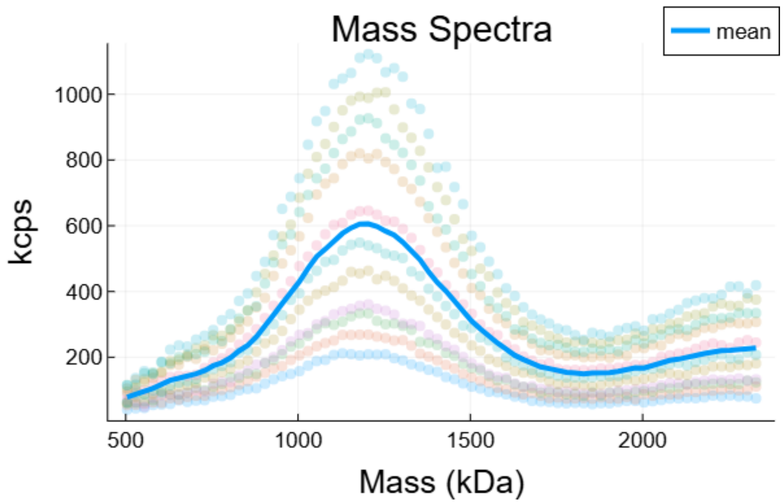

Figure 5.8.: Mass spectra of the silver clusters center mass of 1.2 kDa for different depletion laser powers.

The centers of the individual mass-spectra (figure 5.8) did not shift when changing the depletion power, which indicates that singly charged particles were the only present charge stages.

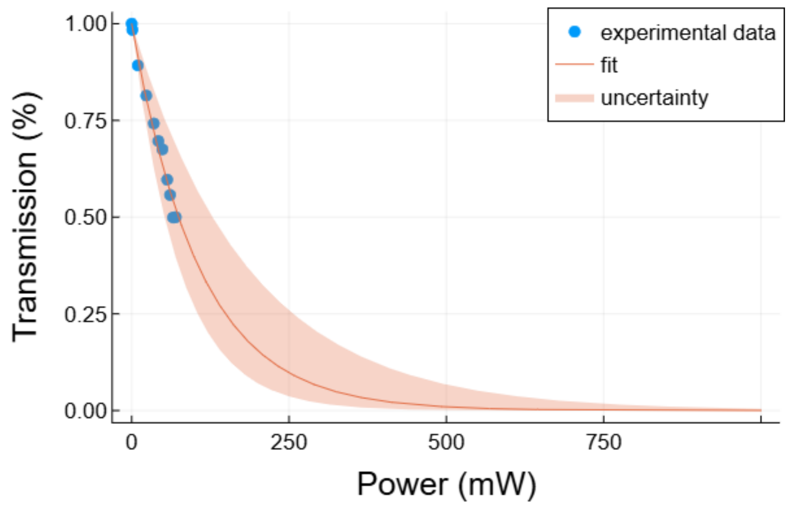

Figure 5.9.: Normalized transmission with respect to the laser power. An exponential fit was put over the measurement data to evaluate the laser power, which would be required to fully deplete the cluster beam.

Figure 5.9 shows the relative transmission of the clusters with respect to the laser power, where the behavior is supposed to follow an exponential decay. The error margins were evaluated over the fit uncertainties, as well as the uncertainties from the velocity and power measurement. The laser intensity was not sufficient to fully deplete the cluster beam. This can be improved by creating a tighter focus of the laser beam, by generating larger clusters, installing windows with higher transmission or by increasing the interaction time via reducing the velocity of the clusters. Especially, measurement data in the range from $(100 - 250)$ mW would have been necessary for a good curve fit. Although, it was mentioned above that UV powers up to 270 mW were already achieved, the laser is not stable enough at such high powers for a full cross-section measurement. Also, this power was measured directly at the exit of the cavity, not taking into account for the transmission losses in the beam path leading to the interaction zones. For a full depletion measurement, either UV-output powers up to ~ 450 mW or a better beam focus would have been necessary.

5.4. Cross-Section Results

With the above described method, we have determined the mass-dependent photoionization cross-sections of silver clusters in a mass range of $(500 - 2350)$ kDa with $\Delta m/m \approx 30\%$ and laser light at 225 nm. The evaluated cross-sections are in the range between $0.6 \cdot 10^{-14}$ cm^2.

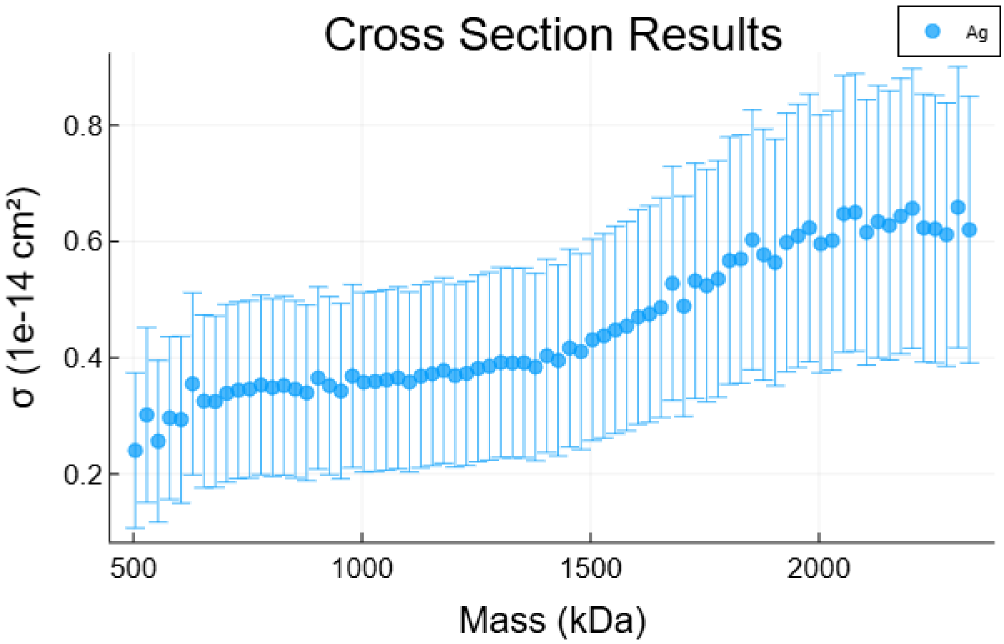

Figure 5.10.: Photoionization cross section of silver clusters in a mass range of (500 – 2350) kDa with laser light at 225 nm.

Evaluation

Koskinen and Manninen distinguish between two photoionization (PI) regimes based on the cluster size [77]. For small clusters, mainly direct PI occurs, which means that a single electron absorbs the photon energy, gets into an excited state and leaves the cluster. The plasmon frequencies are below the photoionization threshold, such that they are not excited. Although, for small clusters, localized electronic excitations may exist, with energies that are close to the single photon energy, such that they might get excited. For larger clusters, on the other hand, the plasmon frequencies are closer to the PI threshold, such that indirect photoionization is dominating. In this case, ionization occurs in two-steps: Firstly, the photon energy excites a plasmon frequency. Secondly, the plasmon decays from the excited to the ground state. During this process it either emits a photoelectron or it heats up and emits phonons. [77]

In this thesis, PI cross-sections of silver clusters with a center mass of 1.2 MDa were measured. Knowing the atomic mass of silver ∼ 108 Da [78], this would mean that the clusters roughly consist of 10^4 atoms. This leads to the assumption that one operates in the large cluster regime, where indirect PI is dominant. However, literature research shows that the plasmon frequencies of silver are unknown in the deep UV-regime.

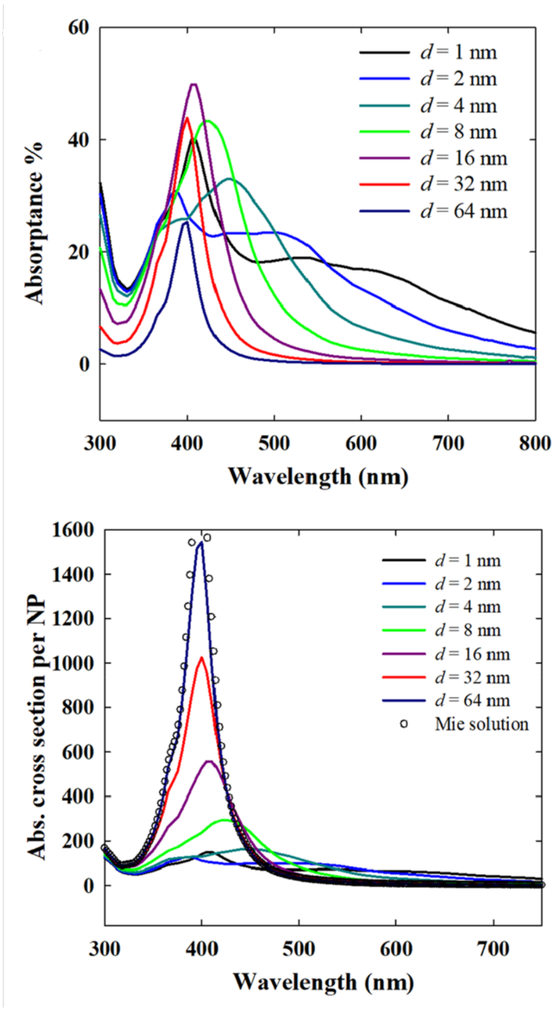

Figure 5.11.: Absorptance and absolute cross-section per nanoparticle for silver. Figure taken and adapted from [21].

Figure 5.11 shows that silver is highly absorptive for wavelengths in the range of $\sim (400 - 550)$ nm. Unfortunately, the plot is cut off at 300 nm, such that one cannot tell for sure if a plasmon frequency was excited with the 225 nm wavelength. However, figure 5.11 indicates that the absorptance is again raising for lower wavelengths [21].

5.5. Improvements

- One way to improve the depletion efficiency is by reducing the mean velocity of the cluster beam. This would require testing different types of gases and gas flows in the aggregation cell as well as the settings of the aerodynamic lens. Reducing the velocity increases the interaction time between the particles and the laser light, such that the probability for photoionization increases.

- Another way to further deplete the cluster beam would be by better focusing of the laser waist: Creating a tighter focus and reducing the ellipticity would increase the intensity of the laser light in the interaction zone, which increases the photoionization probability.
- The laser beam shows astigmatic effects, which means that the foci of the horizontal and vertical axis are not on the same position. Reducing astigmatism would increase the intensity of the light, since the foci overlap. There has been a proposal to compensate for both, ellipticity and astigmatism, in Gaussian beams [79]. The method uses three cylindrical lenses. The first lens can be placed in an arbitrary plane. The other two lenses must be placed next to each other and close to a spot, where the beam is circular. They are rotated against each other at a relative angel $\pm\theta$, where the angle is chosen such that the beam profile is circularly shaped.
- Furthermore, the UV power could be used more efficiently: Instead of splitting the beam into two paths, as seen from 5.4, the same laser beam could be used for the depletion and detection, by guide it back. This would double the available UV power and completely avoids losses from to the PBS.
- To increase the incoupling efficiency of the IR-VIS cavity, the current incoupling mirror could be replaced with a higher transmissive one to compensate for the intra-cavity losses, as figure 1.8 would suggest. This should improve the impedance matching, which in consequence would increase the incoupling efficiency and the overall UV output.
- Although, the rotation of the cylindrical intra-cavity mirrors has already been optimized thoroughly, an even better alignment would increase the finesse and therefore the overall conversion efficiency.
- With respect to the velocity measurement: Increasing the chopper frequency would reduce the opening times and would therefore result in a better signal-to-noise ratio and a higher accuracy.
- Regarding the detection technique: Tests are running, to switch to a digital QMS, which should provide better resolution.

6. Outlook: Photo-Depletion Grating for Matter-Wave Interferometry

Soon after Louis de Broglie published his theory that one can associate a wavelength to massive particles [80], numerous experiments have been conducted to test his hypothesis. Starting with diffraction of electrons by Thomson & Reid [81] and Davisson & Germer [82], followed by helium atoms molecular hydrogen by Estermann & Stern [83] and neutrons by Halban & Preiswerk [84].

Formally, the de Broglie wavelength of a particle with mass m and velocity v is defined by equation 6.1, where h is Planck's constant.

$$\lambda_{dB} = h/mv \tag{6.1}$$

With masses up to 27 kDa, functionalized olgoporphyrins are the most massive particles up to date, that have shown quantum interference effects [85]. The experiment has been conducted in a two-meter long, horizontal interferometer, which is called Long-baseline Universal Matter-wave Interferometer (LUMI). The interferometer scheme works in the near-field regime, where the Talbot-Lau effect is observed. A distinction between near-field and far-field is made by the aperture Talbot length $L_A = A^2/\lambda$, which defines if the operation distance is close or far away from the diffraction aperture.

6.1. Talbot-Lau Effect

In general, the Talbot-Lau effect describes periodic self-imaging. When a plane light wave is diffracted on a periodic transmission mask, the grating period is imprinted in the wave and the pattern will start to replicate itself after certain distances, defined by the Talbot length l_T:

$$l_T = d^2/\lambda_{dB} \tag{6.2}$$

where d is the grating period. This concept for light waves can be extended to atoms, molecules and metal cluster, since they have an associated de Broglie wavelength 6.1.

Talbot-Lau interferometry is a powerful tool to show the delocalization of particles via coherent self-imaging of absorptive gratings. In comparison to the far-field regime, the near field allows more relaxed conditions regarding the collimation of the particle beam and the interferometer length [72].

Kapitza-Dirac Talbot-Lau Interferometry

An extension to mechanical gratings are standing light gratings, with a grating period d, which is half the wavelength λ of the laser light:

$$d = \lambda/2 \tag{6.3}$$

Especially for interference experiments with large metal clusters with masses up to 1 MDa, optical gratings are preferred, since it allows for smaller grating periods and completely avoids clogging. The downside of optical gratings include the setup of a laser source with sufficient power and stable output. This task becomes more challenging, with decreasing wavelength. Standing light gratings can either act as phase gratings, by imprinting a periodic phase onto the matter-wave, or they can be used as optical depletion gratings, where the clusters are ionized when they pass the laser beam close to the anti-node.

Kapitza-Dirac Talbot-Lau Interferometry (KDTLI) combines the operation in the near-field regime (Talbot-Lau effect) with the diffraction technique using standing light gratings. Although, the standing-light wave can be used as both, a phase-grating or a depletion grating, only the latter will be discussed further [72].

6.2. future Experimental Setup

The experimental implementation requires a cluster source, three standing-light depletion gratings and a detection mechanism.

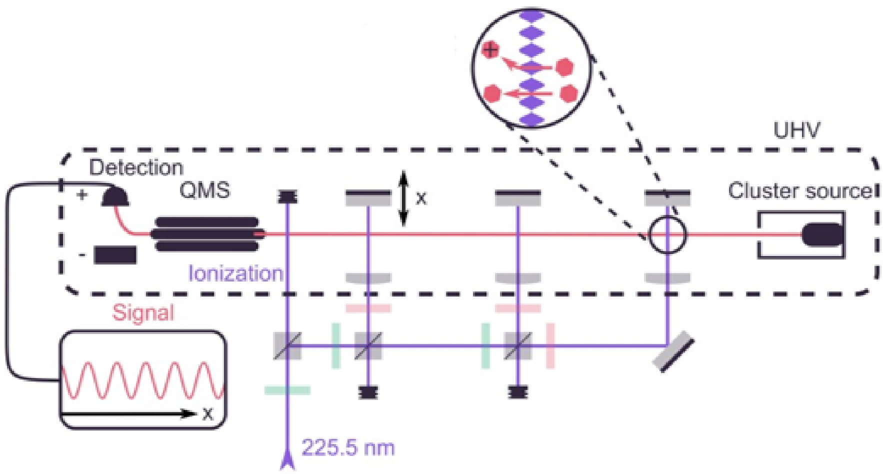

Figure 6.1.: Experimental setup of the interferometer Long-baseline Universal Matter-wave Interferometer (LUMI) with standing-light gratings at a wavelength of 225.5 nm. Image by Richard Ferstl.

The first optical grating prepares coherence and the second one is used for diffraction. After the second grating, a density modulation is imprinted in the beam. For the detection, a third grating is used, which transversely scans over the interference fringes. The neutral particles are ionized by a fourth traveling light beam and the count rates are measured at the detector. Figure 6.1 shows the experimental setup of the cluster interferometer Long-baseline Universal Matter-wave Interferometer (LUMI).

6.3. Laser Power Requirments

When choosing a suitable cluster candidate for interference experiments, one requirement is that its absorption cross-section must be large enough such that it absorbs $2n_{13} + n_2 \approx 10$ photons at the tree standing light gratings. Here n_{13} and n_2 are the number of absorbed photons at the individual gratings. In turn, this gives power requirements on the laser at certain waist sizes [72].

The number of absorbed photons at a standing light wave is given by equation 6.4. The factor of 4 takes into account that the laser forms standing light wave (instead of a traveling wave): As the wave is traveling back and forth, the electric field is doubled ($2E_0$) and the power is proportional to the square of the electric field $P \propto (2E_0)^2$, such that:

$$n_{\text{abs}} = \frac{2P}{\pi w_0^2} \frac{\sigma_{\text{abs}} \tau}{h\nu} \cdot 4 \tag{6.4}$$

The interaction time τ is calculated by the mean velocity of the clusters and the waist size of the laser beam:

$$\tau = \frac{d}{v} = \frac{\sqrt{\pi}}{2} \frac{w_0}{v}. \tag{6.5}$$

Inserting the interaction time from equation 6.5 into equation 6.4 and re-expressing it, yields the following relationship between the required power with respect to the waist of the light beam, which is assumed to be circular $w_x = w_y = w_0$:

$$P = n \frac{h\nu}{\sigma_{\text{abs}}} \sqrt{\pi} w_0 v \tag{6.6}$$

Note that the above mentioned factor of 4 cancels out, since in this setup the laser beam is split into four paths, as it is used for three photon-depletion gratings and one for the ionization-based detection.

Figure 6.2 shows Python simulations for two different scenarios: In 6.2a, clusters with a mass of 100 kDa and a velocity of 130 m/s are assumed, whereas in 6.2b they have a mass of 1 MDa and a velocity of 30 m/s.

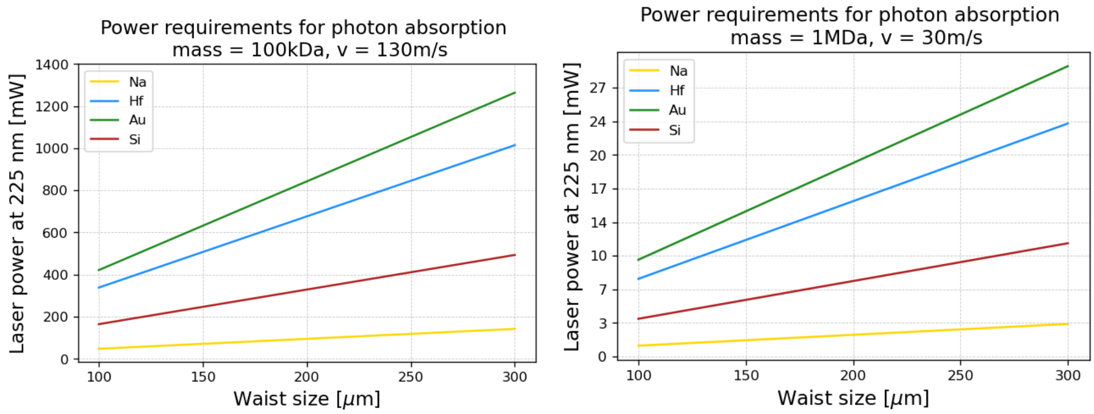

(a) Laser power requirements for clusters with a mass of 100 kDa and a velocity of 130 m/s.

(b) Laser power requirements for clusters with a mass of 1 MDa and a velocity of 30 m/s.

Figure 6.2.: The minimum laser power at a wavelength of 225 nm, which is required to absorb 10 photons in the three ionization gratings. The waist size, is assumed to be circular, such that $w_x = w_y = w_0$.

6.4. Advantages of the UV laser system and Outlook

Exchanging the currently used grating wavelength of 266 nm with 225 nm relaxes the conditions regarding velocity of the cluster beam. Figure 6.3 shows a simulation for sodium (Na), which shows that the particles can be slow for smaller grating wavelengths:

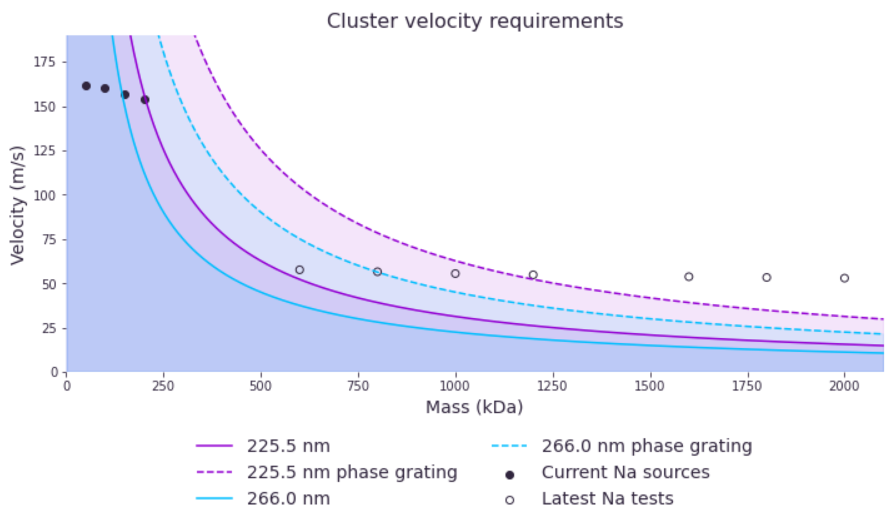

Figure 6.3.: Mass and velocity requirements for the metal clusters with respect the the wavelength of standing light grating/the grating period.

As mentioned above, the single photon energy must exceed the ionization energy of a cluster by at least $(0.5 - 1)$ eV to maximize the PI probability.

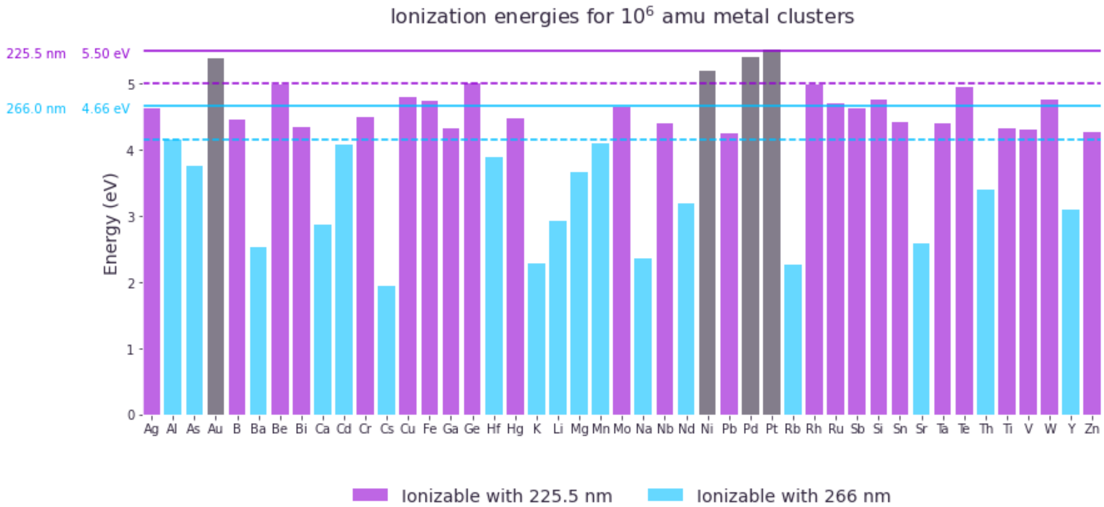

Figure 6.4.: Possible cluster candidates with ionization energies lower than the single photon energies of the currently used optical grating (266 nm) and the future optical grating at 225 nm.

As seen from figure 6.4 moving from towards smaller laser wavelengths (225 nm) offers a big extension in materials and accessible masses, since the single photon energy is $E_\gamma = 5.82$ eV. Although, figure 6.4 only takes into account the work function and not the full ionization energy as defined by equation5.2, it gives a rough estimate on the required single photon energy. This should enable matter-wave interferometry with masses up to 1 MDa-sized clusters. Moving to higher photon energies allows to extend the quantum experiment to gold ($W_{Au} = 5.1$ eV), silver ($W_{Ag} = 4.5$ eV), tantalum ($W_{Ta} = 4.25$ eV) and many other refractory material that are inert, sputter well and are safe to use in large amounts, meaning that they should be non-toxic and non-flammable. It would also make silicon clusters ($W_{Si} = 4.7$ eV) available, which might become interesting when extending the experiments to even larger sized clusters up to $(10 - 100)$ MDa, since cavity cooling and optical feedback schemes require transparent nanoparticles. Smaller grating periods also reduce the Talbot length l_T, the distance after which the interference pattern replicates itself, such that the interferometer length stays within practical limits.

Bibliography

[1] Möller, L., Hannig, S., Truppe, S. & Stellmer, S. A tunable, continuous-wave 130-mW laser at 213 nm (2025). URL http://arxiv.org/abs/2506.08709. ArXiv:2506.08709 [physics].

[2] Matsubara, K., Tanaka, U., Imajo, H., Urabe, S. & Watanabe, M. Laser cooling and isotope-shift measurement of Zn + with 202-nm ultraviolet coherent light. *Applied Physics B: Lasers and Optics* **76**, 209–213 (2003). URL http://link.springer.com/10.1007/s00340-002-1081-7. Publisher: Springer Science and Business Media LLC.

[3] Bahns, J. T. *et al.* Airborne-mercury detection by resonant uv laser pumping. *Opt. Lett.* **22**, 727–729 (1997). URL https://opg.optica.org/ol/abstract.cfm?URI=ol-22-10-727.

[4] Rothschild, M. *et al.* Photolithography at 193 nm. *Journal of Vacuum Science & Technology B: Microelectronics and Nanometer Structures Processing, Measurement, and Phenomena* **10**, 2989–2996 (1992). URL https://pubs.aip.org/jvb/article/10/6/2989/1073486/Photolithography-at-193-nmPhotolithography-at-193. Publisher: American Vacuum Society.

[5] Luo, C. *et al.* Review of recent advances in inorganic photoresists. *RSC Adv.* **10**, 8385–8395 (2020). URL https://xlink.rsc.org/?DOI=C9RA08977B. Publisher: Royal Society of Chemistry (RSC).

[6] Del Barrio, J. & Sánchez-Somolinos, C. Light to Shape the Future: From Photolithography to 4D Printing. *Advanced Optical Materials* **7** (2019). URL https://onlinelibrary.wiley.com/doi/10.1002/adom.201900598. Publisher: Wiley.

[7] Lin, C., Schaubroeck, D., Baets, R., Boon, N. & Le Thomas, N. UV Photonic-Integrated-Circuits-Based Structured Illumination Microscopy With a Field of View Larger than \$100\,\mu \text{m}^{2}\$. *IEEE J. Select. Topics Quantum Electron.* **29**, 1–9 (2023). URL https://ieeexplore.ieee.org/document/10041736/. Publisher: Institute of Electrical and Electronics Engineers (IEEE).

[8] Guo, Q. *et al.* A narrow bandwidth extreme ultra-violet light source for time- and angle-resolved photoemission spectroscopy. *Structural Dynamics* **9** (2022). URL https://pubs.aip.org/sdy/article/9/2/024304/2845288/A-narrow-bandwidth-extreme-ultra-violet-light. Publisher: AIP Publishing.

[9] Optics, E. Bbo - beta barium borate, lbo - lithium triborate (2022). URL www.eksmaoptics.com. Last accessed: 23 April, 2025.

[10] Saleh, B. & Teich, M. *Fundamentals of Photonics, 1st Edition* (1991).

[11] Nagourney, W. G. *Quantum electronics for atomic physics*. Oxford graduate texts (Oxford Univ. Press, Oxford [u.a.], 2010), 1. publ. edn.

[12] Preißler, D., Kiefer, D., Führer, T. & Walther, T. Evolutionary algorithm-assisted design of a UV SHG cavity with elliptical focusing to avoid crystal degradation. *Appl. Phys. B* **125**, 220 (2019). URL http://link.springer.com/10.1007/s00340-019-7333-6.

[13] Petrova-Mayor, A. Development of an eye-safe solid-state tunable laser transmitter around 1.45 my m based on cr 4+:yag crystal for lidar applications (2008).

[14] Boyd, R. W. *Nonlinear optics* (Academic Press is an imprint of Elsevier,, San Diego :, 2020), fourth edition. edn.

[15] Boulanger, B. & Zyss, J. *Nonlinear optical properties*, 178–219 (2003).

[16] GmbH, T. M. Aligna 4d - user manual (modular rack case version) (2020). Last accessed: 09 June, 2025.

[17] GmbH, T. M. Tem messtechnik gmbh website (2025). URL https://tem-messtechnik.de/en/products/active-beam-stabilization/. Last accessed: 08 June, 2025.

[18] Optic, A. 2-channel digital pid for cavity length stabilization (2025). URL www.agile-optic.com. Last accessed: 01 June, 2025.

[19] Hannig, S. *et al.* A highly stable monolithic enhancement cavity for SHG generation in the UV. *Review of Scientific Instruments* **89**, 013106 (2018). URL http://arxiv.org/abs/1709.07188. ArXiv:1709.07188 [physics].

[20] Mäusezahl, M., Munkes, F. & Löw, R. Tutorial on laser locking techniques and the manufacturing of vapor cells for spectroscopy. *New J. Phys.* **26**, 105002 (2024). URL https://iopscience.iop.org/article/10.1088/1367-2630/ad42c6.

[21] Borah, R., Ninakanti, R., Bals, S. & Verbruggen, S. W. Plasmon resonance of gold and silver nanoparticle arrays in the Kretschmann (attenuated total reflectance) vs. direct incidence configuration. *Scientific Reports* **12**, 15738 (2022). URL https://doi.org/10.1038/s41598-022-20117-7.

[22] Siegman, A. E. *Lasers* (Univ. Science Books, Mill Valley, Calif., 1986), 2. pr. edn.

[23] Kogelnik, H. & Li, T. Laser beams and resonators. *Appl. Opt.* **5**, 1550–1567 (1966). URL https://opg.optica.org/ao/abstract.cfm?URI=ao-5-10-1550.

[24] MAIMAN, T. H. Stimulated optical radiation in ruby. *Nature (London)* **187**, 493–494 (1960).

[25] Yariv, A. *Quantum electronics* (Wiley, New York, NY [u.a.], 1989), 3. ed., 7. [print.] edn.

[26] Jackson, J. D. *Klassische Elektrodynamik*. De Gruyter Studium (De Gruyter,, Berlin ; Boston :, 2013), 5. überarb. aufl. edn.

[27] Zhang, W., Yu, H., Wu, H. & Halasyamani, P. S. Phase-Matching in Nonlinear Optical Compounds: A Materials Perspective. *Chem. Mater.* **29**, 2655–2668 (2017). URL https://pubs.acs.org/doi/10.1021/acs.chemmater.7b00243. Publisher: American Chemical Society (ACS).

[28] Yao, J., Shi, W. & Sheng, W. Accurate calculation of the optimum phase-matching parameters in three-wave interactions with biaxial nonlinear-optical crystals. *Journal of the Optical Society of America. B, Optical physics* **9**, 891–902 (1992).

[29] Hobden, M. V. Phase-Matched Second-Harmonic Generation in Biaxial Crystals. *Journal of Applied Physics* **38**, 4365–4372 (1967). URL https://pubs.aip.org/jap/article/38/11/4365/4257/Phase-Matched-Second-Harmonic-Generation-in.

[30] Yao, J. Q. & Fahlen, T. S. Calculations of optimum phase match parameters for the biaxial crystal KTiOPO4. *Journal of Applied Physics* **55**, 65–68 (1984). URL https://pubs.aip.org/jap/article/55/1/65/168678/Calculations-of-optimum-phase-match-parameters-for.

[31] Boyd, G. & Kleinman, D. Parametric interaction of focused gaussian light beams. *IEEE Journal of Quantum Electronics* **4**, 353–353 (1968).

[32] Bourzeix, S., Plimmer, M., Nez, F., Julien, L. & Biraben, F. Efficient frequency doubling of a continuous wave titanium: sapphire laser in an external enhancement cavity. *Optics Communications* **99**, 89–94 (1993). URL https://www.sciencedirect.com/science/article/pii/003040189390710M.

[33] Chen, Y. F. & Chen, Y. C. Analytical functions for the optimization of second-harmonic generation and parametric generation by focused gaussian beams. *Applied Physics B* **76**, 645–647 (2003). URL https://doi.org/10.1007/s00340-003-1190-y.

[34] Daniel, J. R., Tsai, S.-W. & Hemmerling, B. Analytical approximation of the second-harmonic conversion efficiency. *Appl. Opt.* **59**, 9010–9014 (2020). URL https://opg.optica.org/ao/abstract.cfm?URI=ao-59-28-9010.

[35] Kerkoc, P., Bailey, R., Cruickshank, F. & Pugh, D. Second-harmonic generation in biaxial crystals for a focused fundamental gaussian laser beam: application to (–)2--(methylbenzylamino)- 5-nitropyridine single crystals. *Journal of the Optical Society of America B* **15**, 438–445 (1998).

[36] Li, G., Ye, J. & Xu, X. Theoretical analysis of the second-harmonic light power in a biaxial crystal. *Chin. Opt. Lett.* **8**, 693 (2010). URL https://www.researching.cn/ArticlePdf/m00005/2010/8/7/COL08070693.pdf.

[37] und Plasmatechnik GmbH, S. L. Sirah lasertechnik website. Last accessed: 11 June, 2025.

[38] Spectra-physics homepage (2025). URL https://www.spectra-physics.com/en/. Last accessed: 12 June, 2025.

[39] Hannig, D. S. Agile optic website (2025). URL https://www.agile-optic.com/. Last accessed: 08 June, 2025.

[40] Engineering, M. Meerstetter engineering homepage (2025). URL https://www.meerstetter.ch/. Last accessed: 17 June, 2025.

[41] Bourzeix, S., Plimmer, M., Nez, F., Julien, L. & Biraben, F. Efficient frequency doubling of a continuous wave titanium: sapphire laser in an external enhancement cavity. *Optics Communications* **99**, 89–94 (1993). URL https://linkinghub.elsevier.com/retrieve/pii/003040189390710M.

[42] Shaw, J. C., Hannig, S. & McCarron, D. J. Stable 2 w continuous-wave 261.5 nm laser for cooling and trapping aluminum monochloride. *Opt. Express* **29**, 37140–37149 (2021). URL https://opg.optica.org/oe/abstract.cfm?URI=oe-29-23-37140.

[43] Yi, Y. *et al.* All-solid-state continuous-wave frequency-doubled nd:yag/lbo laser with 1.2 w output power at 561 nm. *Laser Physics Letters* **7**, 112 – 115 (2009).

[44] Takachiho, K. *et al.* Ultraviolet laser-induced degradation of cslib6o10 and -bab2o4. *Optical Materials Express* **4**, 559–567 (2014).

[45] Kaneda, Y. *et al.* Continuous-wave, single-frequency 229 nm laser source for laser cooling of cadmium atoms. *Opt. Lett.* **41**, 705 (2016). URL https://opg.optica.org/abstract.cfm?URI=ol-41-4-705.

[46] Peters, E. *et al.* A deep-uv optical frequency comb at 205 nm. *Optics Express* **17**, 9183–9190 (2009).

[47] Röser, D. *et al.* Hyperfine structure and isotope shifts of the $^1p_1 \leftarrow {}^1s_0$ transition in atomic zinc (2023).

[48] Takachiho, K. *et al.* Ultraviolet laser-induced degradation of cslib6o10 and -bab2o4. *Optical materials express* **4**, 559–567 (2014).

[49] Scheid, M. *et al.* 750 mw continuous-wave solid-state deep ultraviolet laser source at the 2537 nm transition in mercury. *Optics letters* **32**, 955–957 (2007).

[50] Kondo, K. *et al.* Demonstration of long-term reliability of a 266-nm, continuous-wave, frequency-quadrupled solid-state laser using -bab2o4. *Optics Letters* **23**, 195–197 (1998).

[51] Gumm, J., Schwarz, D. & Walther, T. High power UV lasers employing elliptically focusing enhancement cavities. *Review of Scientific Instruments* **96**, 033003 (2025). URL https://pubs.aip.org/rsi/article/96/3/033003/3339880/High-power-UV-lasers-employing-elliptically.

[52] Wu, S., Blake, G. A., Sun, S. & Yu, H. Two-photon absorption inside -BBO crystal during UV nonlinear optical conversion. 221 (San Jose, CA, 2000). URL http://proceedings.spiedigitallibrary.org/proceeding.aspx?doi=10.1117/12.379921.

[53] Drever, R. W. P. *et al.* Laser phase and frequency stabilization using an optical resonator. *Applied Physics B Photophysics and Laser Chemistry* **31**, 97–105 (1983).

[54] Hansch, T. & Couillaud, B. Laser frequency stabilization by polarization spectroscopy of a reflecting reference cavity. *Optics communications* **35**, 441–444 (1980).

[55] Kraus, B. *et al.* Phase-stabilized uv light at 267nm through twofold second harmonic generation. *Opt. Express* **30**, 44992–45007 (2022). URL https://opg.optica.org/oe/abstract.cfm?URI=oe-30-25-44992.

[56] Thorlabs (2025). URL www.thorlabs.com. Last accessed: 01 June, 2025.

[57] Design, O. E. (sample) twin-t notch filter design tool (2025). Last accessed: 13 June, 2025.

[58] Kaenders, W. *et al.* A bright continuous-wave laser source at 193nm. *Applied Physics Letters* **103** (2013).

[59] Sakuma, J., Asakawa, Y., Sumiyoshi, T. & Sekita, H. High-power cw deep-uv coherent light sources around 200 nm based on external resonant sum-frequency mixing. *IEEE Journal of Selected Topics in Quantum Electronics* **10**, 1244–1251 (2004).

[60] Fleurbaey, H. *et al.* New measurement of the $1s-3s$ transition frequency of hydrogen: Contribution to the proton charge radius puzzle. *Phys. Rev. Lett.* **120**, 183001 (2018). URL https://link.aps.org/doi/10.1103/PhysRevLett.120.183001.

[61] Kaneda, Y. *et al.* Continuous-wave, single-frequency 229nm laser source for laser cooling of cadmium atoms. *Optics Letters* **41**, 705 (2016). URL http://dx.doi.org/10.1364/OL.41.000705.

[62] Cooper, S. F., Burkley, Z., Brandt, A. D., Rasor, C. & Yost, D. C. Cavity-enhanced deep ultraviolet laser for two-photon cooling of atomic hydrogen. *Opt. Lett.* **43**, 1375–1378 (2018). URL https://opg.optica.org/ol/abstract.cfm?URI=ol-43-6-1375.

[63] Burkley, Z., Brandt, A. D., Rasor, C., Cooper, S. F. & Yost, D. C. Highly coherent, watt-level deep-uv radiation via a frequency-quadrupled yb-fiber laser system. *Appl. Opt.* **58**, 1657–1661 (2019). URL https://opg.optica.org/ao/abstract.cfm?URI=ao-58-7-1657.

[64] Kaneda, Y. *et al.* Continuous-wave all-solid-state 244 nm deep-ultraviolet laser source by fourth-harmonic generation of an optically pumped semiconductor laser using cslib6o10 in an external resonator. *Opt. Lett.* **33**, 1705–1707 (2008). URL https://opg.optica.org/ol/abstract.cfm?URI=ol-33-15-1705.

[65] Burkley, Z. *et al.* Stable high power deep-uv enhancement cavity in ultra-high vacuum with fluoride coatings. *Opt. Express* **29**, 27450 (2021). URL https://opg.optica.org/abstract.cfm?URI=oe-29-17-27450.

[66] Gumm, J., Schwarz, D. & Walther, T. High power UV lasers employing elliptically focusing enhancement cavities. *Review of Scientific Instruments* **96**, 033003 (2025). URL https://pubs.aip.org/rsi/article/96/3/033003/3339880/High-power-UV-lasers-employing-elliptically.

[67] Sakuma, J., Asakawa, Y. & Obara, M. Generation of 5-w deep-uv continuous-wave radiation at 266 nm by an external cavity with a cslib6o10 crystal. *Opt. Lett.* **29**, 92–94 (2004). URL https://opg.optica.org/ol/abstract.cfm?URI=ol-29-1-92.

[68] Eastment, R. & Mee, C. Work function measurements on (100), (110) and (111) surfaces of aluminium. *Journal of Physics F: Metal Physics* **3**, 1738 (2001).

[69] Verlag, S. (ed.) *Atome, Moleküle und optische Physik 1 : Atomphysik und Grundlagen der Spektroskopie*. Springer-Lehrbuch (Springer-Verlag, Berlin, Heidelberg, 2008).

[70] Ouellette, J. Quantum milestones, 1905: Einstein and the photoelectric effect. *Physics (College Park, Md.)* **18** (2025).

[71] Seidl, M., Meiwes-Broer, K.-H. & Brack, M. Finite-size effects in ionization potentials and electron affinities of metal clusters. *Journal of Chemical Physics* **95**, 1295–1303 (1991). URL https://api.semanticscholar.org/CorpusID:55128009.

[72] Kiałka, F., Fein, Y. Y., Pedalino, S., Gerlich, S. & Arndt, M. A roadmap for universal high-mass matter-wave interferometry. *AVS Quantum Sci.* **4**, 020502 (2022). URL https://pubs.aip.org/avs/aqs/article/2835315.

[73] Central Research Institute for Physic, S.-V. Lognormal distribution as the natural statistics of cluster systems .

[74] Mathieu, Mémoire sur le mouvement vibratoire d'une membrane de forme elliptique. *Journal de Mathématiques Pures et Appliquées* **13**, 137–203 (1868). URL http://eudml.org/doc/234720.

[75] Heinrich, J. *A Be+ Ion Trap for H2+ Spectroscopy*. Ph.D. thesis, De Sorbonne Universite (2018).

[76] Pedalino, S., De Sousa, T., Fein, Y. Y., Gerlich, S. & Arndt, M. Exploring metal nanoparticles for matter-wave interferometry. *Phys. Rev. A* **106**, 023312 (2022). URL https://link.aps.org/doi/10.1103/PhysRevA.106.023312.

[77] Koskinen, M. & Manninen, M. Photoionization of metal clusters. *Phys. Rev. B* **54**, 14796–14806 (1996). URL https://link.aps.org/doi/10.1103/PhysRevB.54.14796.

[78] for Biotechnology Information, N. C. eriodic table of elements. (2025). URL https://pubchem.ncbi.nlm.nih.gov/periodic-table/. Last accessed: 10 July, 2025.

[79] Khoubyarian, S., Mashko, A. & Cooper, A. Correcting astigmatism and ellipticity in Gaussian beams using a cylindrical lens pair with tunable focal lengths (2025). URL http://arxiv.org/abs/2506.22308. ArXiv:2506.22308 [physics].

[80] DE BROGLIE, L. Waves and Quanta. *Nature* **112**, 540–540 (1923). URL https://doi.org/10.1038/112540a0.

[81] THOMSON, G. P. & REID, A. Diffraction of Cathode Rays by a Thin Film. *Nature* **119**, 890–890 (1927). URL https://doi.org/10.1038/119890a0.

[82] Davisson, C. & Germer, L. H. Diffraction of electrons by a crystal of nickel. *Phys. Rev.* **30**, 705–740 (1927). URL https://link.aps.org/doi/10.1103/PhysRev.30.705.

[83] Estermann, I. & Stern, O. Beugung von Molekularstrahlen. *Z. Physik* **61**, 95–125 (1930). URL http://link.springer.com/10.1007/BF01340293.

[84] Halban, H. & Preiswerk, P. Preuve expérimentale de la diffraction des neutrons. *Comptes Rendus de l'Académie des Sciences, Paris* **203**, 73–75 (1936).

[85] Fein, Y. Y. *et al.* Quantum superposition of molecules beyond 25 kDa. *Nat. Phys.* **15**, 1242–1245 (2019). URL https://www.nature.com/articles/s41567-019-0663-9.

Acronyms

A. Appendix

A.1. Most relevant ABCD-matrices

Illustration	Matrix	Description
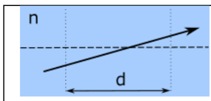	$\begin{bmatrix} 1 & d/n \\ 0 & 1 \end{bmatrix}$	Free propagation in a medium with refractive index n for a distance d.
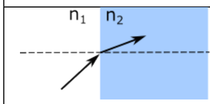	$\begin{bmatrix} 1 & 0 \\ 0 & \frac{n_1}{n_2} \end{bmatrix}$	Refraction on a planar boundary with refractive indices n_1 and n_2.
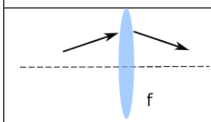	$\begin{bmatrix} 1 & 0 \\ -\frac{1}{f} & 1 \end{bmatrix}$	Transmission through a thin convex lens with focal length $f > 0$.
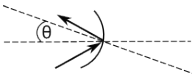	$\begin{bmatrix} 1 & 0 \\ \frac{-2}{R\cos\theta} & 1 \end{bmatrix}$	Tangential plane: Reflection on a spherical mirror with radius R, which is tilted at an angle θ with respect to the beam.
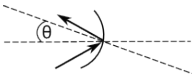	$\begin{bmatrix} 1 & 0 \\ \frac{-2\cos\theta}{R} & 1 \end{bmatrix}$	Sagittal plane: Reflection on a spherical mirror with radius R, which is tilted at an angle θ with respect to the beam.
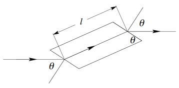	$\begin{bmatrix} 1 & \frac{l}{n^3} \\ 0 & 1 \end{bmatrix}$	Tangential plane: Transmission through a Brewster cut medium of length l and refractive index n.
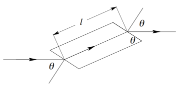	$\begin{bmatrix} 1 & \frac{l}{n} \\ 0 & 1 \end{bmatrix}$	Sagittal plane: Transmission through a Brewster cut medium of length l and refractive index n.

Table A.1.: Summary of all ABCD-matrices used in this thesis to calculate the waist evolution inside and outside the cavities. Figures adapted from [10]. ABCD-matrix information taken from [11], [10] and [12].

A.2. Evaluation of the LBO phase-matching angle

For biaxial crystals, three separate equations are necessary to fully describe the refractive indices along all optical axes. The Sellmeier equations for the LBO are listed below, the data has been taken from the specifications sheet from the manufacturer [9]. Their behavior is plotted in figure A.1.

$$n_x^2 = 2.4542 + \frac{0.01125}{\lambda^2 - 0.01135} - 0.01388\lambda^2 \tag{A.1}$$

$$n_y^2 = 2.5390 + \frac{0.01277}{\lambda^2 - 0.01189} - 0.01849\lambda^2 + 4.3025 \times 10^{-5}\lambda^4 - 2.9131 \times 10^{-5}\lambda^6 \tag{A.2}$$

$$n_z^2 = 2.5865 + \frac{0.0131}{\lambda^2 - 0.01223} - 0.01862\lambda^2 + 4.5778 \times 10^{-5}\lambda^4 - 3.2526 \times 10^{-5}\lambda^6 \tag{A.3}$$

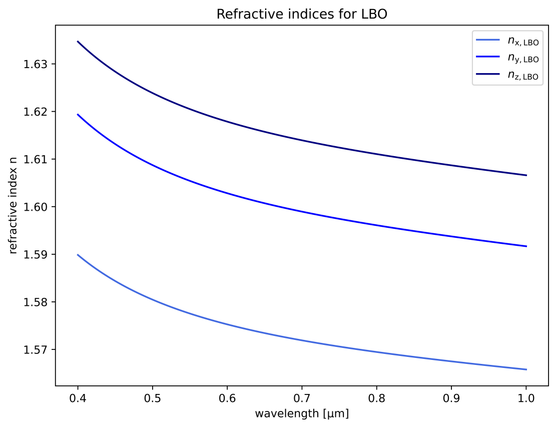

Figure A.1.: Behavior of the refractive indices n_x, n_y, n_z with respect to the wavelength in a LBO crystal.

Calculating the values for the refractive indices n_x, n_y, n_z at the given wavelengths using the Sellmeier equations A.1 - A.2 and plugging them into the equation for the phase-matching angle for biaxial crystal 2.47 yields the following phase-matching angle $\theta_{\mathrm{pm}} = 26.7°$.

A.3. Evaluation of the BBO phase-matching angle

The Sellmeier equations describe the wavelength dependence of the refractive index. For uniaxial crystals two equations are necessary to describe the refractive index in ordinary and extraordinary propagation directions. For a BBO, the Sellmeier equations A.4 and A.5 are listed below, the data has been taken from the specification sheet of the crystal, provided by the manufacturer [9]:

$$n_o^2 = 2.7366122 + \frac{0.0185720}{\lambda^2 - 0.0178746} - 0.0143756\lambda^2 \tag{A.4}$$

$$n_e^2 = 2.3698703 + \frac{0.0128445}{\lambda^2 - 0.0153064} - 0.0029129\lambda^2 \tag{A.5}$$

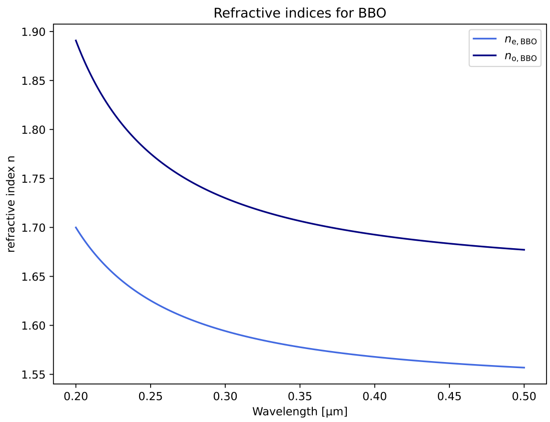

Figure A.2.: Refractive indices along the ordinary and extraordinary axis in a BBO crystal

With reference to the refractive indices listed in table 3.3 the largest conversion efficiency for type I phase-matching is at an angle of $\theta_{\mathrm{pm}} = 62,7°$.